Conférence Internationale sur les Sciences Appliquées et l'Innovation

(CISAI-2023)

Editor :
Dr. Ahmed Rhif (Tunisia)

Proceedings of Engineering & Technology
-PET-

ICID

International Centre for Innovation & Development

Proceedings of Engineering & Technology
-PET-

Conférence Internationale sur les Sciences Appliquées et l'Innovation

(CISAI-2023)

Editor :
Dr. Ahmed Rhif (Tunisia)

PET-Vol. 77
ISSN : 1737-9334

Committees

Committee Chairs:

Afef Khalil (TUN)
Akrouch Soukaina (MAR)
Belatel Mimi (ALG)
Fatima Zohra Boufadi (ALG)
Gherbi Mohamed (ALG)
Georges Descombes (FR)
Hadiza Moussa-Saley (SEN)
Hanaa Benchrifa (MAR)
Haitham Mohamed Ramadan (EGP)
Hayani Mechkouri Meriem (MAR)
Jeru Achyl Hounogbe (SEN)
Mohamad Ramadan (LIB)
Ouardia Laoudj (ALG)
Rahmouni Soumia (ALG)
Rhif Ahmed (TUN)
Sahbeni Kawther (TUN)
Vincent Sambou (SEN)

International Committee:

Abdelkrim Khireddine (ALG)
Abdoulaye Bouya Diop (SEN)
Abdoulaziz Alhassane (SEN)
Afef Trabelsi (TUN)
Ahmed Charif (MAR)
Allé Dioum (SEN)
Amrhar Aicha (MAR)
Barara Mohamed (FR)
Bendifallah Leila (ALG)
Benhabib Lamia (ALG)
Cherkaoui Abdeljzbbar (MAR)
Djalila Boudemagh (ALG)
Faical Mahrek (MAR)
Fateh Mebarek-Oudina (ALG)
Hadja Fatima Mehnane (ALG)
Harrizi Driss (MAR)
Ikhlef Nadia (ALG)
Kheiri Abdelhamid (FR)
Lamia Larioui (MAR)
Madiha Yessari (MAR)
Manal Marzouq (MAR)
Méziane Aïder (ALG)
Mhamed Hammoudi (ALG)
Merdaoui Kamel (ALG)
Mihoub Ouahiba (ALG)
Mor Welle Diop (SEN)
Mounsi Demmouche Nedjoua (ALG)
Nawel Seddiki (ALG)
Ndeye Astou Manel Fall (SEN)
Olfa Kammoun (TUN)
Rachid Benchrifa (MAR)
Rosalie Douyon (FR)
Sara Zatir (ALG)
Sellam Mebrouk (ALG)
Serigne Moussa Dia (SEN)
Sebai Jihane (FR)
Slimane Semghouli (MAR)
Sofiane Amara (ALG)
Souad Elmanssouri (MAR)
Yavo Chaba Estelle Stéphanie (SEN)
Zakaria Ez-Zarzari (MAR)

Summary

Modeling and control of tire pressure for suspension system of Electric vehicle

Rached BEN MEHREZ[1], Abdelkader ABBASSI [2] , Nada OUASLI [3] and Lilia EL AMRAOUI[4]
[1,3,4] *Research Laboratory on Smart Electricity & ICT, National Engineering School of Carthage, , Tunisia*
[2]*Institute of Applied Sciences and Technology of Kasserine (ISSATKas), PO Box 471, 1200 Kasserine, Tunisia,*
rached.benmehrez@gmail.com, abd_abbassi@yahoo.com, nada.ouasli.esti@gmail.com, lilia.elamraoui@gmail.com

***Abstract*—This research paper focuses on the issue of detecting tire pressure in a vehicle using an indirect method, without the need for pressure sensors. The proposed method aims to determine a decrease in pressure by jointly estimating three parameters: the effective radius of two wheels and the front axle rolling resistance force. To achieve this, an observer based on high-order sliding mode theory is developped, which takes into account the angular velocity values of each wheel and the applied torque. This observer demonstrates robustness against uncertainties and disturbances, ensuring convergence in a finite time. Simulation results are provided to illustrate the effectiveness of this approach.**

***Keywords*— Modeling, Effective radius of wheels, Global rolling resistance, High order sliding mode observer, Tire pressure.**

I. Introduction

Ensuring adequate tire pressure in vehicles is crucial for passenger safety as it affects directional stability, manoeuvrability, and comfort. Insufficient tire pressure is known to result in increased fuel consumption [1][13].

However, the use of tire pressure sensors located in the tire valves presents drawbacks such as potential failures, the requirement for specialized tires, and additional costs that car manufacturers aim to avoid. Therefore, there is a genuine interest in eliminating these sensors and finding alternative indirect solutions for tire deflation detection [2].

The objective of this paper is to propose online estimation methods for determining the rolling resistance force and effective radius of the wheels. This assessment of variables, along with the application conditions, represents a novel approach. The estimation results could be utilized by a tire pressure monitoring system (TPMS) [3].

To achieve this, the paper considers the longitudinal and rotational dynamics model of two wheels. A variable structure observer, based on high-order sliding mode theory [4], is designed for the online estimation of the tire radius and rolling resistance force. The input signals for this observer are the angular velocity of each wheel in the train and the applied torque [5]. These signals are available through the controller area networks (CANs).

The observer demonstrates robustness against uncertainties and disturbances, ensuring convergence in finite time. Furthermore, it can be applied to a wide range of observable systems [6][7].

The structure of the paper is as follows: Section II introduces the wheel model, providing the main equations for the longitudinal and rotational dynamics of the two tires. Section III elaborates on the design strategies for the observer in the case of overseeing the wheels on the front axle. Additionally, Section IV presents simulation results to illustrate the practicality of the proposed method. Finally, Section V concludes the paper and provides insights into future work.

II. MODEL OF STATEMENT PROBLEM

The main objective of the presented work is to develop a strategy for estimating the effective radius of two wheels and the rolling resistance force of the vehicle's front axle. This estimation is achieved by using only the vehicle speed, angular velocity of each wheel, and the torque applied to the wheels. The strategy requires the following:

ISSN: 1737-93341

- An adapted model that accounts for the dynamics of the two wheels.
- A solution for assessing the unmeasured variables,

Considering that the evolution of these variables cannot be known beforehand. Therefore, a robust estimation solution must be designed, taking into account the unknown effective radius of the two wheels and the rolling resistance force. By applying the second Newton's law to the forces acting on the two wheels of the front axle, their rotational and longitudinal dynamics can be expressed by:

$$J_l\,\Omega_l = T_l - R_l\,F_{xl} - C_f\,\Omega_l \qquad (1)$$

$$J_r\,\Omega_r = T_r - R_r\,F_{xr} - C_f\,\Omega_r \qquad (2)$$

$$M_{1/2}\nu_x = F_{xr} + F_{xl} - F_{d1/2} - F_{rg} \qquad (3)$$

The subscripts "l" and "r" indicate the front left and right wheels, respectively. The symbol "ω" represents the angular velocity of the left wheel, while "ω" represents the angular velocity of the right wheel. The symbols "Rl" and "Rr" represent the effective radius of the left and right wheels, respectively. The vehicle's linear velocity is denoted by "v." The viscous friction coefficient of the wheel is represented by "γ."

Furthermore, "Jl" and "Jr" are the respective inertias of the left and right wheels, and "m" is half of the vehicle's mass. Additionally, "Tl" and "Tr" denote the torques applied to the left and right wheels, respectively.

The primary forces acting on the two wheels of the front axle are as follows: the traction forces "Fl" and "Fr," the aerodynamic drag forces "Dl" and "Dr," and the overall rolling resistance forces "Rrl" and "Rrr."

1. Tractive forces

The tractive forces are generated by the interaction between the tires and the road surface in response to the applied torque on the wheels. These forces are determined by the friction coefficient and the slip ratio. The slip ratio, as defined in reference [8], represents the relative difference between the actual wheel speed and the ideal wheel speed:

$$\lambda_i = -\frac{\left(\nu_x - R_i\Omega_i\right)}{R_i\Omega_i} = -\frac{\nu_x}{R_i\Omega_i} + 1 \qquad (4)$$

where $i \in \{l,r\}$.

The friction coefficient is typically determined using semi-empirical formulas. A commonly accepted approximation, as mentioned in reference [9], expresses the friction coefficient as a function of the slip ratio:

$$\mu_i(\lambda) = 2\mu_0\left(\frac{\lambda_0\lambda_i}{\lambda_0^2 + \lambda_i^2}\right) \qquad (5)$$

where λ_0 is the optimal slip ratio, leading to the maximum friction value $\mu_0 = \mu(\lambda_0)$.

The tractive forces [8] are then given by :

$$F_{xi} = 2\mu_0 \frac{\lambda_0\left(1 - \frac{\nu_x}{\Omega_i R_i}\right)}{\lambda_0^2 + \left(1 - \frac{\nu_x}{\Omega_i R_i}\right)^2} M_{1/2}\, g \qquad (6)$$

ISSN: 1737-93342

2. Aerodynamic force

The force mentioned is directly proportional to the square of the vehicle's velocity, as indicated in reference [10].

$$F_{d1/2}(v_x) = \frac{1}{2}(\rho A_{d1/2} C_{d1/2} v_x^2) \quad (7)$$

with ρ the air density, $A_{d1/2}$ the frontal area of the half-vehicle and $C_{d1/2}$ the drag coefficient.

3. Global Rolling resistance force

There exists a linear relationship between the global rolling resistance force and the vehicle's speed, as expressed by the equation:

$$F_{rg}(\nu_x) = F_{rl}(\nu_x) + F_{rr}(\nu_x) = 2M_{1/2}gC_r\nu_x \quad (8)$$

with C_r the rolling resistance coefficient. This hypothesis can be made for heavy vehicles and is valid on light vehicles only for low speeds [10].

In the case of light vehicles with higher speeds, another equation must be considered:

$$F_{rg}(\nu_x) = 2M_{1/2}g\left[f_0 + 3.24 f_s \left(3.6 v_x / 100\right)^{2.5}\right] \quad (9)$$

The rolling resistance coefficient is mainly determined by several factors, including tire inflation pressure, temperature, velocity, and road surface type. These variables collectively impact the magnitude of resistance encountered by the tires as the vehicle travels on the road.

III. NON LINEAR OBSERVER SYNTHESIS FOR PRESSURE DETECTION

The main objective of this task is to monitor the tire pressures of the two wheels located in the front axle of the vehicle. To achieve this, the methodology presented in references [3] and [4] needs to be extended to design an observer that can estimate the radius of the front axle wheels and the global rolling resistance force of the entire axle.

This proposed observer takes into account the coupling between the two wheels, resulting in a more precise estimation of the wheels' radius . By analyzing the increase in rolling resistance caused by a decrease in tire pressure, accurately estimating the radius of each wheel becomes crucial for detecting and locating any pressure drop.

This estimation plays a significant role in determining whether there is a decrease in tire pressure and identifying its location within the front axle.

A. Observation model

The observer is designed based on a model that incorporates equations (1), (2), and (3) describing the rotational dynamics of the two wheels in the front axle. The effective radius of the wheels, the rolling resistance force of the front axle, and the variable are initially unknown and can potentially change as a result of pressure loss in both wheels [6]. The goal of the observer is to estimate these unknown parameters and track their changes over time, taking into account the dynamics of the system. By continuously updating the estimates, the observer can provide valuable information about the state of the wheels and the front axle, particularly in relation to tire pressure.

ISSN: 1737-93343

The following equations are therefore used

$$\dot{R}_l = \eta_l(t),\ \dot{R}_r = \eta_r(t),\ \dot{F}_{rg} = \eta_g(t) \qquad (10)$$

with $\eta_l(t)$, $\eta_r(t)$ and $\eta_F(t)$ unknown and bounded. The torques applied to each wheel are, respectively, denoted as Γ_l and Γ_r.

By denoting $y = [y_1\, y_2\, y_3]^T = [\Omega_l\, \Omega_r\, v_x]^T$, $x = [x_1\, x_2\, x_3\, x_4\, x_5\, x_6]^T = [\Omega_l\, \Omega_r\, v_x\, F_{rg}\, R_l\, R_r]^T$ and $u = [u_1\, u_2]^T = [T_l\, T_r]^T$ the control input, the dynamic behavior of the whole axle is given by

$$\dot{x} = f(x) + \chi(y,u) + \Delta f \qquad (11)$$

where

$$f(x) = \begin{bmatrix} -\frac{1}{J_l} x_5 F_{xl}(x) \\ -\frac{1}{J_r} x_6 F_{xr}(x) \\ \frac{1}{M_{1/2}}\left(F_{xl}(x) + F_{xr}(x) - F_{d1/2}(x) - x_4\right) \\ 0 \\ 0 \\ 0 \end{bmatrix} \qquad (12)$$

$$\chi(y,u) = \begin{bmatrix} -\frac{C_f}{J_l} x_1 + \frac{1}{J_l} u_1 & -\frac{C_f}{J_r} x_2 + \frac{1}{J_r} u_2 & 0 & 0 & 0 & 0 \end{bmatrix}^T$$

$$\Delta f = \begin{bmatrix} 0 & 0 & 0 & \eta_l(t) & \eta_r(t) & \eta_F(t) \end{bmatrix}^T$$

Two assumptions are considered [4], [6]:

Assumption 1: The uncertainty term Δf does not change the observability of (11). The nonlinear system (11) without any uncertainty $(\Delta f = 0)$.

$$\dot{x} = f(x) + \chi(y,u) \qquad (13)$$

Else, the term $\chi(y, u)$ only depends on well-known (measured) variable: as shown in [11], [12] this term is not required for the observer design and can be removed thanks to an input-output injection function $\chi(y,u)$. The term $-\chi(y,u)$ will be re-injected in the observer.

Assumption 2: The input–output injection function $-\chi(y,u)$ does not change the observability feature. It yields that the system (13) is transformed into

$$\dot{x} = f(x) \qquad (14)$$

ISSN: 1737-93344

B. Observability analysis

The function $\psi(x)$ is defined by

$$\psi(x)=\begin{bmatrix} y_1 \\ \dot{y}_1 \\ y_2 \\ \dot{y}_2 \\ y_3 \\ \dot{y}_3 \end{bmatrix}=\begin{bmatrix} x_1 \\ -\frac{1}{J_l}x_5F_{xl}(x) \\ x_2 \\ -\frac{1}{J_r}x_5F_{xr}(x) \\ x_3 \\ \frac{1}{M_{1/2}}\left(F_{xl}(x)+F_{xr}(x)-F_{d1/2}(x)-x_4\right) \end{bmatrix} \tag{15}$$

The measured variables are the wheels' velocities and the vehicle's longitudinal speed $y=[x_1\ x_2\ x_3]^T$. If the determinant of the Jacobian of the function $\psi(x)$ is in all cases different from 0 on the operating trajectories, this implies that the transformation ψ is invertible and the system (14) is locally observable [3].

TABLE I:
WHEELS AND VEHICULE MODEL PARAMETERS FOR THE AXLE MODEL

Symbol	**Parameter**	**Value**	**Unit**
Left wheel's inertia	J_l	1.6	$Kg.m^2$
Right wheel's inertia	J_r	1.6	$Kg.m^2$
Nominal radius	R_{0i}	0.32	m
Half-vehicle mass	$M_{1/2}$	880	Kg
Frontal area	$A_{d1/2}$	0.65	m^2
Air density	ρ	1.205	Kg/m^3
Gravitational constant	g	9.807	m/s^2
Viscous friction coefficient	C_f	0	$Kg.m^2/s$
Drag coefficient	$C_{d1/2}$	0.25	-
Suspension damping	C_s	7722	Kg/s
Suspension stiffness	K_{si}	19960	Kg/s^2
Peak friction	μ_0	0.9	-
Optimal slip	λ_0	0.25	-

ISSN: 1737-93345

C. Observer design

The application of the inverse input–output injection transformation $\chi\,(y, u)$ allows us to get an observer for system (13)

$$\dot{\hat{x}} = f(\hat{x}, y) + \chi(y, x) + \left[\frac{\partial \psi}{\partial x}\right]^{-1} k(y, \hat{x}) \qquad (16)$$

The function $k(y, \hat{x})$ has to be designed such that the state vector $\hat{x}$ of the previous system is reaching the vicinity of state vector of system (11) in finite time in spite of the uncertain dynamics Δf of R_l, R_r and F_{rg} .

A solution for $k(y, \hat{x})$ [3], [4] is suggested in order to obtain an accurate and robust estimation of $\hat{x}$; it is based on high order sliding mode differentiation. Then, the observer (16) for the system (11) has a correction term defined by :

$$k(y,\hat{x}) = \begin{bmatrix} \gamma_1 \\ \gamma_2 \\ \gamma_3 \\ \gamma_4 \\ \gamma_5 \\ \gamma_6 \end{bmatrix} = \begin{bmatrix} a_1 L_1^{1/2} \left| y_1 - \hat{x}_1 \right|^{1/2} sign(y_1 - \hat{x}_1) \\ a_2 L_1 sign(\gamma_1) \\ a_3 L_2^{1/2} \left| y_2 - \hat{x}_2 \right|^{1/2} sign(y_2 - \hat{x}_2) \\ a_4 L_2 sign(\gamma_3) \\ a_5 L_3^{1/2} \left| y_2 - \hat{x}_2 \right|^{1/2} sign(y_2 - \hat{x}_2) \\ a_6 L_3 sign(\gamma_5) \end{bmatrix} \qquad (17)$$

The parameters used for the axle model are summarized in Table I [3]. The observer coefficients are defined as must be fixed as proposed in [3].

II. SIMULATION AND RESULTS

In this section, we present the results of our solution validation under ideal conditions, where no noise is present. We employed the Matlab/Simulink® software as the tool for constructing the half-vehicle. The torques applied to the two wheels and their angular velocities were obtained from a prototype vehicle, specifically the Renault sedan Laguna II, which was generously provided by Renault [6],[14].

To explore different values for the effective radii and rolling resistance force of the entire axle, we considered two inflation pressure levels. The first pressure value, P1, was set at 2.3 bar, which corresponds to the nominal pressure. For the left front wheel, we used a pressure of 1.9 bar, denoted as P2, while maintaining the right front wheel at its nominal pressure of 2.3 bar. The observer state variables were initialized with the following values.

$$\hat{x}(0) = \begin{bmatrix} \hat{\Omega}_l \\ \hat{\Omega}_r \\ \hat{v}_x \\ \hat{F}_{rg} \\ \hat{R}_l \\ \hat{R}_r \end{bmatrix} = \begin{bmatrix} 15/0.31 \\ 15/0.31 \\ 15 \\ 148 \\ 0.305 \\ 0.305 \end{bmatrix} \qquad (18)$$

ISSN: 1737-93346

The gains values of observer are $L_1 = 6$, $L_2 = 5$ and $L_3 = 4$ where as the initial conditions of the complete model are such that

$$x(0) = \begin{bmatrix} \Omega_l \\ \Omega_r \\ v_x \\ d_c \\ \dot{d}_c \\ d_r \\ \dot{d}_r \end{bmatrix} = \begin{bmatrix} 15/0.3 \\ 15/0.3 \\ 15 \\ 0 \\ 0 \\ 0 \\ 0 \end{bmatrix} \tag{19}$$

Controller design: In order to be as near as possible to real situation, it has been assumed that the effective radii and their dynamics are well-known. A control ensures movement of the vehicle at a slow speed variable in time according to a desired speed v^d [4].

$$v_x^{\,d} = v^d\,(1+\delta_v \sin(\omega t)) \tag{20}$$

with :

$v_x^{\,d}$: Profile to be followed by the speed,
$v^d = 40 km/h$,
$\delta_v = 0.01$,
$\omega = 0.314 rad/s$.

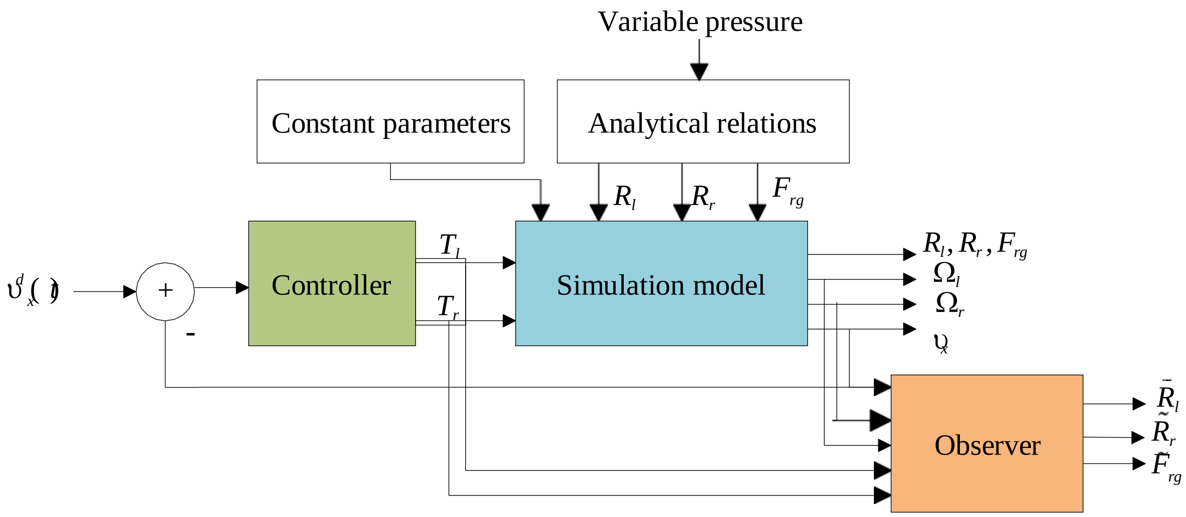

Fig. 1. Schematic diagram for the simulation of the system and the observer effective radusi and the global rolling resistance of front axle of vehicle.

Consider the controller output

$$z = R_i\Omega_i - \upsilon^d{}_x(t) \tag{21}$$

The relative degree of z equals 1, which gives :

ISSN: 1737-93347

$$
\begin{aligned}
z &= \frac{R_i}{J_i}(T_i - R_i F_x - C_f \Omega_i) + R_i \Omega_i - \upsilon_x^d \\
&= \underbrace{-\frac{R_i}{J_i}(R_i F_x + C_f \Omega_i) + R_i \Omega_i - \upsilon_x^d}_{\alpha(x,t)} + \underbrace{\frac{R_i}{J_i}}_{\beta(x,t)} T_i \qquad (22) \\
&= -k z
\end{aligned}
$$

where i ∈ {l,r}.

There fore the torque applied to each wheels can be written

$$
T_i = \frac{1}{\beta_i}\left[-\alpha_i(x,t) - k(R_i \Omega_i - \upsilon_x^d(t))\right] \qquad (23)
$$

with $k \rangle 0$ which is set empirically to $k = 1$ in this test.

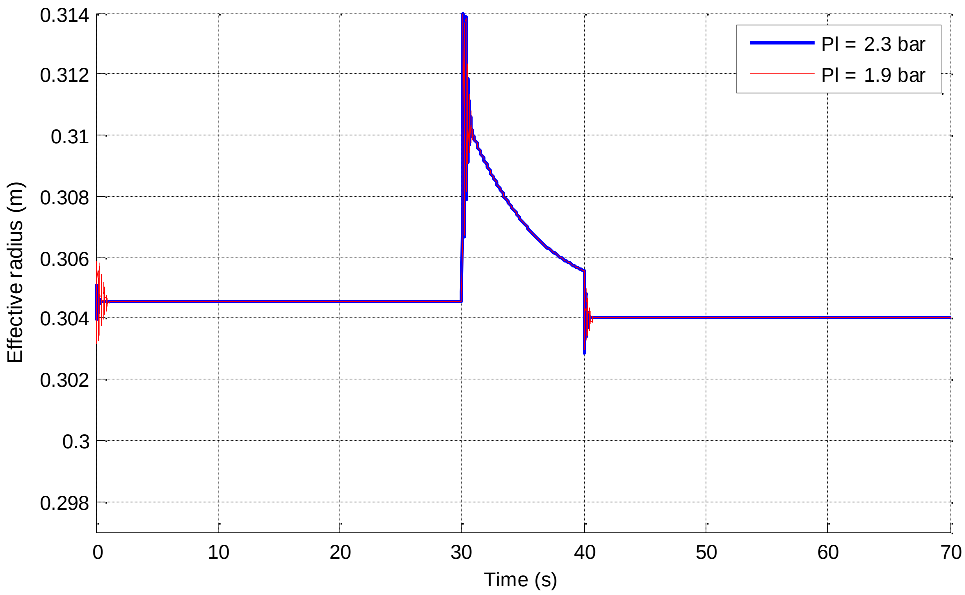

Fig. 3. Estimated right wheel effective radius for two different tire pressures (2.3 and 1.9 bar).

ISSN: 1737-93348

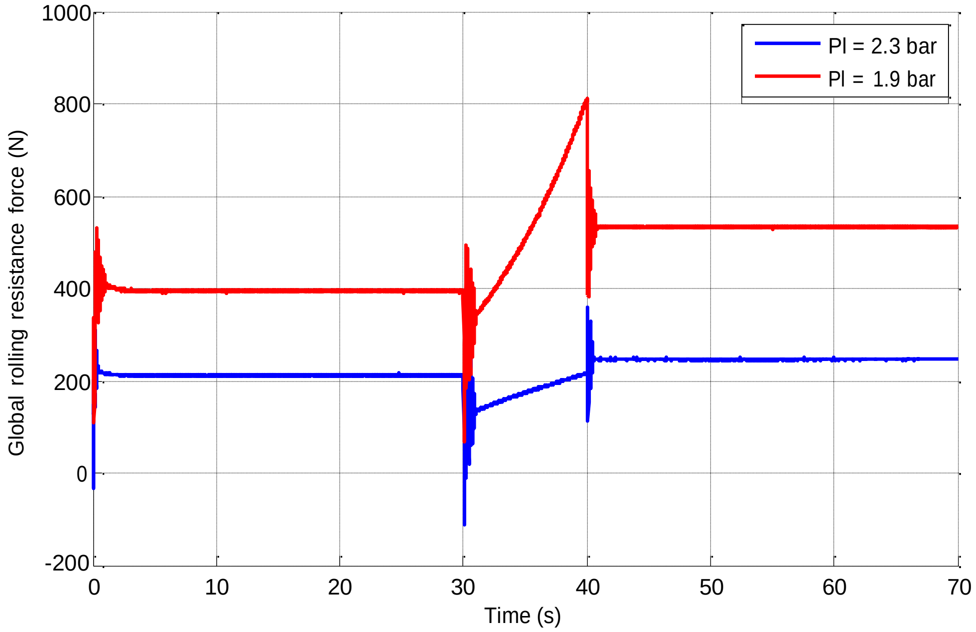

Fig. 4. Estimated global rolling resistance force of the axle for two different tire pressures (2.3 and 1.9 bar).

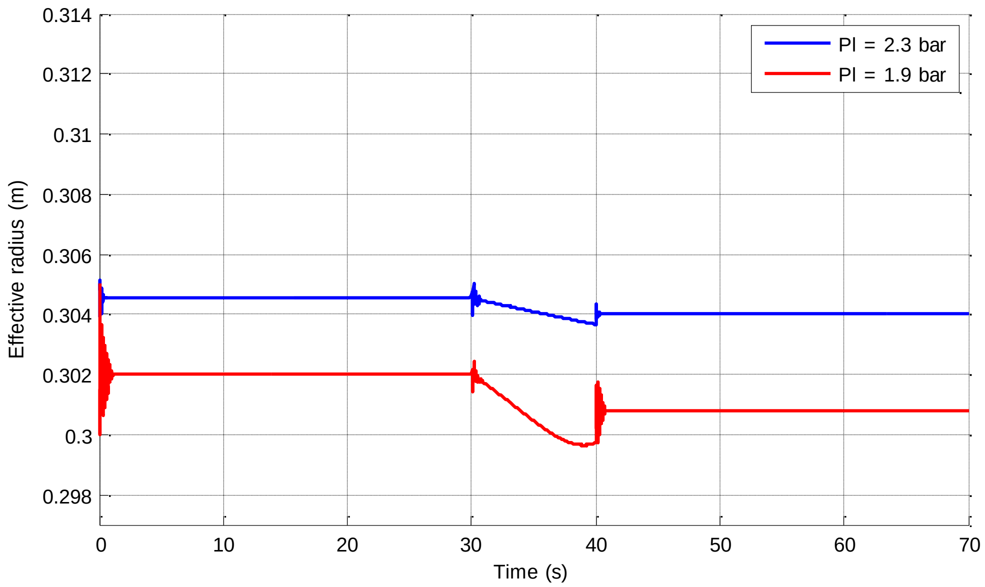

Fig. 2. Estimated left wheel radius for two different tire pressures (2.3 and 1.9 bar).

A simulated scenario involved a 20% decrease in pneumatic pressure from its nominal value of 2.5 bar between specific time intervals $t_1 = 30s$ and $t_2 = 40s$. At the initial time, there was an assumed error of 5 mm between the actual and estimated radii, as well as an error of 1.6 rad/s between the actual and estimated angular velocities for each wheel. Additionally, the two wheels on the front axle of the vehicle had different profiles.

Figures 2, 3, and 4 depict the estimation of the left wheel radius, the right wheel radius, and the global rolling resistance force of the front axle, respectively. It can be observed that when the pressure decreases in the left front wheel's tire, the observer provides a lower value for the wheel radius and a significantly higher value for the global rolling resistance force on the front axle.

The estimated radius of the right front wheel remains constant. The increase in the global rolling resistance force indicates a pressure drop, but it does not alone identify which tire experiences the pressure decrease. The radius of

ISSN: 1737-933416

both wheels are directly related to their respective pressures. These graphical representations enable us to deduce that the pressure drop originates from the left wheel.

IV. CONCLUSION

This paper focuses on estimating the effective radius and global rolling resistance force of the vehicle's front axle. To address the uncertainty surrounding these parameters, a high-order sliding mode observer is employed, leveraging its robustness and accuracy. The use of this observer is motivated by the lack of prior knowledge regarding the evolution of the effective radius and rolling resistance force. The obtained results demonstrate a satisfactory estimation of the effective radii and rolling resistance force for the vehicle's front axle. This suggests that the sliding mode observer effectively captures the desired non-measurable quantities, providing accurate estimations. The observer's robustness allows it to handle uncertainties and disturbances, while its precision ensures reliable estimations even under challenging conditions. Overall, the application of the sliding mode observer proves to be a viable approach for estimating the essential parameters related to the front axle of the vehicle.

Additionally, extending the study to include the observation model and an observer for the characteristics of all four wheels simultaneously presents an intriguing opportunity. This would involve developing a model of the complete vehicle and incorporating it into the observation framework.

REFERENCES

[1] Egaji O.A., Chakhar S., Brown D.: *An innovative decision rule approach to tyre pressure monitoring. Expert Systems with Applications*. 2019, 124, 252-270, DOI: 10.1016/j.eswa.2019.01.051.

[2] S. Velupillai and L. Guveng, "*Tire pressure monitoring,*" IEEE Control Syst. Mag., vol. 27, no. 6, pp. 22–25, Jun. 2007.

[3] El Tannoury, C "*Développement d'outils de surveillance de la pression dans les pneumatiques d'un véhicule à l'aides des méthodes basées sur l'analyse spectrale et sur la synthèse d'observateurs*,". Diss. École centrale de nantes-ECN, 2012.

[4] N. Ouasli, R. Ben Mehrez, L. El Amraoui, " *Parameter estimation of one wheel vehicle using nonlinear observer,*" International Conference on Electrical Sciences and Technologies in Maghreb-CISTEM, Nov. 2014.

[5] T. Boukhobza, "*Observateurs à Modes Glissants et Formes D'observabilité et Analyse et Synthèse Des Commandes Par Ordres Supérieurs,* " Thèse de doctorat, Université de Paris Sud Orsay, 1997.

[6] El Tannoury, C., Moussaoui, S., Plestan, F., Romani, N., & Gil, G. P, "*Synthesis and Application of Nonlinear Observers for the Estimation of Tire Effective Radius and Rolling Resistance of an Automotive Vehicle*,". IEEE Transactions on Control Systems Technology, 21(6), 2408-2416, 2013.

[7] H. Imine, L. Fridman, H. Shraim, and M. Djemai, "*Sliding Mode Based Analysis and Identification of Vehicle Dynamics,*" ser. Lecture Notes in Control and Inf. Sci., New York: Springer-Verlag, 2011, vol. 414.

[8] G. Jazar, "*Vehicle Dynamics: Theory and Applications,*" 1st ed. New York: Springer Verlag, 2008.

[9] W-E.Ting and J-S.Lin, "*Nonlinear control design of anti-lock braking systems combined with active suspensions,"* In 5th Asian control conference, 2004.

[10] T. Gillespie, "*Fundamentals of vehicle dynamics*," SAE International, 1992.

[11] A.J. Krener and A. Isidori, "*Linearization by output injection and nonlinear observers*," Systems & Control Letters, 1983, vol. 3, no 1, p. 47-52.

[12] F. Plestan and A. Glumineau, "*Linearization by generalized input-output injection*," Systems and Control Letters, 31(31):115–128, 1997.

[13] D. Stein, "*Tires and passenger vehicle fuel economy: Informing consumers and improving performances,"* Trans. Res. Board, Washington, DC., TRB Special Rep. 286-78, Aug. 2006.

[14] Žuraulis V., Surblys V., Šabanovič E.: *Technological measures of forefront road identification for vehicle comfort and safety improvement. Transport*. 2019, 34(3), 363-372, DOI: 10.3846/transport.2019.10372.

ISSN: 1737-933416

Conférence Internationale sur les Sciences Appliquées et l'Innovation (CISAI-2023)
Proceedings of Engineering & Technology-PET-Vol 77

Fluid flow and heat transfer around three circulars cylinders in tandem arrangements with variable boundary condition in semi confined media

Farid HACHICHI[*1], Nourdine BELGHAR[*2], Mahfoud KADJA[3], Ridha MEBROUK[#4], Issam REZAIGUIA[#5], [6]Mohammed LACHI

[*1-2] *Mechanical Engineering, University of Mohamed Khider Biskra*
BP 145 RP, 07000 *Biskra*, Algeria

[3] *Mechanical Engineering, University of Mentouri Brothers University of Constantine 1*
P.O. Box, 325 Ain El Bey Way, Constantine, Algeria, 25017

[#4-5] *Drilling and mechanics of oilfildes, University of Kasdi Merbah*
BP.511, 30,000, Ouargla, Algeria

[6] *University of Reims Champagne Ardenne*
Villa Douce - 9, bd de la Paix - CS 60005 - 51724 Reims Cedex, France

[1]hachichifa@yahoo.fr
[2]n.belghar@univ-biskra.dz
[3]kadja_mahfoud@yahoo.fr
[4]ridhamebrouk@gmail.com
[5]irezaiguia1981@gmail.com
[6]m.lachi@univ-reims.fr

***Abstract*— In this paper, tow dimensional unsteady laminar convective heat transfer from three isothermal cylinders of tandem arrangements with variable boundary condition in semi confined media is numerically investigated. The numerical simulations are carried out by solving continuity, momentum and energy equations using a finite volume method-based commercial solver ANSYS-FLUENT. The present study was conducted using a Prandtl number of 0.7 for air as working fluid, with Reynolds number equal to 100, spacing ratio varying from 2 to 5, and at fixed value of blockage ration β=0.25. The characteristics of the flow such as the totals drag and lift coefficients on these dimensionless parameters has been discussed in detail. The isotherms and vorticity were generated to explain the flow and heat transport visualization. The local and average Nusselt numbers for first, second and third cylinder are also computed. It is found that the force coefficients, the wake structure behind the cylinders and the Nusselt number depend strongly on the value of the spacing ratio. Finally in some cases the behavior of the second cylinder does not follow the overall trend of variations.**

***Keywords*— Forced convection, numerical simulation, circular cylinders in tandem arrangement, vortex shedding patterns, Drag and lift coefficients, Nusselt number.**

I. INTRODUCTION

Fluid flow and heat transfer around cylinders has various applications in engineering systems, such as heat exchangers, gas turbine cooling, electronic cooling, and other thermal applications. Flow dynamics and formation of vortices between two tandem bluff obstacles (circular cylinders, square cylinders, trapezoidal cylinders…..) in unconfined and confined domain are very complex, for these reasons, the fluid flow and heat transfer around tow cylinders in tandem arrangements has received a surge attention in the literature (Igarashi [1-2] and Zdravkovich [3]) and the focus of the most investigation is in vortex formation, vibration, forced and heat transfer. A number of studies have been published on this topic. A comprehensive review is presented by Sumner [4] for understanding the effect of placing tow circular cylinders on the flow field structure, aerodynamics loads, vortices and other parameters, the flow around two identical cylinders in a stable cross flow can be divide into (a) extended-body regime; (b) reattachment regime; (c) coshedding regime. Jiang et al. [5] performed numerical simulation of flow past two tandem cylinders of different diameters and assessed the effects of channel walls on the flow field for

ISSN: 1737-933416

blockage ration ranging from 2 to 8. They showed that the channel width has an important effect on the critical spacing where the flow changes from single body mode to co-shedding mode. Sohanker and Etminan [6] presented numerical results of flow characteristics and heat transfer on two equal square cylinders arranged in series at low Reynolds number ($Re = 1 - 200$). Lin et al [7] carried out numerical investigation of flow past two tandem cylinders that are free to move in the transverse direction in a plane channel with a blockage ration of 15% and singled out that the channel walls play an important role in the computed hydrodynamic forces. In another works, the same authors [8] presented numerical results of the unsteady laminar flow and heat transfer from square cylinders in a channel. The results showed that the cylinder Nusselt and Strouhal numbers decrease as the wall is approached. Rosales [9] performed a numerical study of fluid flow and heat transfer over tow squere cylinders with different sizes and arrangements in a channel for $Re = 500$. Considering channel walls and the upstream cylinder as insulators and the downstream cylinder as a hot obstacle, their results show that the drag coefficient and the Nusselt number decrease when the in-line or offset tandem pair of cylinders is positioned coser to a channel wall.

Unsteady laminar convective heat transfer from two isothermal cylinders in tandem arrangement was studied numerically by mahir and Altac [10]. It was shown from the numerical results that the average Nusselt number of the upstream cylinder approached to heat of a single isothermal cylinder for $L/D > 4$ and the average Nusselt number of the downstream cylinder was about 80% of the upstream cylinder. Ding et al. [11] presented numerical results for flow field around two circular cylinders arranged in side-by-side and tandem configuration ($L/D = 2.5$ and 5.5) using the mesh-free least square based finite difference method. The flow simulation were carried out for $Re = 100$ and 200. The flow separation and flow state of the trapezoidal cylinder under low Reynolds number ($Re = 1 - 150$) was analyzed by Dhiman and Hasan [12]. The numerical study of Cung and Kang [13] showed that the Strouhal number of the trapezoidal cylinder depends on the Reynolds number and height ratio, wich is thz ratio of height of the rear face to that of the front face (d/D). The flow without heat transfer behavior past a single cylinder as well as tandem square and circular cylinders in vicinity of a wall with low Reynolds number ($Re = 100$ and 200) was studied numerically by Harichandan and Roy [14]. Their analysis focused on the boundary layer growth and the location of the cylinders parameters. Their results are presented for different parameters to visualize vorticities and streamlines. Similarly, the wall effects on flow structure over two tandem cylinders is studied by Jiang and Lin[15] with low Reynolds number ($Re = 20 - 120$). Ajay Raj Dwivedi et al [16] presented numerical results for the fluid flow and mixed convective (thermal cross-buoyancy) heat transfer of incompressible fluid across identical cylinders organized in a confined tandem configuration. For different gap ration ($S/D = 2.5, 3, 3.5, 4, 5,$ and 5.5) with varying Richardson number ($Ri = 0, 0.5, 1$ and) at Reynolds number 100. Prandtl number $Pr = 0.7$ and wall confinement $\beta = 25\%$. It was found that the fluctuations in lift signal shift from zero average value at $Ri = 0$ towards the nonzero negative average value for the tandem cylinders at $Ri > 0$. The local Nusselt number shows the shift in the front stagnation point on both cylinders with increasing thermal cross-buoyancy. The drag coefficient and Nusselt number of the downstream cylinder are always less than the upstream cylinder, but the percentage increment in the physical parameters of the downstream cylinder after critical spacing is much more the its upstream counterpart. A numerical methods was used by Arif Mentese et al [17] to study the effect of distance between cylinders on flow characteristics for tandem and side-by-side two circular cylinders. It was shown from the numerical results that the flow is almost steady with any vortex in the gap when cylinders are in tandem and the gap between them is low. In contrast, the interactions are strong in case of side-by-side arrangement at the lowest gap ratio. When the gap ratio increase, the flow is affected that results in change on the global parameters. Wei Zhang [18] investigated numerically of flow across two tandem cylinders with rounded corners in a channel at $Re = 100$. The cylinder geometry varies from square to circular by rouding all corners, and the partially rounded cylinders were considered. The effects of gap ratio (GR) characterizing the separting distance of two cylinders and the radius (R) was analyzed at dimensionless parameters ($R^+ = 0 - 0.5$) and $GR = 1 - 8$. They showed that the cylinder geometry determines the unsteadiness of the near-wake after the downstream cylinder, the flow is always unsteady for square-like cylinders where the corner radius is small, while the flow can be stabilized by the circular-like cylinders with larger corner radius that the flow fluctuation is greatly weakened or even fully suppressed at small GRs

After above investigation, it is clear that there is no reported work on the effect of three tandem cylinders on fluid flow and heat transfer in a confined domain with inlet parabolic velocity, the aim of the present study is to add to our scholarship on the relationship of dynamics fields (C_L, C_D) and thermal fields (Nusselt number) with gap ratio and Reynolds number of the forced convection over three tandem cylinders in confined domain with variable boundary condition. A series of computational is conducted for three tandem cylinders with Reynolds number varying from 100 to 200 and gap ratio varying from 2 to 10 with inlet parabolic velocity profile, analyzed and studied in detail through the flow structures and thermal fields in this configuration.

ISSN: 1737-933416

II. Problem description

Briefly the description of the problem is shown in Figure 1. Three identical heated circular cylinders of equal diameter D arranged in tandem whose surfaces are fixed temperature T_w and placed in confined duct, with exposed to a fully developed velocity profile with average velocity u_{avg} and T_∞. Tow adiabatic horizontal walls of finite length are placed at a distance of $H/2$ on either side of the center of the cylinders. The outlet of the duct is specified with Neumann condition. The gap ratio G was defined as $G = S/D$, where S represents the spacing between centre to centre of the cylinders, G was selected as 2 to 10. The flow was described in a Cartesian coordinated system (x and y). The upstream and downstream distances of computational domain are gives respectively by the values $L_u = 10D$ and $L_d = 48D$. The blockage ratio of the computational domain is given as: $\beta = D/H = 0.25$. It is also considered that the flow unsteady laminar regime with constant thermo-physical proprieties.

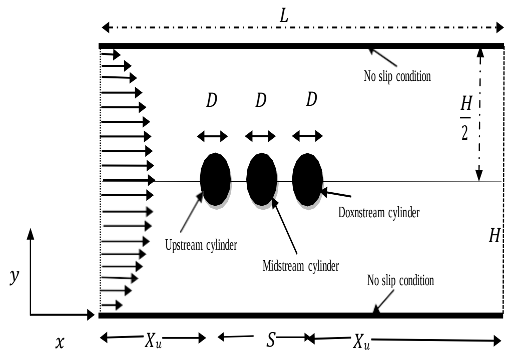

Fig.1 Computational domain and three cylinders configuration.

III. Governing equations and boundary conditions

The governing equations, for unsteady incompressible viscous flow with constant thermophysical properties in two-dimensional Cartesian coordinate are expressed as follows:

For continuity

$$\frac{\partial u_x}{\partial x} + \frac{\partial u_y}{\partial y} = 0$$

For the momentum

$$\frac{\partial u_x}{\partial t} + u_x \frac{\partial u_x}{\partial x} + u_y \frac{\partial u_x}{\partial y} = -\frac{1}{\rho}\frac{\partial p}{\partial x} + v\left(\frac{\partial^2 u_x}{\partial x^2} + \frac{\partial^2 u_x}{\partial y^2}\right)$$

$$\frac{\partial u_y}{\partial t} + u_x \frac{\partial u_y}{\partial x} + u_y \frac{\partial u_y}{\partial y} = -\frac{1}{\rho}\frac{\partial p}{\partial y} + v\left(\frac{\partial^2 u_y}{\partial x^2} + \frac{\partial^2 u_y}{\partial y^2}\right)$$

Ffor the energy

$$\frac{\partial T}{\partial t} + u_x \frac{\partial T}{\partial x} + u_y \frac{\partial T}{\partial y} = \alpha\left(\frac{\partial^2 T}{\partial x^2} + \frac{\partial^2 T}{\partial y^2}\right)$$

Where u_x, and u_y are the dimensionless velocity components along $x-$ and $y-$directions of a Cartesian coordinate system, respectively, p is the dimensionless pressure, v is the kinematic viscosity, ρ is the density, T is the temperature of the fluid, and α is the thermal diffusivity defined as $k/\rho c$ where is k the thermal conductivity and is the c specific heat of the fluid.

The computational domain and the configuration of the circulars cylinders are illustrated in Fig.1. The boundary conditions for the inlet, outlet, walls and surface of cylinders can be written as:

For the inlet: A fully developed $2-D$ parabolic velocity profile

$$u_x = 1.5u_{avg}\left(1 - \left(1 - \frac{2Dy}{H}\right)^2\right)$$

Where $0 \le y \le H/D$, $u_y = 0$, $T = T_\infty$

For the outlet: $\frac{\partial u_x}{\partial x} = \frac{\partial u_y}{\partial y} = \frac{\partial T}{\partial x} = 0$

For the Bottom and top: $\frac{\partial T}{\partial x} = 0$, $u_x = u_v = 0$

For the cylinders walls: $u_x = u_v = 0$, $T = T_w$
Were u_{avg}, T_∞ are the average velocity and stream temperature respectively and T_w is the cylinder wall temperature. One of the key parameters in the present study is the Reynolds number, Eq. 9.

$$R_e = \frac{\rho u_{avg} D}{\mu}$$

This numerical study reveals the influence of Reynolds number and the space between the cylinders on lift coefficient (Eq.10), drag coefficient (Eq.11), and Nusselt number (Eq.12) since these coefficients deliver important information about flow characteristic and heat transfer by forced convection.
Overall mean drag and mean lift coefficient was mathematically defined as:

$$C_D = \frac{F_D}{\frac{1}{2}\rho u_{avg}^2 D}$$

$$C_L = \frac{F_L}{\frac{1}{2}\rho u_{avg}^2 D}$$

Where, F_D and F_L are the force components in the longitudinal and transverse directions respectively.

In the present study, the local Nusselt number is defined based on the cylinder diameter D as the length scale:

$$-k\frac{\partial T}{\partial n}\Big|_w = h_\theta (T_w - T_\infty)\ ,\ Nu_\theta = \frac{h_\theta D}{k}$$

Where, h_θ is the local surface heat transfer coefficient, and n is the direction perpendicular to the cylinder wall. The average Nusselt number at the cylinder wall is calculated by integrated of the local Nusselt number over the cylinder surface.

$$\overline{N_u} = \frac{1}{2\pi}\int_{\theta=0}^{\theta=2\pi} Nu_\theta \, d\theta$$

IV. Numerical methods and simulation conditions

In this study, the governing flow and energy equations with its boundary conditions have been solved numerically by the finite volume method using the ANSYS Fluent, the ANSYS work-bench was used to generate structured quadrilateral cells of uniform and no-uniform grid spacing as shown in Fig.1.
The tow-dimensional, unsteady, laminar, segregated solver was used to solve the equations of the incompressible flow on the collocated grid a arrangement. A Semi-Implicit Method for Pressure Linked Equation algorithm (SIMPLE) is used for the velocity-pressure coupling. QUICK (Quadratic Upstream Interpolation for Convective Kinematics) scheme was used to discretize the convective terms in the momentum and energy equations. The second order implicit time-integration scheme was used to solve the evolved transit condition with dimensionless time step Δt of0.01, which was fixed after a time-dependent study indicates that any decrease in the time step size has negligible effect on the values of the global flow and heat transfer characteristics. The software Fluent uses the Gauss-Seidel point by point iterative method in combination with the algebraic multi-grid method to solve the system of algebraic equations. The inlet velocity input (Eq. 6) is specified by exploiting the by user-defined function (UDF) accessiblein ANSYS Fluent.
In the current computations, we divided the domain into structured mesh with fin clustering distributions in the vicinity of the cylinders surface, top and bottom walls to control the sharp velocity, temperature and pressure gradients near the surfaces of the cylinders and walls and of course these deviations it should not be excessively computationally intensive. Therefore, a grid independency test has been performed using the gap ratio GR=4 and 10 for R_e=100 and three quadrilateral grid which are differentiated by the number of points on the surface of cylinders (N_i), the value of (δ⁄D) near the surface of the cylinders. we was found that the N_i=200 and (δ⁄D=0.005) is sufficient to conduct the following numerical simulations with conditions used in this work.
In unsteady flow numerical simulations results also depend on the time interval. In this study, three different dimensionless time intervals: Δt=0.1, 0.01 and 0.005 is used to determine an optimum value which resulted in less computational time, yet sufficiently accurate solutions. Finally a dimensionless time step size of 0.01 which was adapted in this study.

ISSN: 1737-933416

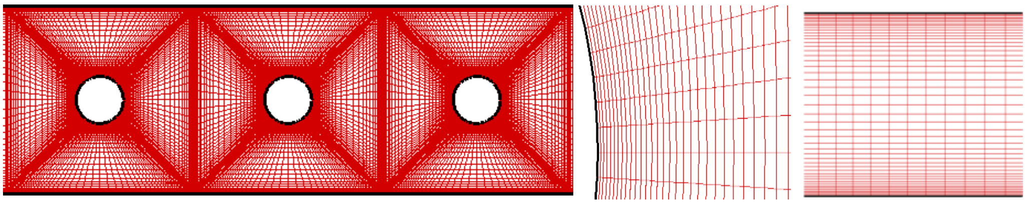

Fig.2 Magnified view of a grid structure around the three tandem cylinders ($GR = 4$)

V. Results and Discussion

This section starts with presentation and discussion of the validation study, before systematize the results obtained by this numerical simulation in the form of streamline, vorticity and isotherm contours along with drag coefficient, lift coefficient and Nusselt number (local and surface average).

A. Validation study

A validation is performed before solving the present problem to demonstrate and confirm the precision of the results reported in this study. For this purpose figure 2 and Table 1 compares the numerical results of Ajay Raj Dwivedi and Amit Kumar Dhiman [16] to our numerical results for for two identical circular cylinders in the case of parabolic inlet velocity at gap ration GR=4 for Re=100 and Pr=0.7, the comparison of the results through the values of mean drag and lift coefficients and average Nusselt numbers for both upstream and downstream cylinders. Figure 2 and Table 1 shows excellent agreement between the findings, confirming the veracity of our numerical results.

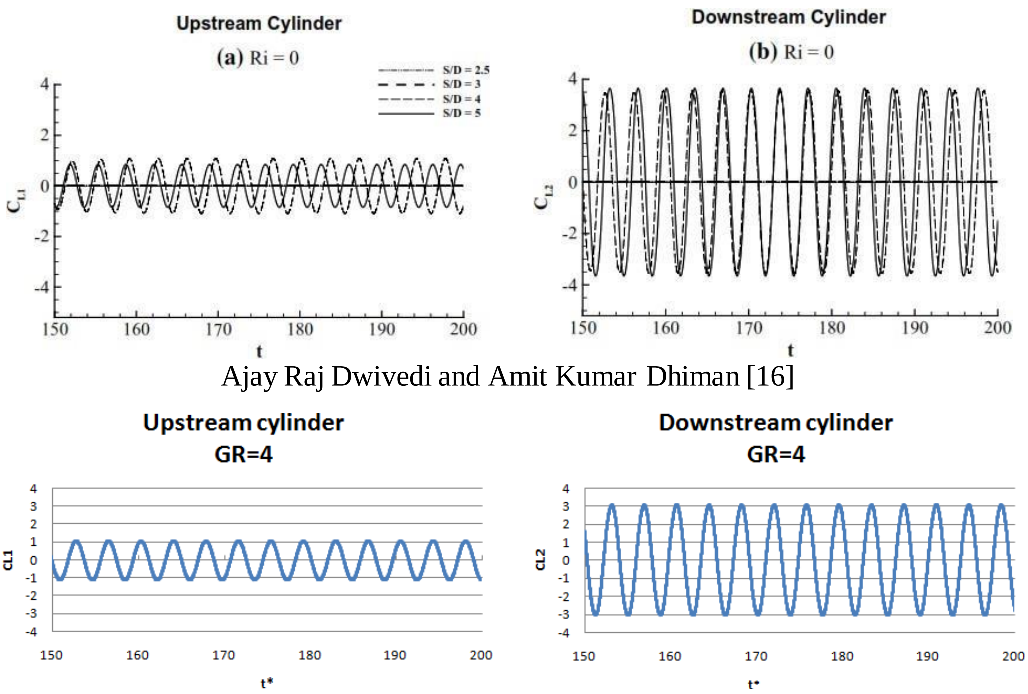

Present study

Fig.3 Comparison between the present and literature values of the time histories of lift coefficients and for a two tandem confined cylinders at $Re = 100$, GR=4 and $Pr = 0.7$.

Table 1 Comparison between the present and literature values of the mean drag coefficients and average Nusselt number for a two tandem confined cylinders at $Re = 100$, GR=4 and $Pr = 0.7$.

References	*Present study*	*Ajay Raj Dwivedi and Amit Kumar Dhiman [16]*
C_{D1}	*2.9684*	$\approx$ *2.97*
C_{D2}	*2.4832*	$\approx$ *2.49*

ISSN: 1737-933416

Nu_1	*6.368*	$\approx$ *6.38*
Nu_2	*5.260*	$\approx$ *5.53*

B. Streamlines, vorticity and isotherms contours

Streamline and vorticity contours it is one of the keys to understanding the flow regimes, this flow regimes it is divided into three regimes depending on the gap ratio G: (a) the extended-body regime ($G < 1.2 - 1.8$) in this range the free shear layers separated from the upstream cylinder overshot the downstream cylinder. (b) reattachment regime, ($1.2 - 1.8 < G < 3.4 - 3.8$) in this range the shear layers reattached on the downstream cylinder, and (c) the co-shedding regime ($G > 4$) and the shear layers rolled up alternately, forming a vortex street in the gap between, as well as behind, the cylinders, like's reported by Zdravkovich (1977).

Figure 4, figure 5 and figure 6 show streamlines, vorticity and isotherms in the computational domain respectively, both figures reveal that the gap ratio between cylinders has significant great impact of the mechanism of flow and thermal patterns evolution around tandem circular cylinders. The dependence of instantaneous streamlines near the cylinders for different spacing ratios at Re=100 obtained at dimensionless time t*=225 are shown in Figure.4. It can be assessed that the flow behaves as steady for GR<4 and the flow filed obtained is symmetric about the mid-plane with formation of twin vortices are observed. For GR=3 the flow remains steady, whereas the centers of symmetric recirculation zones in gap region move toward inside slightly due to the increasing driven effect from the free stream flow. With increasing the gap ratio (GR≥4) The shear layer from the front cylinder reattaches on the rear cylinder at some point. After impinging on the rear cylinder, this shear layer is divided into two parts and transported away and detaches from the lower and upper part of the rear cylinder. The detached layer once again impinged on the lower part of the rear cylinder. The flow patterns in the gap and around the cylinders strongly depend on the cylinder spacing and this is confirmed by figure 5.

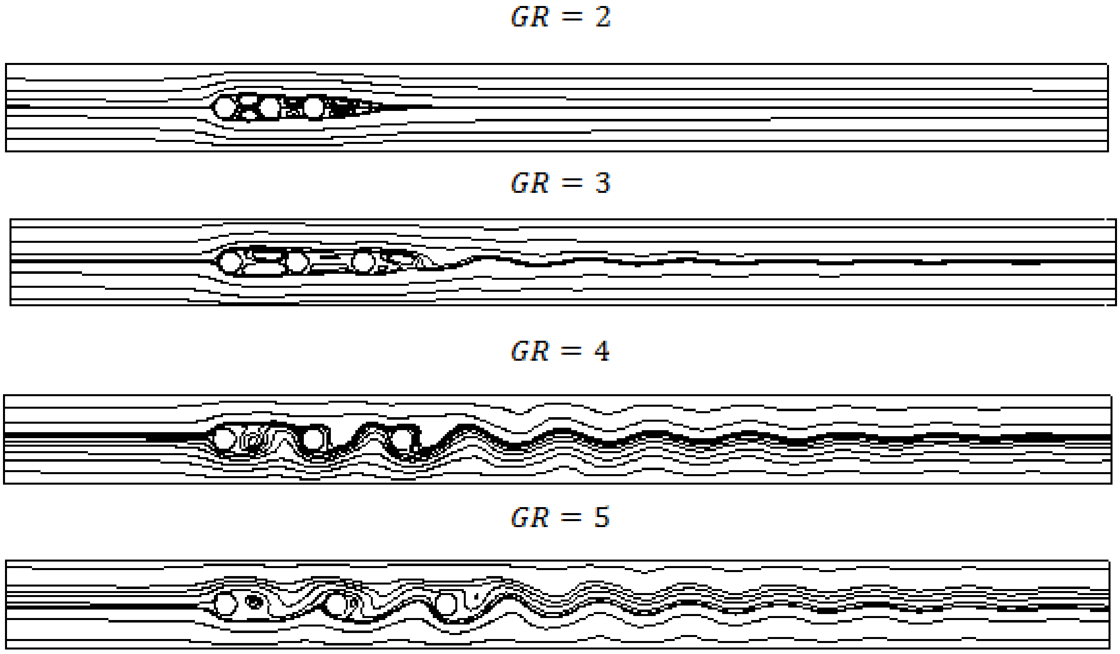

Fig.4 Streamlines around three cylinders in tandem arrangement for different spacing ratios at $Re = 100$ with $t^* = 225$.

The instantaneous vorticity contours around three tandem cylinders are shown in Figure.5, these contours are plotted for different spacing ratios at Re=100 and at dimensionless time t*=225. As can be seen in this figure, the vorticity contours become more complex with increasing the spacing. The wake structure behind the cylinders strongly depends on the spacing ratio. There is no vortex shedding from the cylinders at GR=2 and GR=3. It is observed that for GR≥4, the generated vortices are more obvious. For small gap ratio (Gr<4) the flow is steady and shear layers detached from the first and second cylinder do not form vortex shedding upstream of the second and third cylinders respectively. Vortices are formed in between the cylinders and behind the third cylinder and the formation of vortex shedding for both cylinders occurs only after GR≥4. We can observed that the flow remains steady until GR <4, but at GR ≥ 4 the flow becomes unsteady and at this gap ratio the fluid separates from the first, second and third cylinder and it is seen that in this instability, a couple of eddies is developed, and is shed alternately in the downstream direction with two row vortex street. These results mean that at high gap ratios ($G \geq 4$) the shear layer from the first cylinder top surface reattaches on the surface of the second cylinder and is divided into two parts as well the shear layer from the second cylinder top surface reattaches on the surface of the third cylinder and is divided into two parts , where one will be moving through the gap between the cylinders and the other over the third cylinder. Overall, the flow is characterized by the formation of the Ka´rma´n vortex street behind the third cylinder.

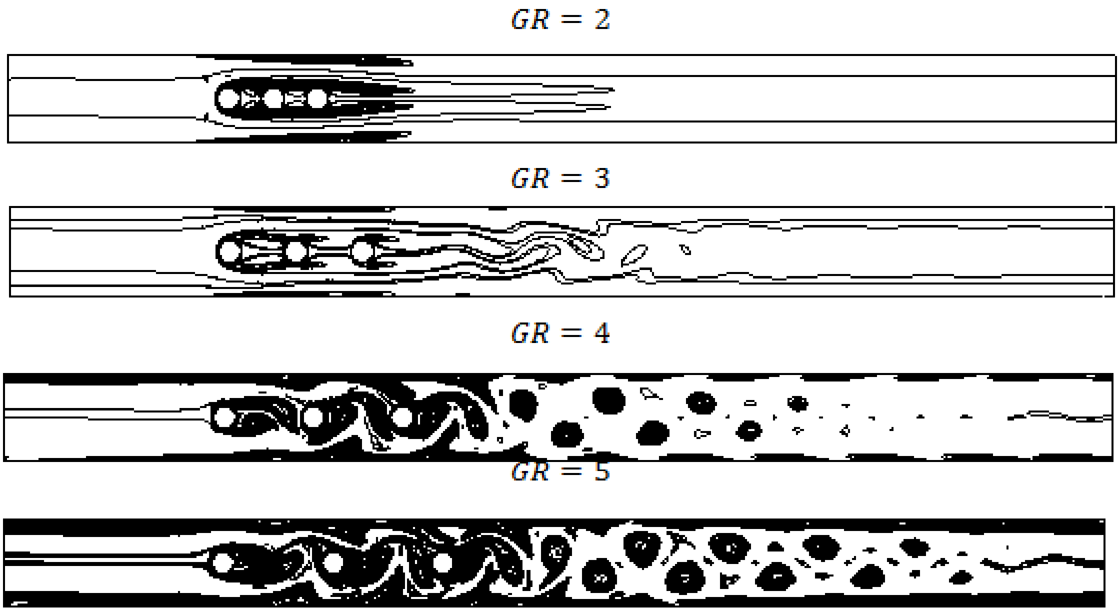

Fig.5 Vorticiy around three cylinders in tandem arrangement for different spacing ratios at $Re = 100$ and $t^* = 225$.

Figure 5 shows the temperature contours gap ratio. The vorticity transport characteristics are indicative of the thermal transport. Accordingly, it is seen from figure 5 that the characteristic feature of the isotherms are similar to the vorticities evolving. Most of the isotherms are clustered around both the cylinder surfaces resulting in maximum heat transfer on the front stagnation point for first, second and for third cylinder maximum heat transfer location are at two points where thermal and hydrodynamic boundary layer thickness becomes thin for GR=2, 3 and for GR>3 (after reattachment), maximum heat transfer (cluster of isotherms) for first cylinder also shifts to its front stagnation point. There is a uniform temperature field between the cylinders for lower gap spacing. However, when the spacing increases, an unsteady temperature pattern is observed between the cylinders.

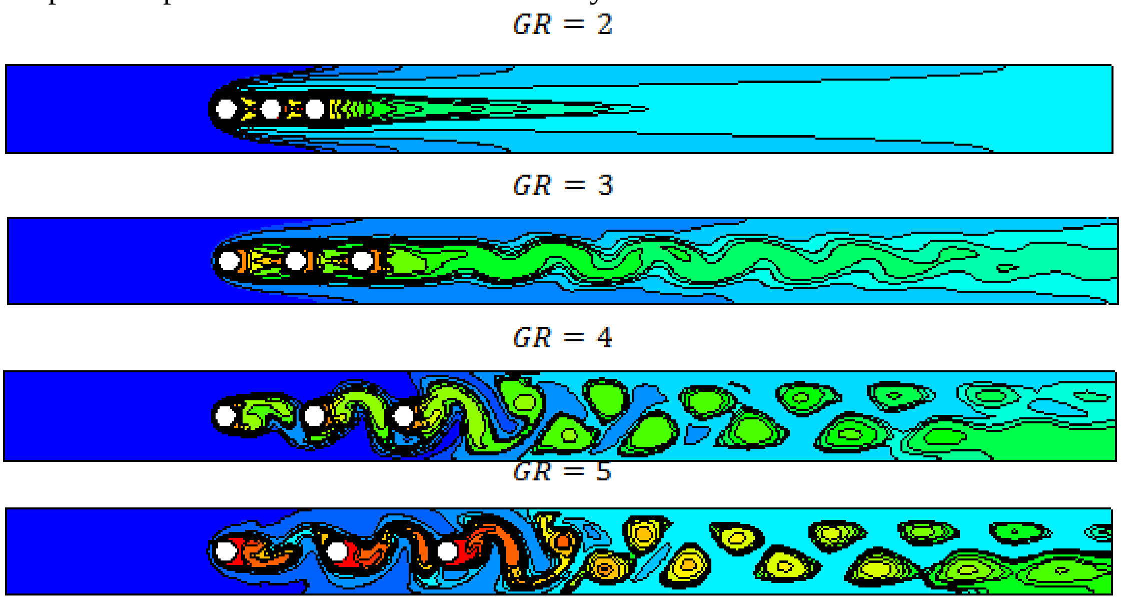

Fig 6. Isotherms around three cylinders in tandem arrangement for different spacing ratios at $Re = 100$ with $t^* = 225$.

ISSN: 1737-933416

B. Variation of lift and drag coefficients with gap ratio

Figure 7 and 8 shows results for time histories of the lift and Drag coefficient of three circular cylinders in the range of GR= 2 to 5 at Re =100 respectively. The amplitudes of time histories of CL and CD at GR=2 are quite small because the vortex street behind the cylinders is not formed as seen in figure 5.

The CL and CD amplitudes of the first cylinder is small relative to that of the second and third cylinder. No vortices are shed from the first and second cylinder, and the CL fluctuation of the first and second cylinder is induced by the movement of the first and second cylinder shear layers. The CL fluctuation of the second and third cylinder is caused by the alternate reattachment of the first cylinder shear layers, as well as by the vortex shedding from the first and second cylinder.

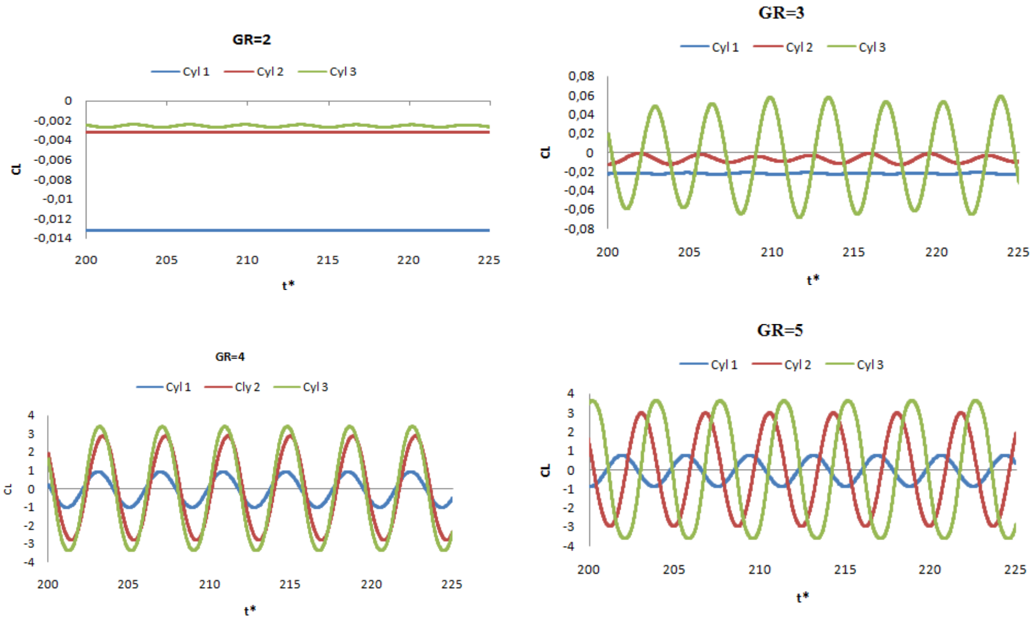

Fig.7 Time histories of lift for first, second and third cylinders at different gap ratios.

However, in the range of GR>3, it is observed that fluid forces of the third cylinder which is located in the wake of the first and second cylinder are very much larger than those of the windward cylinder because the vortex shedding behind two cylinders has a strong influence on the amplitudes of CD and CL. It is possible to clearly catch the phenomena that the flow patterns behind the windward cylinder and the fluid forces of three circular cylinders change suddenly at the spacing ratio of approximately GR=4 which is well known as the critical spacing ratio.

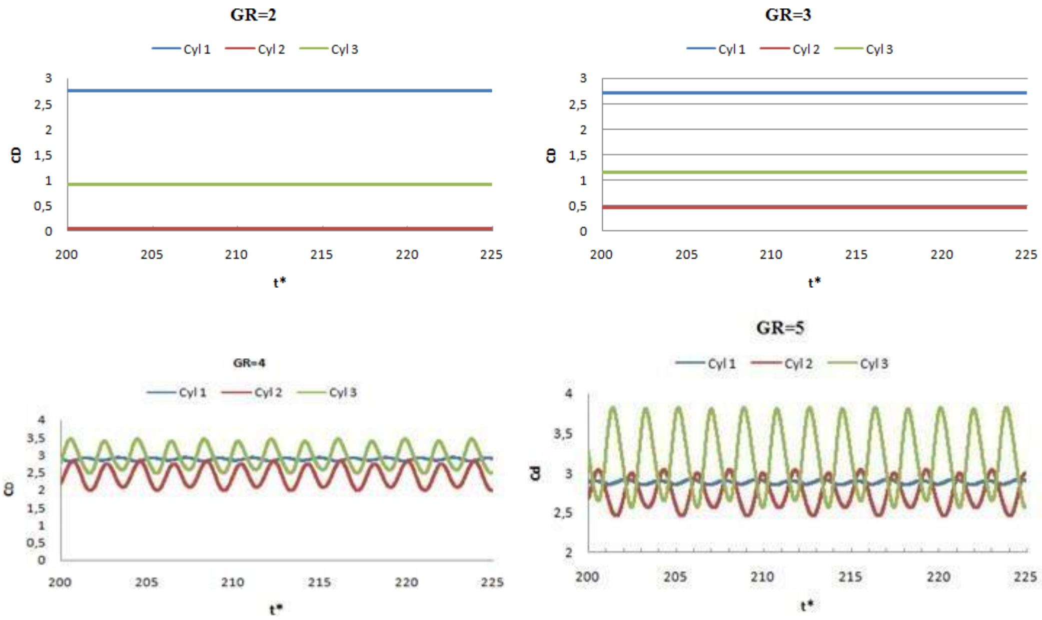

Fig.8 Time histories of Drag force acting on the cylinders for different gap ratios at Re=100.

C. *Local Nusselt number variations*

The local Nusselt number on the first, second and third cylinder surface is plotted as a function of circumferential direction ð for different gap ratios are shown in Figure.5. It can be deduced from this figure that the local Nusselt number is greatest at the front portions of the cylinders. Since heat transfer rate is closely related to flow structure, the minima of the local heat transfer rates appear in the front and back stagnation points of the second and third cylinder where the velocity magnitudes are relatively small for Gr=2 and 3. The local Nusselt number distribution of the second and third cylinder resembles to that of first cylinder typified for Gr=4 and 5. The maximum heat transfer from first cylinder occurring at θ=45 and 360 of the cylinder wall for all values of gap ratios. The maximum heat transfer from second and third cylinder exhibits itself with a double hump occurring at θ=115 and 240 of the cylinder wall at GR=2 and 3 where the thermal and hydrodynamic boundary layers become the thinnest.

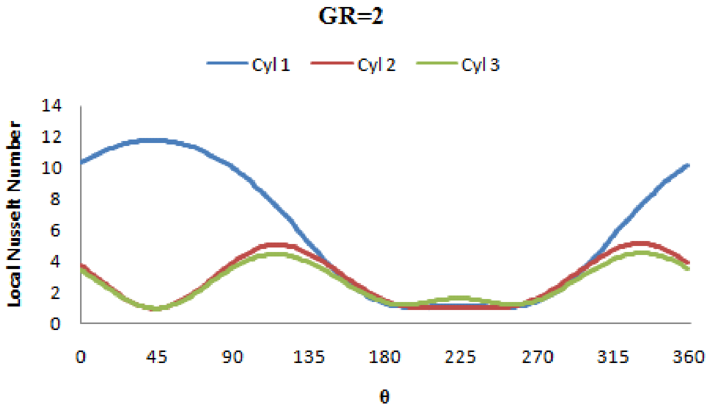

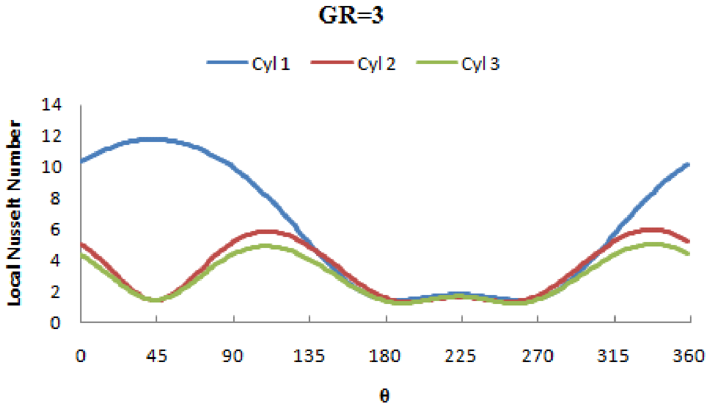

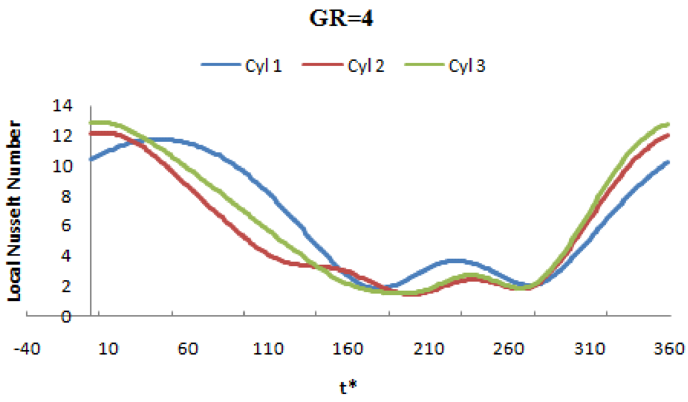

ISSN: 1737-933416

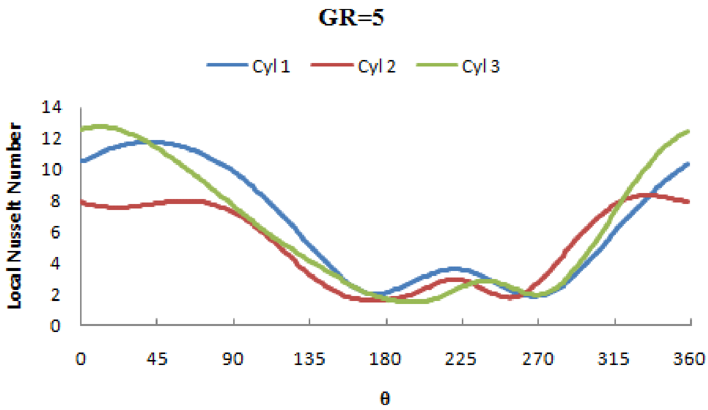

Fig 10. The local Nusselt number distribution on the first, second and third cylinder at $Re = 100$ and $t^* = 225$.

D. Average Nusselt numbers

Figure 11 shows the variation of the mean Nusselt number of the three whole cylinders with the spacing ratio at Re=100. It can be deduced from this figure that the level of Nusselt number for first cylinder is higher than the corresponding value for the second and third cylinder. The heat transfer from the second and third cylinder increases with increase in the gap ratio for 2 to 3 and it decreases for GR>4. It can also be pointed out that the mean Nusselt number for the third cylinder is always less than its second counterpart for Gr<4. In general, the global transport of heat quantities have larger values for the fiest cylinder compared to the second and third cylinder, and at lower cylinder spacing the difference is more; however, at larger spacing this discrepancy is substantially reduced.

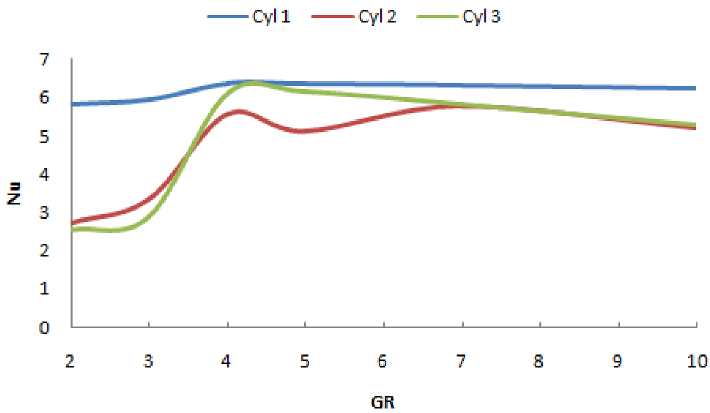

Fig.11 Mean Nusselt number of the first, second and third cylinder for different gap ratio.

VI. CONCLUSIONS

A two-dimensional numerical study is reported addressing the laminar flow and heat transfer around three circulars cylinders in tandem arrangements with variable boundary condition in semi confined media. Three identical heated circular cylinders of equal diameter D arranged in tandem whose surfaces are fixed temperature T_w and placed in confined duct, with exposed to a fully developed velocity profile with average velocity u_{avg} and T_∞ at Reynolds number equal to 100. Tow adiabatic horizontal walls of finite length are placed at a distance of $H/2$ on either side of the center of the cylinders. The outlet of the duct is specified with Neumann condition. The gap ratio GR was selected as 2 to 5. One of the objectives is to understand the critical gap ratio at which the unsteady flow and thermal fields are transformed into a steady pattern. The results of simulation show that beyond the critical gap ratio (GRcr) there is a stabilization in the flow and thermal fields. The main findings are summarized below:

The gap between cylinders has crucial impact on flow patterns, when cylinders are very close to each other, the flow regime is steady in gap area and no vortex shedding occurs. After the critical gap (GR=4), a vortex shedding forms in the gap while double row vortex streets are observed behind the third cylinder as the gap increases.

The vorticity and isotherms were obtained to understand and interpret the flow and heat transport. For GR≥4, the vortices and isotherms are in unsteady behaviour irrespective of the gap spacing.

It is observed that fluid forces of the third cylinder which is located in the wake of the second cylinder are very much larger than those of the first cylinder.

The local Nusselt number is greatest at the front portions of the cylinders. The heat transfer from the second and third cylinder increases GR<4 and it decreases for GR ≥4. The heat transfer rate from the second and third cylinder is about 80% and 90% of that of the first cylinder respectively.

References

[1] Igarashi, T. (1981). Characteristics of the flow around two circular cylinders arranged in tandem: 1st report. Bulletin of JSME 24(188),323–331.
[2] Igarashi, T. (1984). Characteristics of the flow around two circular cylinders arranged in tandem: 2nd report, unique phenomenon at small spacing. Bulletin of JSME 27(233), 23802387.
[3] Zdravkovich, M. (1987). The effects of interference between circular cylinders in cross flow. Journal of fluids and structures 1(2), 239-261.
[4] D. Sumner, “Two circular cylinders in cross-flow: a review,” Journal of Fluids and Structures, vol. 26, no. 6, pp. 849–899, 2010
[5] Jiang, R.J., Lin, J.Z.: Wall effects on flows past two tandem cylinders of different diameters. J. Hydrodyn. 24, 1–10 (2012)
[6] A. Sohankar and A. Etminan, “Forced-convection heat transfer from tandem square cylinders in cross flow at low Reynolds numbers,” International Journal for Numerical Methods in Fluids, vol. 60, no. 7, pp. 733–751, 2009.
[7] Lin, J., Jiang, R., Chen, Z., Ku, X.: Poiseuille flow-induced vibrations of two cylinders in tandem. J. Fluid Struct. 40, 70–85(2013)
[8] [8] J. L. Rosales, A. Ortega, and J. A. C. Humphrey, A Numerical Simulation of the Convective Heat Transfer in Confined Channel Flow Past Square Cylinders: Comparison of Inline and Offset Tandem Pairs, Numer. Heat Transfer A, vol. 38, pp. 443–465, 2000.
[9] J. L. Rosales, A. Ortega, and J. A. C. Humphrey, A Numerical Simulation of the Convective Heat Transfer in Confined Channel Flow Past Square Cylinders: Comparison of Inline and Offset Tandem Pairs, Int. J. Heat Mass Transfer, vol. 44, pp. 587–603, 2001.
[10] N. Mahir, Z. Altac, Numerical investigation of convective heat transfer in unsteady flow past two cylinders in tandem arrangements, Int. J. Heat Fluid Flow 29 (2008) 1309-1318.
[11] Ding, H., Shu, C., Yeo, Y.O., Xu, D., 2007. Numerical simulation of flows around two circular cylinders by mesh-free least square-based finite difference methods, Int. J. Numer. Meth. Fluids 53, 305–332.
[12] A. Dhiman and M. Hasan, “Flow and heat transfer over a trapezoidal cylinder: steady and unsteady regimes,” AsiaPacific Journal of Chemical Engineering, vol. 8, no. 3, pp. 433–446, 2013.
[13] Y. J. Chung and S.-H. Kang, “Laminar vortex shedding from a trapezoidal cylinder with different height ratios,” Physics of Fluids, vol. 12, no. 5, pp. 1251–1254, 2000.
[14] A. Harichandan, and A. Roy, "Numerical investigation of flow past a single and tandem cylindrical bodies in the vicinity of a plane wall", Journal of Fluids and Structures, vol. 33, pp. 19–43, 2012.doi: 10.1016/j.jfluidstructs.2012.04.006.
[15] R.J. Jiang, and J.Z. Lin, "Wall effects on flows past two tandem cylinders of different diameters", Journal of Hydrodynamics, vol. 24, pp. 1-10, 2012. doi: 10.1016/s1001-6058(11)60212-6.
[16] Ajay Raj Dwivedi and Amit Kumar Dhiman. Flow and heat transfer analysis around tandem cylinders: critical gap ratio and thermal cross-buoyancy. Journal of the Brazilian Society of Mechanical Sciences and Engineering (2019) 41:487
[17] Arif MENTEŞE , Seyfettin BAYRAKTAR. Numerical investigation of flow over tandem and side-by-side cylinders. Seatific 2021;1:1:15–25.
[18] Wei Zhang et al. Forced convection for flow across two tandem cylinders with rounded corners in a channel. International Journal of Heat and Mass Transfer 130 (2019) 1053–1069.
[19] Zdravkovich, M.M., 1977. Review of flow interference between two circular cylinders in various arrangements. Trans. ASME J. Fluids Eng. 99, 618–633.

ISSN: 1737-933416

USE of LICHENS for the QUALITATIVE and QUANTITATIVE ASSESSMENT of AIR QUALITY in the Annaba REGION

Amina CHAKER#1, Kheireddine FEKROUNE#2, Sameh BOUKHDIR#3, Labiba ZERARI#4, Khaoula Abdelli#5

[1, 3, 4, 5] *Department of Biology, Faculty of Sciences, University of Badji Mokhtar of Annaba, Algeria*

[1]amina.fekrounechaker@yahoo.fr

[3]samehboukhdir@gmail.com

[4]hortansia23@gmail.com

[5]khawlabdelli66@gmail.com

[2] *Department of Biology, Faculty of Nature and Life Sciences, University of Chadli BenDjeddid of El Tarf, Algeria*

[2]kfekroune@gmail.com

Abstract— It is possible to assess air quality using measuring apparatus, but physical collectors remain expensive equipment. Lichens were recognised as potential indicators of air pollution as early as the 1860s in Great Britain and the rest of Europe, so they were used for qualitative or quantitative assessment of the air quality of a given area. Hence, qualitative methods (the method of Van Haluwyn and Lerond (1986) [1], the illustrated scale of Dalby (1981)[2] and the scale adapted by Tiévant (2001)[3]) and a quantitative method (atmospheric purity index) of Leblanc and De Sloover (1970)[4] were used for the estimation of the air quality of the Annaba region, which allowed us to classify the stations studied according to the evaluation of the SO_2 rate (µg/m^3). From the most polluted stations (such as the city centre) to the least polluted stations (the reference station, the Edough mountain or Edough Peninsula). This montain abounds in fruticose species (Ramalina sp.) and foliose species, particularly those that are toxiphobic such as Lobaria pulmonaria. It is possible to monitor the evolution of the air quality of a region by following the evolution of its lichenic flora.

Keywords— Lichens, qualitative methods, quantitative method, pollution, assessment, Annaba.

I. INTRODUCTION

Lichens are made up of fungi and algae living in true symbiosis: one cannot live without the other [3]. This lichenic symbiosis is a permanent and harmonious association from the structural point of view, balanced and beneficial from the nutritional point of view for both partners: algae and fungi [5]. Because sulphur dioxide (SO_2) pollution is the easiest to detect and study, it is considered the main "tracer" of atmospheric and urban pollution [6]. Reference [7] lists certain characteristics of lichens that have led authors ([8] or [9]) to recognise lichens as good bioindicators of air quality, such as their particular sensitivity to certain pollutants or an easily observable way of reacting, etc. Thus, lichens make it possible to establish an extensive and inexpensive observation network in both space and time [7]. It is in this context that we proposed to use lichen species as biological indicators of air pollution in the Annaba region. To do so, we have different qualitative and quantitative methods.

II. THE STUDY AREA

The city of Annaba is located in the east of Algeria, between latitudes 36°30' North and 37°30' North, and longitudes 07°20' East and 08°40' East, with 12 communes with a total area of 1,411.98 km^2. It is delimited by the Mediterranean Sea to the North, the wilaya of Skikda to the West, Guelma to the south and El-Tarf to the east [10]. It is the industrial capital of eastern Algeria and has long been subjected to various types of pollutants that spare neither humans nor animals, let alone plants ([11], [12], [13], [14]).

Five stations were the subject of our study in the Annaba region (Fig. 1):

ISSN: 1737-933422

Station 1: Fertial (Algerian Fertiliser Company), which is located in the immediate vicinity of the Fertial Annaba complex (road of the salt flats W56). This phosphate and nitrogen fertiliser complex is the main source of fluorinated atmospheric emissions (latitude: 36.866058º longitude: 7.767669º)

Station 2: Boukhadra, EL-Bouni, which is located at the entrance of the city Boukhadra, EL-Bouni, and is exposed to the north-east wind coming from Fertial (latitude: 36.871220º, longitude: 7.74801º)

Station 3: (city centre)

Sub-station 1: The Edough Square (north) in the centre of Annaba (latitude: 36.909359º, longitude: 7.756934º),

Sub-station 2: The Christian Cemetery (latitude: 36.970322º, longitude: 7.756702º)

Station 4: Bouhdid Cemetery (latitude : 36.88934º, longitude : 7.712582º)

Station 5: Cork oak forests (northern slopes) of the Edough mountain (latitude: 36.551164°, 7.41555468°).

III. MATERIAL AND METHODS

Sampling was carried out on 6 trees, diversifying the tree species according to the trees available in the selected stations), in order to optimise the representativeness of lichen diversity [15]. The survey is carried out on the four sides of each tree using an observation grid consisting of five 10×10 cm meshes superimposed vertically. The grid is placed at least 1m high to avoid any disturbance of the ground (Fig. 2). To determine the frequency of each lichen species, their possible presence in the different grid cells of the observation grid is noted, i.e. a frequency ranging from 0 (species absent) to 5 (species present in all grid cells).

These frequencies are indicated for each side of the tree on a field sheet, which also mentions the geographical coordinates of the phorophytes

The Air quality of the Annaba region was assessed using qualitative and quantitative methods by means of lichen flora.

In the field, lichens are collected by hand or with the help of a knife to gently remove a piece of bark that supports the thallus (Van Haluwyn et al, 2013). The collected lichens will be individually wrapped in absorbent paper and placed in small plastic boxes on which we note the date, station, as well as phorophyte (Tiévant, 2001; Van Haluwyn et al., 2013; Asta et al., 2016).

The identification of lichens is carried out in the field and continued in the laboratory using a binocular magnifying glass and the usual thallin reactions.

The following references (guidebooks and websites) were used for the identification of lichens:

Guide des Lichens de France, Lichens des arbres [16], Guide des Lichens, 350 espèces de lichens d'Europe [3], Images of British Lichens [17], and specialised websites ([18], [19]).

The lichens identified follow the nomenclature of reference [20].

Qualitative methods:

The scale for estimating air quality in northern France according to the Method of Van Haluwyn et Lerond (1986) [1]

The Illustrated Scale of Dalby (1981) [2]

The scale adapted by Tiévant (2001) [3]

Quantitative methods:

The method of I.A.P. (Index of Atmospheric Purity) of Leblanc et De Sloover (1970) [4].

The method for calculating Lichenic Diversity per Station (LDS). It is a quantitative method that consists of calculating the lichen diversity in each station (DLS) and to do this it is first necessary to calculate the lichen diversity in each tree (DLA). To carry out these calculations, it is first necessary to identify each species present in the grid and then count the number of cells in which the lichen species is present. A frequency score ranging from 0 to 5 is then obtained [21].

Lichen diversity per tree:

LDT = SFnorth + SFeast + SFsouth + SFwest where SF: sum of frequencies

Lichenic diversity per station:

LDS = (DLA1 + DLA2 + DLA3 + DLA4 + DLA5 + DLA6) / 6

Fig. 1 Study stations in the region of Annaba

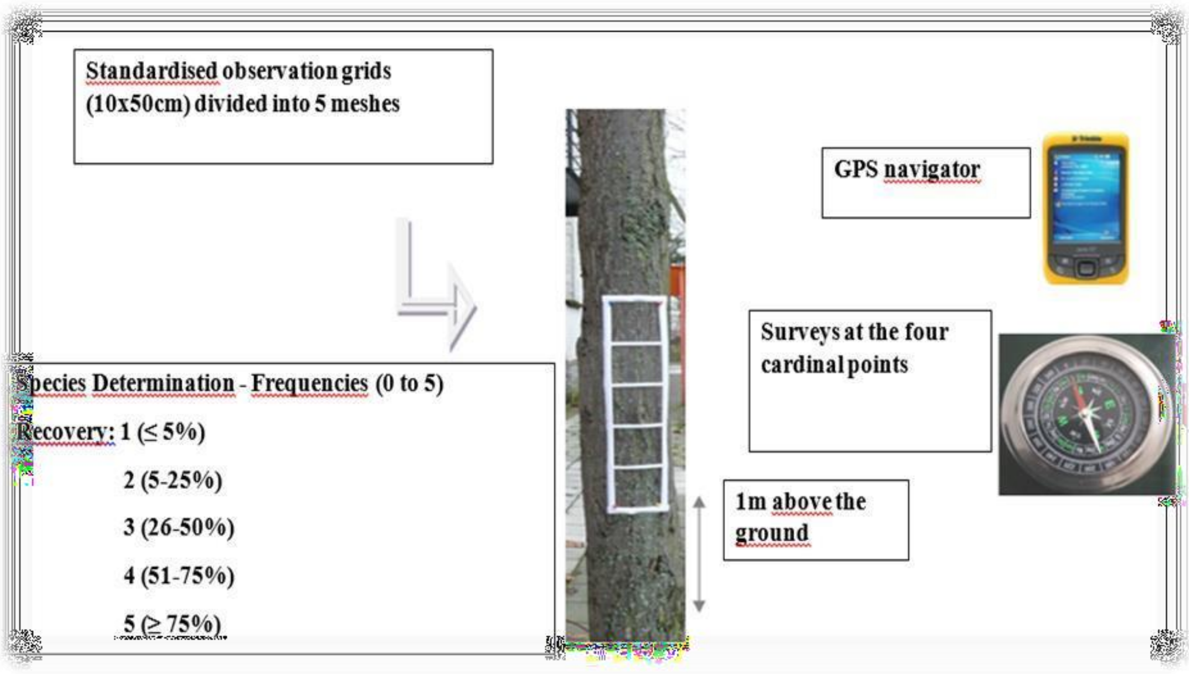

Fig. 2 Experimental protocol (according to [22])

ISSN: 1737-933422

IV. RESULTS AND DISCUSSION

The results relating to the lichenic flora of the stations studied in the Annaba region are expressed according to the physiognomy (type of thallus: foliose, crustose.. etc (Fig. 3)) and according to the systematic classification (orders, families and genera (Fig. 4)).

The first station is poor in lichens. We note the presence of the green alga Pleurococcus viridis and Nostoc ssp., the absence of fruticulous lichens and the codominance of the crustose lichen Lecanora conizaeoides and the foliose lichen, *Xanthoria parientina*, a nitrophilic lichen (roadside as is the case of station 1). These two lichenic species still belong to two different orders and families (Tab. 1).

TABLE 1
THE LICHENIC FLORA OF STATION 1

n°	Name of species	Order	Family	Type of thallus	Substratum
1	*Xanthoria parietina* (L.) Th. Fr.	Teloschistales	Teloschistaceae	Foliose	*Cupressus sempervirens*
2	*Lecanora conizaeoides* Nyl. ex Cromb.	Lecanorales	Lecanoraceae	Crustose	*Cupressus sempervirens*

Unlike green plants, lichens have no cuticle and therefore no stomata and therefore no means of regulating their exchanges with the atmosphere. Thus, in the event of atmospheric pollution, however slight, they absorb the pollutants, which may even cause them to disappear. This is why lichens can be used as bio-indicators of air quality [24].

In the second station, a low number of lichens (4 species) and the dominance of the foliaceous thallus type was observed: *Xanthoria parientina*, *Physconia grisea*, *Physcia adscendes* being all nitrophilic lichens, quite toxic-tolerant (very common in urban areas as the case of station 2). On the other hand, the fourth species *Parmeliopsis ambigua*, which is a nitrophobic lichen, was only encountered once (a single specimen on an olive tree very far from the roadside). The lichens recorded in station 2 (Boukhadra) are grouped into 2 orders only: Teloschistales (75%) and Lecanorales (25%), and two families: Teloschistaceae and Parmeliaceae (Tab. 2).

TABLE 2
THE LICHENIC FLORA OF STATION 2

n°	Name of species	Order	Family	Type of thallus	Substratum
1	*Physcia adscendens* (Fr.) H. Olivier	Caliciales	Physciaceae	Foliose	*Olea europea*
2	*Xanthoria parietina* (L.) Th. Fr.	Teloschistales	Teloschistaceae	Foliose	*Olea europea*
3	*Physconia grisea* (Lam.) Poelt	Caliciales	Physciaceae	Foliose	*Olea europea*
4	*Parmeliopsis ambigua* (Wulf.) Nyl.	Lecanorales	Parmeliaceae	Foliose	*Olea europea*

The Station 3 is split into two sub-stations (1 and 2) located side by side: Christian Cemetery and Edough Square (North). In this station, foliose lichens dominate (74%) followed by crustose lichens (21%) and finally leprose lichens (5%). The 12 species recorded in this station are quite diverse, divided into four orders: Teloschistales, Lecanorales, Candelariales and Peltigerales; and six families: Teloschistaceae, Physciaceae, Lecanoraceae, Candelariaceae, Cladoniaceae and Collemataceae.

ISSN: 1737-933425

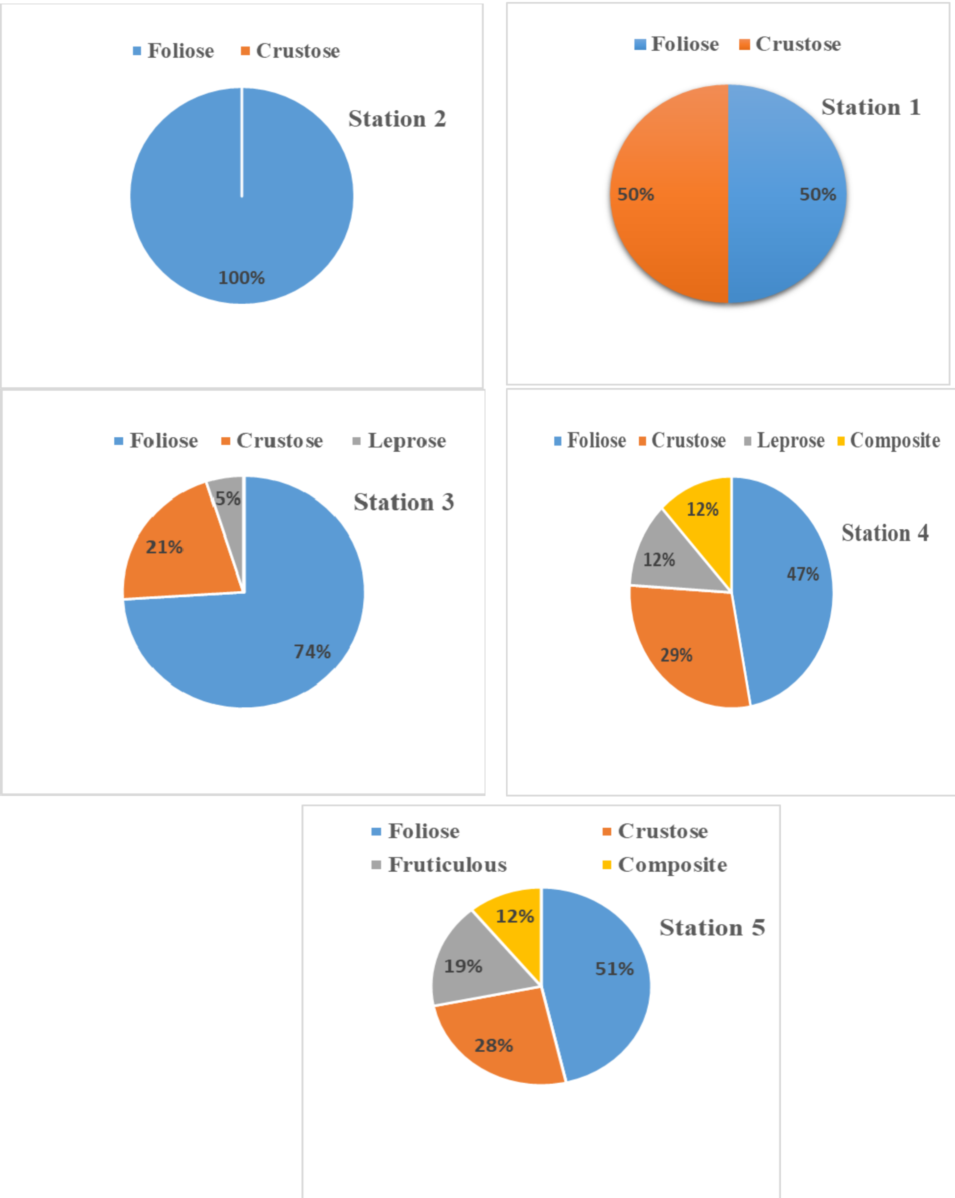

Fig. 3 Physiognomic spectra by thallus type of stations (station1, station 2, station 3, station 4)

TABLE 3

THE LICHENIC FLORA OF STATION 3 (SUB-STATIONS 1 AND 2)

n°	Name of species	Order	Family	Type of thallus	Substratum	Sub-station
1	*Candelariella reflexa* (Nyl.) Lettau	Candelariales	Candelariaceae	Crustose	*Cercis siliquastrum*	2
2	*Cladonia chlorophaea* (Flörke ex Sommerf.) Spreng.	Lecanorales	Cladoniaceae	Composite	*Cupressus sempervirens* and *Cercis siliquastrum*	1 and 2
3	*Collema nigrescens* (Huds.) DC	Peltigerales	Collemataceae	Foliose	*Cercis siliquastrum*	2
4	*Lecanora argentata* (Ach.) Malm.	Lecanorales	Lecanoraceae	Crustose	*Cercis siliquastrum*	2

ISSN: 1737-933426

5	*Lecanora chlarotera* Nyl.	Lecanorales	Lecanoraceae	Crustose	*Cercis siliquastrum*	2
6	*Lecanora conizaeoides* Nyl. ex Cromb.	Lecanorales	Lecanoraceae	Crustose	Cercis siliquastrum	2
7	*Lepraria incana* (L.) Ach	Lecanorales	Lecanoraceae	Crustose	Cercis siliquastrum	2
8	*Physcia adscendens* (Fr.) H. Olivier	Teloschistales	Physciaceae	Foliose	Cercis siliquastrum	2
9	*Physcia biziana* (A. Massal.) Zahlbr.	Teloschistales	Physciaceae	Foliose	*Cercis siliquastrum* and *Cercis siliquastrum*	1 and 2
10	*Physconia grisea* (Lam.) Poelt	Teloschistales	Physciaceae	Foliose	*Cupressus sempervirens* and *Cercis siliquastrum*	1 and 2
11	*Scytinium lichenoides* (L.) Otálora, P. M. Jørg. et Wedin.	Peltigerales	Collemataceae	Foliose	*Cupressus sempervirens*	1
12	*Xanthoria parietina* (L.) Th. Fr.	Teloschistales	Teloschistaceae	Foliose	*Cercis siliquastrum*	2

In general, the types of thallus represented in the station number 4 are given by the following values: foliose thallus 47%, crustose thallus 29%, composite and leprose thallus each giving a value of 12%.

TABLE 4

THE LICHENIC FLORA OF STATION 4

n°	Name of species	Order	Family	Type of thallus	Substratum
1	*Amandina punctata* (Ach.) Fryday et L. Arcadia	Caliciales	Caliciaceae	Crustose	*Fraxinus excelsior*
2	*Candelariella reflexa* (Nyl.) Lettau	Candelariales	Candelariaceae	Crustose	*Fraxinus excelsior*
3	*Collema furfuraceum* (Arnold) Du Rietz	Peltigerales	Collemataceae	Foliose	*Fraxinus excelsior*
4	*Collema subflaccidum* Degel.	Peltigerales	Collemataceae	Foliose	*Fraxinus excelsior*
5	*Collema subnigrescens* Degel. f.	Peltigerales	Collemataceae	Foliose	*Fraxinus excelsior*
6	*Collema nigrescens* (Huds.) DC	Peltigerales	Collemataceae	Foliose	*Fraxinus excelsior*
7	*Hypogymnia physodes* (L.) Nyl.	Lecanorales	Parmeliaceae	Foliose	*Fraxinus excelsior*
8	*Physcia adscendens* (Fr.) H. Olivier	Teloschistales	Physciaceae	Foliose	*Fraxinus excelsior*
9	*Physcia biziana* (A. Massal.) Zahlbr.	Teloschistales	Physciaceae	Foliose	*Fraxinus excelsior*
10	*Physcia leptalea* (Ach.) DC.	Caliciales	Physciaceae	Foliose	*Fraxinus excelsior*
11	*Physcia stellaris* (L.) Nyl.	Caliciales	Physciaceae	Foliose	*Fraxinus excelsior*
12	*Physconia grisea* (Lam.) Poelt	Caliciales	Physciaceae	Foliose	*Fraxinus excelsior*
13	*Physconia distorta* (With.) Laundon	Caliciales	Physciaceae	Foliose	*Fraxinus excelsior*
14	*Physconia venusta* (Ach.) Poelt	Caliciales	Physciaceae	Foliose	*Fraxinus excelsior*
15	*Lecanora chlarotera* Nyl.	Lecanorales	Lecanoraceae	Crustose	*Fraxinus excelsior*

ISSN: 1737-933427

16	*Lepraria incana* (L.) Ach	Lecanorales	Lecanoraceae	Crustose	*Fraxinus excelsior*
17	*Lecanora conizaeoides* Nyl. ex Cromb.	Lecanorales	Lecanoraceae	Crustose	*Fraxinus excelsior*
18	*Scytinium lichenoides* (L.) Otálora, P. M. Jørg. et Wedin.	Peltigerales	Collemataceae	Foliose	*Fraxinus excelsior*
19	*Xanthoria parietina* (L.) Th. Fr.	Teloschistales	Teloschistaceae	Foliose	*Fraxinus excelsior*

Regarding the last station (station 5), the corticolous populations of lichens of the foliose thallus type (*Flavoparmelia caperata*, *Parmotrema perlatum*, *Parmelia borreri*), and especially fruticulose ones (the abondant *Ramalina farinacea* or *Ramalina fastigiata*, *Evernia prunastri*, and *Teloschistes Chrisophtalmus*), seem to be the best indicators of good air quality in this station. We note the presence of *Usnea ceratina*, which seems to grow well on *Erica arborea* (better than on *Quercus suber* on which it was also found), since a few pendulous specimens of about ten centimetres long were found. For the crustose thallus we find mainly: *Lepra amara*, *Pertusaria pertusa* and also *Diploicia canescens*, *Gyalolechia flavorubescens*, in addition to the abundance of *Lecanora chlarotera*, *Bacidia rubella* is present on almost the entire surface of the bark of trees.

The lichenic specimens found in the Edough station are grouped into six orders: Teloschistales, Lecanorales, Peltigerales, Verrucariales, Pertusariales, Ortospales, comprising twelve families: Physciaceae, Lecanoraceae, Ramalinaceae, Collemataceae, Cladoniaceae, Teloschistaceae, Parmeliaceae, Lobariaceae, Verrucariaceae, Pertusariaceae, Pannariaceae, Phlyctidaceae and 26 genera.

TABLE 5

THE LICHENIC FLORA OF STATION 5. (*) AND WRITING IN BOLD ARE A NEW RECORDS (UNDER PRESS) FOR THE STUDY AREA (EDOUGH PENINSULA)

n°	Name of species	Order	Family	Type of thallus	Substratum
1	**Amandina punctata* Hoffm.	Caliciales	Caliciaceae	Crustose	*Quercus suber*
2	*Anaptychia cilliaris* (L.) Körb. ex A. Massal.	Caliciales	Physciaceae	Fruticulose	*Quercus suber*
3	*Bacidia rubella* (Hoffm.) A. Massal	Lecanorales	Ramalinaceae	Crustose	*Quercus suber*
4	**Blastenia ferruginea* (Huds.) A. Massal.	Teloschistales	Teloschistaceae	Crustose	*Quercus suber*
5	**Collema furfuraceum* (Arnold) Du Rietz	Peltigerales	Collemataceae	Foliose	*Quercus suber*
6	*Collema nigrescens* (Huds.) DC	Peltigerales	Collemataceae	Foliose	*Quercus suber*
7	**Cladonia chlorophaea* (Flörke ex Sommerf.) Spreng	Lecanorales	Cladoniaceae	Composite	*Quercus suber*
8	*Evernia prunastri* (L.) Ach	Lecanorales	Parmeliaceae	Fruticulose	*Quercus suber*
9	*Flavoparmelia caperata* (L.) Hale	Lecanorales	Parmeliaceae	Foliose	*Quercus suber*
10	**Fuscopannaria leucosticta* (Tuck. ex E. Michener) P.M. Jørg	Peltigerales	Pannariacea	Foliose	*Quercus suber*
11	**Gyalolechia flavorubescens* (Huds.) Søchting, Frödén & Arup	Teloschistales	Teloschistaceae	Crustose	*Quercus suber*
12	**Lecanora chlarotera* Nyl	Lecanorales	Lecanoraceae	Crustose	*Quercus suber*
13	**Lecidella elaeochroma* (Ach.) M. Choisy	Lecanorales	Lecanoraceae	Crustose	*Quercus suber*
14	**Lepra albescens* (Huds.) Hafellner	Pertusariales	Pertusariaceae	Crustose	*Quercus suber*
15	*Lepra amara* (Ach.) Hafellner	Pertusariales	Pertusariaceae	Crustose	*Quercus suber*
16	*Lobaria amplissima* (Scop.) Forssell.	Peltigerales	Lobariaceae	Foliose	*Quercus suber*
17	*Lobaria pulmonaria* (L.) Hoffm.	Peltigerales	Lobariaceae	Foliose	*Quercus suber*

ISSN: 1737-933428

18	*Nephroma laevigatum* (Ach.) Ach.	Peltigerales	Peltigeraceae	Foliose	*Quercus suber*
19	**Normandina pulchella* (Borrer.) Nyl.	Verrucariales	Verrucariaceae	Squamulose	*Quercus suber*
20	**Ochrolechia androgyna* (Hoffm.) Arnold	Pertusariales	Ochrolechiaceae	Crustose	*Quercus suber*
21	*Parmelia sulcata* Taylor	Lecanorales	Parmeliaceae	Foliose	*Quercus suber*
22	*Parmelina pastillifera* (Harm.) Hale	Lecanorales	Parmeliaceae	Foliose	*Quercus suber*
23	**Parmotrema perlatum* (Huds.) M. Choisy	Lecanorales	Parmeliaceae	Foliose	*Quercus suber*
24	*Parmotrema reticulatum (*Taylor) M. Choisy	Lecanorales	Parmeliaceae	Foliose	*Quercus suber*
25	**Pectenia plumbea* (Lightf.)	Peltigerales	Pannariacea	Foliose	*Quercus suber*
26	**Pertusaria coccodes* (Ach.) Nyl	Pertusariales	Pertusariaceae	Crustose	*Quercus suber*
27	*Pertusaria pertusa* (Weigel) Tuck.	Pertusariales	Pertusariaceae	Crustose	*Quercus suber*
28	*Phaeophyscia orbicularis* (Neck.) Moberg	Caliciales	Physciaceae	Foliose	*Quercus suber*
29	*Physcia aipolia* (Ehrh. ex Humb.) Fürnr .	Caliciales	Physciaceae	Foliose	*Quercus suber*
30	*Physcia leptalea* (Ach.) DC.	Caliciales	Physciaceae	Foliose	*Quercus suber*
31	*Physconia distorta* (With.) Laundon	Caliciales	Physciaceae	Foliose	*Quercus suber*
32	*Physconia perisidiosa* (Erichsen) Moberg	Caliciales	Physciaceae	Foliose	*Quercus suber*
33	*Physconia venusta* (Ach.) Poelt.	Caliciales	Physciaceae	Foliose	*Quercus suber*
34	*Pleurostitca acetabulum* (Neck.) Elix & Lumbsch	Lecanorales	Parmeliaceae	Foliose	*Quercus suber*
35	*Punctelia subrudecta* (Nyl.) Krog	Lecanorales	Parmeliaceae	Foliose	*Quercus suber*
36	*Ramalina canariens* J. Steiner	Lecanorales	Ramalinaceae	Fruticulose	*Quercus suber*
37	*Ramalina farinacea* (L.) Ach	Lecanorales	Ramalinaceae	Fruticulose	*Quercus suber*
38	*Ramalina fastigiata* (Pers.) Ach	Lecanorales	Ramalinaceae	Fruticulose	*Quercus suber*
39	**Ramalina fraxinea* (L.) Ach.	Lecanorales	Ramalinaceae	Fruticulose	*Quercus suber*
40	**Ramalina pollinaria* (Westr.) Ach.	Lecanorales	Ramalinaceae	Fruticulose	*Quercus suber*
41	**Scytinium lichenoides* (L.) Otálora	Peltigerales	Collemataceae	Foliose	*Quercus suber*
42	**Teloschistes chrysophthalmos* (L.) Th.Fr	Teloschistales	Teloschistaceae	Fruticulose	*Quercus suber*
43	**Usnea ceratina* Ach.	Lecanorales	Parmeliaceae	Fruticulose	*Quercus suber*
44	*Xanthoria parietina* (L.) Th.Fr.	Teloschistales	Teloschistaceae	Foliose	*Quercus suber*

ISSN: 1737-933429

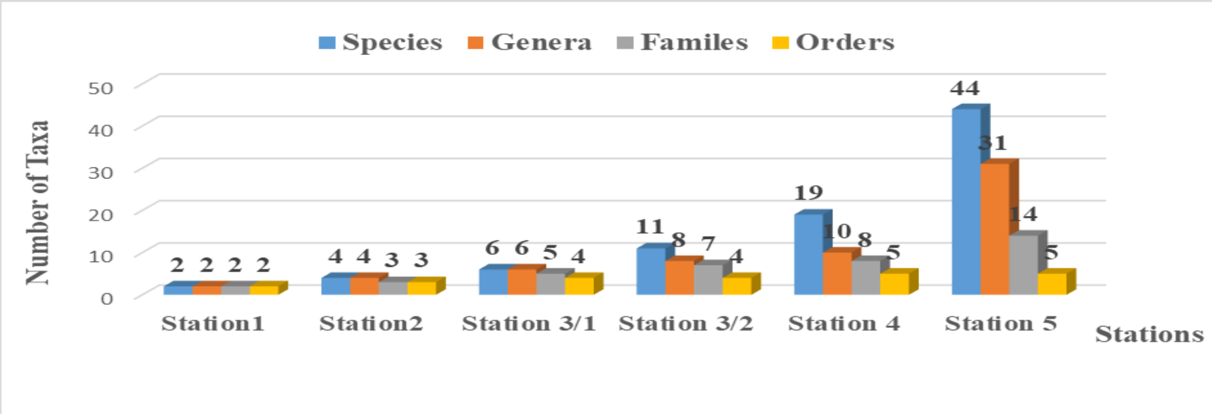

Fig. 4 Systematic spectra of the five surveyed stations

Air quality assessment using qualitative and quantitative methods

❖ Qualitative methods

- ***The scale for estimating air quality in northern France according to the Method of Van Haluwyn et Lerond (1986)*****[1]**

SO_2 is considered the main "tracer" of industrial and urban air pollution. Therefore, SO_2 pollution is the easiest to track and study.

The air quality assessment of our study area (station 1: Fertial (Algerian Fertiliser Company), station 2: Boukhadra (a municipality next to Fertial); station 3: Christian Cemetery (City centre of Annaba)and Square de l'Edough Nord (In front of the Christian Cemetery), station 4: Bouhdid Cemetery (at the foothills of the Edough mountain), station 5: which is the reference station, Edough Montain or Edough Peninsula) according to the method of Van Halwyun and Lerond [1] is given in Table 6. A variation in air quality was observed between the five stations studied:

Station 1 (Fertial) was considered to be a very heavily polluted station, which places it in class "B".

The 2nd station (Boukhadra) has been classified in zone "E" because its air pollution is estimated to be medium.

Station 3, subdivided into two juxtaposed substations (Christian Cemetery, Square de l'Edough "North"), is estimated as a station with moderately low pollution, placing it between two classes "E-F". The same observation was made for the Bouhdid station (station 4) even though the number of lichens recorded in the latter is higher (19 taxa) than that of station 3.

The reference station (Edough Peninsula) has low to very low pollution; placing this station between classes F and G.

TABLE 6

ESTIMATION OF THE AIR QUALITY OF THE STATIONS ACCORDING TO THE METHOD OF VAN HALUWYN AND LEROND [1]

Class	SO_2 Pollution	Station	Lichen species present according to the air quality assessment scale of Van Haluwyn and Lerond [1]
B	Very heavy pollution	1	*Pleurococccus virdis* ; *Leanora conzaeiodes*; *Xanthoria parietina*
E	Moderate pollution	2	*Physcia adscendens*; *Xanthoria parietina*
E-F	Moderately low pollution	3	*Physconia grisea, Lepraria incana* *Physconia grisea, Lepraria incana, Xanthoria parietina, Lecanora conizaeoides, Physcia adscendens*
E-F	Moderately low pollution	4	*Physcia adscendens*; *Xanthoria parietina*; *Physconia grisea*; *Lepraria incana*

ISSN: 1737-933430

F-G	Low to very low pollution	5	*Anaptychia cilliaris, Parmotrema perlatum*; *Ramalina farinacea, Ramalina fraxinea, Physcia aipolia, Flavoparmelia caperata, Ramalina fastigiata*

- **Dalby's Illustrated Scale [2]**

The results of the estimation of air quality in our five study stations, according to the scale of Dalby [2]are recorded in Table 7.

According to the lichen species identified in station 1 (Fertial), the rate of atmospheric pollution is estimated between 150 and 70 µg/m^3 of SO_2.

In the station 2 (Boukhadra), the rate of atmospheric pollution is estimated between 70 and 60 µg/m^3 de SO_2.

According to the resenced lichen specimens in the station 3, the rate of atmospheric pollution varied between 50 and 150 µg/m^3 de SO_2

In the fourth station (Bouhdid), the SO_2 level is estimated at more than 50 µg/m^3.

Thanks to the presence of lichen species sensitive to pollution according to the air quality estimation scale of Van haluwyn and Lerond (1986), such as: *Usnea ssp.*, *Lobaria ssp.* or *Pectenia plumbea* (previously known as), the estimated SO_2 level at reference station 5 (Edough Penninsula) is [30-35] to 5 µg/m^3.

TABLE 7

ESTIMATION OF STATION AIR QUALITY ACCORDING TO THE ILLUSTRATED SCALE OF DALBY [2]

SO_2 µg/m^3	Station	Lichen species present according to Dalby's Air Quality Assessment Scale [2]
150-70	1	*Pleurococccus virdis ; Leanora conzaeiodes; Xanthoria parietina*
70-60	2	*Physcia adscendens; Xanthoria parietina, Parmeliopsis ambigua,*
150- ≥50	3	*Physconia grisea, Physcia biziana*
		Physconia grisea, Xanthoria parietina, Lecanora chlarotera; Physcia adscendes
≥50	4	*Xanthoria parietina, Lecanora chlarotera; Physcia adscendes, Lepraria incana*
35-30 to 5	5	*Parmotrema perlatum, Lobaria pulmonaria, Ramalina fraxinea, Ramalina calicaris,Ramalina fastigiata ,Physcia aipolia, Degelia plumbea*

- **The scale adapted by Tiévant (2001) [3]**

According to the air quality assessment scale adapted by Tiévant [3], which classifies areas (ranging from 1 to 10) according to the estimated SO_2 level based on the presence of specific lichen species, we estimate the air quality of our 5 study stations as follows (Table 8):

- ✓ The 1st station (Fertial) corresponds to the 4th zone of the adapted Tiévant scale [3] with an estimated SO_2 value of about 70 µg/m^3.
- ✓ Depending on the lichen species growing in station 2 (Boukhadra), the SO_2 level is estimated to be between 50 µg/m^3 and 60 µg/m^3, which corresponds to zones 5 and 6 respectively, of the adapted scale of Tiévant [3]. The same estimate is noted for station 4 (Bouhdid Cemetery).
- ✓ Concerning station 3 (Christian Cemetery and Square de l'Edough Nord) and according to the lichenic species recorded, it corresponds to zone 4 with an estimate of SO_2 of approximately 70µg/m^3.
- ✓ The reference station 5 (Edough Peninsula) is classified in the 9th zone (on a scale of 10 zones) with a SO_2 value of about 30µg/m^3 according to the lichen species recorded.

ISSN: 1737-933431

TABLE 8

THE SCALE ADAPTED BY TIÉVANT (2001) [3]

zone	SO_2 µg/m^3	station	Lichen species present according to the scale adopted for estimating air quality by Tiévant [3]
4	70 approximately	1	*Pleurococccus virdis ; Leanora conzaeiodes; Xanthoria parietina*
5 and 6	(50-60)	2	*Physcia adscendens; Xanthoria parietina, Parmeliopsis ambigua, Physconia grisea*
4	70 approximately	3	*Physconia grisea, Physcia biziana, Lepraria incana*
			Lepraria incana, Xanthoria parietina, Lecanora chlarotera; Physcia adscendes
5 and 6	(50-60)	4	*Xanthoria parietina, Lepraria incana,Lecanora chlarotera, Physconia grisea,Physcia adscendens*
9	30 approximately	5	*Pertusaria albescens, Lobaria pulmonaria, Ramalina fraxinea, Ramalina calicaris,Ramalina fastigiata, Physcia aipolia, Anaptychia ciliaris; Physcia leptalea*

In general, the comparison of the three qualitative methods (Van Haluwyn and Lerond's method [1], Dalby's illustrated scale [2] and Tiévant's adapted method [3]) shows that:

- Station 1 (Fertial): is classified as a very heavily polluted area up to a SO_2 value of 150µg/m^3.
- Station 2 (Boukhadra): is considered as a medium pollution zone around SO_2 of 60µg/m^3.
- Station 3 (Christian Cemetery and Square de l'Edough Nord) as well as station 4 (Bouhdid Cemetery): is considered as a "medium" low pollution area around an SO_2 value of 70-50µg/m^3.
- Station 5 (Edough Park): this station is classified as a low to very low pollution zone with the presence of *Anaptychia cilliaris*, *Permotrema perlatum*, *Physcia aipolia*, *Ramalina fraxinae*, *Lobaria pulmonaria*, *Ramalina calicaris*, which according to Dalby's scale [2] grows in zones below 5µg/m^3 as well as the presence of *Usnea ceratina* and *Pectenia plumbea*, which testify to the good air quality of the Edough mountain.

❖ Quantitative methods

In order to estimate the air quality in the studied stations, two quantitative methods were used: the first one is based on the calculation of the *index of atmospheric purity* (I.A.P.) of each station which aims to evaluate the air quality according to a scale, the second method consists in calculating the index of Lichenic Diversity per Station (LDS).

- ***The method of I.A.P. (index of atmospheric purity) of Leblanc et De Sloover*** **[4]**

The results of the atmospheric purity index (A.P.I.) obtained respectively for each station and which are recorded in table 9 (Tab. 9), show in a global way, the air quality of each of them (Fig. 5).

According to the scale established by reference [25] or [26], it appears that :

- Station 1 (Fertial) and station 2 (Boukhadra) have a low I.A.P. which translates into a very high atmospheric pollution (7.4 and 8.6 between [0-15]), hence a limited presence of the number of lichen species.
- On the other hand, station 3 (sub-station 1: Square de l'Edough Nord, sub-station 2: Christian Cemetery) is subject to a moderately polluted atmosphere due to their moderately

ISSN: 1737-933432

high I.A.P. values (27.7 and 34.7, i.e. an average of : 31.2, thus an I.A.P. between [30-45] classifying this station in a medium air pollution area (Tab.20).

- As for station 4, its I.A.P. value is quite high at 85.9 (≥ 60 according to the scale) which shows that the pollution is very low translating the good air quality of this station.
- Similarly for station 5 (Edough National Park) whose I.A.P. is ≥ 100, which translates into an important number of lichenic specimens compared to the other stations studied but also by the presence of lichens typically indicative of good air quality.

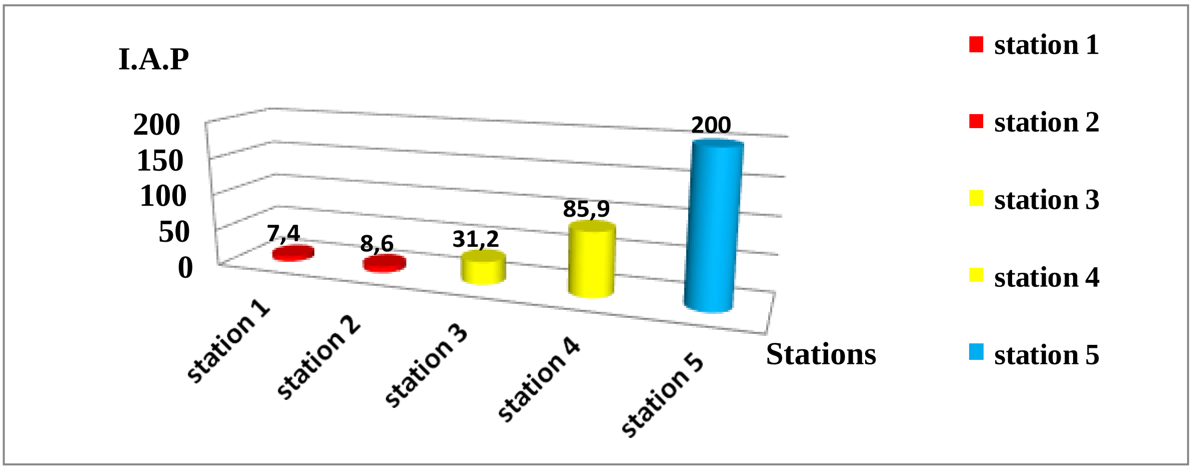

Fig. 5 Results of the air quality assessment using the quantitative method (Index of Air Purity I.A.P.)

TABLE 9

SCALE OF CORRESPONDENCE BETWEEN THE I.A.P. AND AIR POLLUTION

Atmospheric pollution	I.A.P. (Index of the air purity)	Station
Extremely high	0-15	S1 and S2
Medium	30-45	S3
Very low	≥ 60	S3 and S4

- ***The method for calculating lichen diversity per station (LDS)***

The indices of lichenic diversity per station, are recorded in the figure 6 and compared between them. Although the number of species seems to differ from one station to another, the index of lichenic diversity of certain stations (S1: Fertial, S2: Boukhadra) is identical, but remains much lower than that of the reference station, in this case the Edough station (S5): more than 13 times lower. This leads us to say that the stations of Fertial and Boukhadra (S1 and S2) are the most polluted and the poorest in terms of lichen diversity, followed by station S3 and S4 which are respectively 6 and 3 times less diverse in lichens than station 5 (Edough).

ISSN: 1737-933433

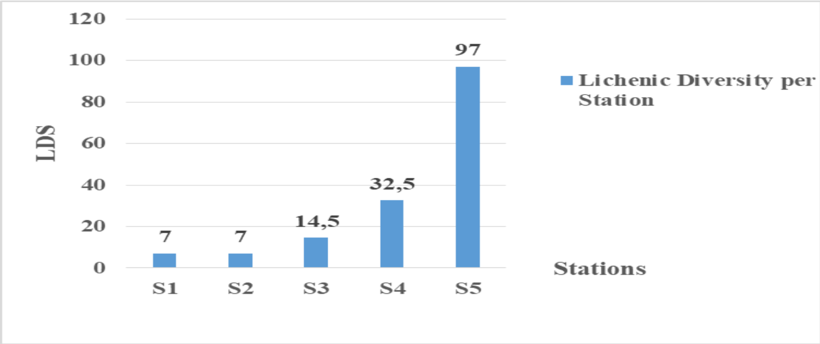

Fig. 6 Results of the air quality assessment using the quantitative method The index of Lichenic Diversity per Station (LDS)

As reported by the reference [27], the better the air quality of the environment, the more species will be able to thrive and the higher the lichenic diversity per station; and conversely, the more limiting the environmental conditions, the fewer species will be able to survive and the lower the lichenic diversity.

V. CONCLUSION

It appears from the use of lichens as an indicator of abiotic stress, in this case air pollution, in the stations studied (station1 Fertial; station2 Boukhadra, station3 Edough North Square and Christian Cemetery, station4 Bouhdid Cemetery and station5 Edough Peninsula):

Significant reduction in the number of species in station 1 (Fertial) which is considered to be polluted (source of fluorinated and plumbed air pollution) and where the SO_2 level is estimated at 150 µg/m^3.

Stations 2 and 3 are intermediate (average pollution) between stations 1 and 4, as they are more exposed to north-east winds, especially as station 3 is only separated from Fertial (Algerian Fertiliser Company) by the Mediterranean Sea

The Bouhdid cemetery station is considered to be a moderately polluted place located between the reference station (Edough) and the most polluted station, namely station 1 (Fertial)

The abundance of fruticulous and foliaceous lichens in station 5 (Edough) gives an idea about the good air quality of the station and especially the presence of some specimens:

Usnea ceratina, *Teloschistes chrysophtalmus*, *Lobaria pulmonaria Pectenia plumbea* (a new species in the study area) and *Fuscopannania leucosticta* (a species rediscovered in Algeria), which are particularly sensitive to pollution.

REFERENCES

[1] C. Van Haluwyn et M. Lerond, "Les lichens et la qualité de l'air. Evaluation méthodologique et lmites". Rapport final au Ministère de l'Environnement (SRETIE), 1986.
[2] C. Dalby, "LICHENS AND AIR POLLUTION", British Museum (Natural History), BP Educational Service, London, England, 1981.
[3] P. Tiévant, "Guide des Lichens, 350 espèces de lichens d'Europe". Paris, France, Edition Delachaux et Niestlé, 2001.
[4] F. LeBlanc and J. De Sloover, "Relation between industrialization and the distribution and growth of epiphytic lichens and mosses in Montreal". Canadian Journal of Botany, vol.48, pp. 1485–1496, 1970.
[5] G. Gooet et J. Ferguson, "Nature et science", Paris, France: Edition. Casteilla, 1987.
[6] J.P. Gavériaux, "Les lichens et la bio-indication de la qualité de l'air Guide technique à l'usage des professeurs des Collèges et des Lycées". *Bull. Soc. Bot. N. Fr.*, vol. 49, pp. 1–52, 1996.
[7] A-M. Fiore-Donno, "Les lichens épiphytes comme bioindicateurs de la pollution atmosphérique dans la région genevoise = Epiphytic lichens as bioindicators of atmospheric pollution in Geneva (Switzerland)". Saussurea, vol 28, pp.189–218, 1997.
[8] T.H.Nash III and C. Gries, "The response of lichens to atmospheric deposition with an emphasis on the Arctic". Science of The Total Environment, vol. 160–161, pp 737–747, 1995.
[9] C. Van Haluwyn et M. Lerond, "Guide des lichens", France, Edition Lechevalier, 1993.
[10] N. Maizi, A. Alouia et A. Tahar, "Jumelage des bio-indicateurs et d'un réseau de surveillance de la qualité de l'air pour la détection de la pollution par le SO2 dans la région de Annaba (Algérie)", Biotechnol. Agron.

ISSN: 1737-933434

Soc. Environ., vol. 16, pp.149–158, 2012.
[11] A. Semadi, "Effet de la pollution atmosphérique (pollution globale, fluorée et plombique) sur la végétation dans la région de Annaba". Thèse de Doctorat d'état en sciences naturelles. Université Pierre et Marie Curie, Paris VI, France, 1989.
[12] A. Alioua "Détection de la pollution mercurielle dans la région de Azzaba à l'aide de bio-accumulateurs (*Xanthoria parietina*, *Olea europea*, *Cupressus sempervirens*, *Casuarina equisetifolia* et *Triticum durum*) ". Thèse de Magister, Université d'Annaba, Algérie, 1995.
[13] A. Alioua "Détection de la pollution plombique d'origine automobile à l'aide de bio-accumulateurs végétaux dans l'agglomération de Skikda (N. E. Algérie) ", Thèse de Doctorat, Université Joseph Fourier, Grenoble, France, 2001.
[14] A. Alioua, N. Maizi, A. Semadi, A. Tahar et M. Kahoul "Détection et Etude de la Pollution Mercurielle à l'Aide des Bioindicateurs Dans la Région de Azzaba (Algérie Orientale)", *European Journal of Scientific Reasearch*,vol. 23, pp.187–196, Nov. 2008.
[15] H. Poličnik, P. Simoncic and F. Batic, "Monitoring air quality with lichens : a comparison between mapping in forest and in open areas", Environmental pollution, vol. 151, pp. 395– 400, 2008.
[16] C. Van Haluwyn, J. Asta, J.P. Gavériaux, "Guide des Lichens de France, Lichens des arbres". Paris, France Edition Belin, 2013.
[17] A.J. Silverside (2013) "Images of British Lichens". [Online]. Available: lastdragon.org
[18] (2023) The AFL website. [Online]. Available: http:// www.afl-lichenologie.fr
[19] (2023) The irishlichens website. [Online]. Available: http:// www.irishlichens.ie
[20] C. Roux et coll., "Catalogue des lichens et champignons lichénicoles de France métropolitaine". 2e édition revue et augmentée. Association française de lichénologie (A.F.L.). Fontainebleau, France, 2017.
[21] C. Boucheron et N. Martin, "Estimation de la qualité de l'air par l'étude des lichens épiphytes bio-indicateurs sur le Pays du Bocage Vendéen". CPIE Sèvre et Bocage, 2019.
[22] (2023) The SIGLES website. [Online]. Available: http://www.sigles-sante-environnement.fr/?page_id=14303
[23] A. Chaker, K. Fekroune, A. Hassaine, A. slimani, L. Zerari and R. Moulaï, "New data on lichen flora of the Edough Peninsula in north-eastern Algeria", Botanica, vol. 29, pp. 9–20, 2023.
[24] J.C. Masson. (2014) Les lichens, bio-indicateurs de la qualité de l'air. IFE, [Online]. Available: http://www.attiredailes.be/pdf/botanique/bota_lichens_bio-indicateurs.pdf
[25] R.H. Herzig, J.D. Hines, G.P. Herzig, S.N. Wolff, P.A. Cassileth, H.M. Lazarus, D.J. Adelstein, R.A. Brown, P.F. Coccia and S. Strandjord, "Cerebellar toxicity with high-dose cytosine arabinoside". J Clin Oncol. Vol. 5, pp.927–32, 1987.
[26] R. Kricke and S. Loppi, "Bioindication: the I.A.P. approach". In: P.L. Nimis, C. Scheidegger, P.A. Wolseley, Ed. "Monitoring with lichens". Monitoring lichens, Kluwer Academic Publishers, NATO Science Series, pp. 21–37, 2002.
[27] C. Boucheron et N. Martin, Estimation de la qualité de l'air par l'étude des lichens épiphytes bio-indicateurs sur le Pays du Bocage Vendéen. France: CPIE Sèvre et Bocage, 2019.

ISSN: 1737-933435

Characterisation of a Carreau-Yassuda Fluid Flow Within a Circular Pipe

Labsi Nabila[1], Melki Rafik[2], Benkahla Youb Khaled[3]

Equipe Rhéologie et Simulation Numérique des Ecoulements, Laboratoire des Phénomènes de Transfert,
Faculté de Génie Mécanique et de Génie des Procédés,
Université des Sciences et de la Technologie Houari Boumediene
BP. 32 El Allia, Bab Ezzouar, Alger, Algérie
[1]nabilalabsi@yahoo.fr ; nlabsi@usthb.dz
[2]melki.rafik@hotmail.com
[3]youbenkahla@yahoo.fr

***Abstract*— The study considers the laminar steady axisymmetric flow of an incompressible Carreau fluid in a circular pipe, maintained at a constant and uniform wall temperature. The dimensionless governing equations, i.e. continuity, momentum and energy equations, are discretized using the Finite Volume Method and resolved by means of a homemade computer code. The study focuses on the effect, on heat transfer, of both viscous dissipation and temperature-dependency of the fluid's viscosity. The results show that neglecting viscous dissipation for both isoviscous and thermodependent fluid leads to underestimate heat transfer.**

***Keywords*— Carreau fluid, thermodependent viscosity, viscous dissipation, finite volume method, circular pipe.**

I. Introduction

Some fluids such as polymers are well described by the rheological model of Carreau-Yasuda. Thus, many studies have been undertaken considering the flow of this non Newtonian fluid within various geometries.

Khellaf and Lauriat [1] studied the forced, mixed and natural convection of a Carreau fluid within a short annulus with a heated and rotating inner cylinder and a cooled and fixed outer cylinder. Their results show that the shear thinning effect decreases the friction factor at the rotating cylinder and increases the heat transfer through the annular.

Abbasi et *al.* [2] undertook a numerical study on the effect of applied magnetic field on the peristaltic transport of a Carreau-Yasuda fluid in a curved duct. They found that the fluid velocity is not symmetric about the centreline for small values of curvature parameter and that the increase of the Hall parameter value balances the magnetic effect of applied magnetic field.

Rousset et *al.* [3] analyzed the temporal stability of a Carreau fluid flow along a tilted plate plane. They highlighted the effect of shear-thinning fluid's properties on the definition of the stability kind. They found also that the critical Reynolds number for this fluid is smaller than the one corresponding to Newtonian fluids.

Lounis et *al.* [4] studied numerically, the thermosolutal convection of a Carreau-Yasuda fluid within an inclined square cavity by considering Soret and Dufour effects. The active walls are subject to constant and uniform concentrations and temperatures whereas the other walls are impermeable and adiabatic. The results show that the increase of the time constant parameter as well as the decrease of the ratio of infinite-to zero-shear-rate viscosities enhance thermal and mass exchange for various values of the flow index. In addition, the rise of the orientation angel from 0° to 90° increases heat and mass transfer rates.

Bilal et *al.* [5] analyzed the magnetic dipole and heat transmission through ternary hybrid Al_2O_3/SiO_2/TiO_2-Carreau-Yasuda nanofluid flow across a vertical stretching sheet. The heat transfer and velocity were analysed by considering the effect of heat source/sink and Darcy Forchhemier. Among the results, they found that the increase of the flow index increases the skin friction and the Nusselt number. Also, the rising effect of Darcy Forchheimer's term and porosity constant decreases the velocity outlines and finally, the ternary hybrid nanofluid have a greater tendency to increase the energy transmission across a vertical plate in comparison to the base fluid.

It can be seen that there is few studies regarding the Carreau-Yasuda or Carreau fluid flow within a pipe and moreover, by considering the effect of viscous dissipation. For this purpose, the present numerical study deals with

ISSN: 1737-933436

the analysis of thermal exchange through the flow of a temperature-dependent Carreau fluid within a pipe, by considering viscous dissipation.

II. Mathematical Formulation and Numerical Modelling

Let's consider the laminar steady axisymmetric flow of an incompressible Carreau fluid in a pipe of a circular cross section. The pipe is of length L and radius r_w and is maintained at a constant and uniform wall temperature T_w. The fluid is assumed to be of constant physical and rheological properties except for the apparent viscosity which is considered thermodependent. Viscous dissipation will be considered, by taking both cases of wall heating and wall cooling.

A. *Mathematical Formulation*

The dimensionless governing equations, i.e. continuity, momentum and energy equations are, respectively, given in cylindrical coordinates by:

$$\frac{1}{R}\frac{\partial(RV)}{\partial R}+\frac{\partial U}{\partial X}=0 \tag{1}$$

$$\frac{1}{R}\frac{\partial(RVV)}{\partial R}+\frac{\partial(UV)}{\partial X}=-\frac{\partial P^*}{\partial R}+\frac{1}{Re}\left[\frac{1}{R}\frac{\partial}{\partial R}\left(\eta_{app}R\frac{\partial V}{\partial R}\right)+\frac{\partial}{\partial X}\left(\eta_{app}\frac{\partial V}{\partial X}\right)\right]$$
$$+\frac{1}{Re}\left[\frac{V}{R}\frac{\partial}{\partial R}\left(\eta_{app}\right)-\eta_{eff}\frac{V}{R^2}+\frac{\partial}{\partial X}\left(\eta_{app}\right)\frac{\partial U}{\partial R}+R\frac{\partial}{\partial R}\left(\eta_{app}\right)\frac{\partial}{\partial R}\left(\frac{V}{R}\right)\right] \tag{2}$$

$$\frac{1}{R}\frac{\partial(RVU)}{\partial R}+\frac{\partial(UU)}{\partial X}=-\frac{\partial P^*}{\partial X}+\frac{1}{Re}\left[\frac{1}{R}\frac{\partial}{\partial R}\left(\eta_{app}R\frac{\partial U}{\partial R}\right)+\frac{\partial}{\partial X}\left(\eta_{app}\frac{\partial U}{\partial X}\right)\right]$$
$$+\frac{1}{Re}\left[\frac{\partial}{\partial R}\left(\eta_{app}\right)\frac{\partial V}{\partial X}+\frac{\partial}{\partial X}\left(\eta_{app}\right)\frac{\partial U}{\partial X}\right] \tag{3}$$

$$\frac{1}{R}\frac{\partial(RV\theta)}{\partial R}+\frac{\partial(U\theta)}{\partial X}=\frac{1}{Pr\,Re}\left[\frac{1}{R}\frac{\partial}{\partial R}\left(R\frac{\partial\theta}{\partial R}\right)+\frac{\partial^2\theta}{\partial X^2}\right]+\frac{Br}{Pr\,Re}\eta_{app}\gamma^{*2} \tag{4}$$

Where the dimensionless second invariant in Equation (4) is given by:

$$\gamma^{*2}=2\left\{\left(\frac{\partial V}{\partial R}\right)^2+\left(\frac{\partial U}{\partial X}\right)^2+\left(\frac{V}{R}\right)^2\right\}+\left(\frac{\partial U}{\partial R}+\frac{\partial V}{\partial X}\right)^2 \tag{5}$$

The apparent viscosity of Carreau fluid is given, in its dimensionless form by the following law, proposed by Bird at al. [6]:

$$\eta_{app}=\left[\left(1+We^2\gamma^{*2}\right)^{\frac{n-1}{2}}\right] \tag{6}$$

Where We represents the Weissenberg number and n is the flow index.

To complete the system of governing equations, we consider as steady boundary conditions, a uniform axial velocity and temperature at the inlet (U = θ = 1, V = 0), no-slip conditions are applied at the wall along the pipe where a uniform wall temperature is assumed (U = V = θ = 0) and finally, at the symmetry plan (θ = 0), we consider: $\left(\frac{\partial U}{\partial X}=\frac{\partial V}{\partial X}=\frac{\partial\theta}{\partial X}=0\right)$.

B. *Numerical Modelling and validation of the computer code*

The governing equations with the corresponding boundary conditions are solved numerically using the finite volume method proposed by Patankar [7]. Thus, these differential equations are transformed in algebraic equations which are solved by means of the line by line method.

ISSN: 1737-933438

The grid adopted in the present study is non-uniform and consists, after studying the sensitivity of the results to the mesh, of 250 nodes in the X direction and 50 nodes in the R direction. The convergence criterion, which is based on the residual, is set to 10^{-5} for both velocity components and temperature and to 10^{-6} for pressure.

Since there is few works regarding the Carreau fluid's flow within a pipe, to validate our computer code, we considered the limit case of a Newtonian fluid (n = 1). Thus, our results, concerning the axial evolution of the Nusselt number, were compared to those of Min et *al.* [8]. The comparison, illustrated in Fig. 1, shows a good agreement between both results since the relative gap does not exceed 1.8%.

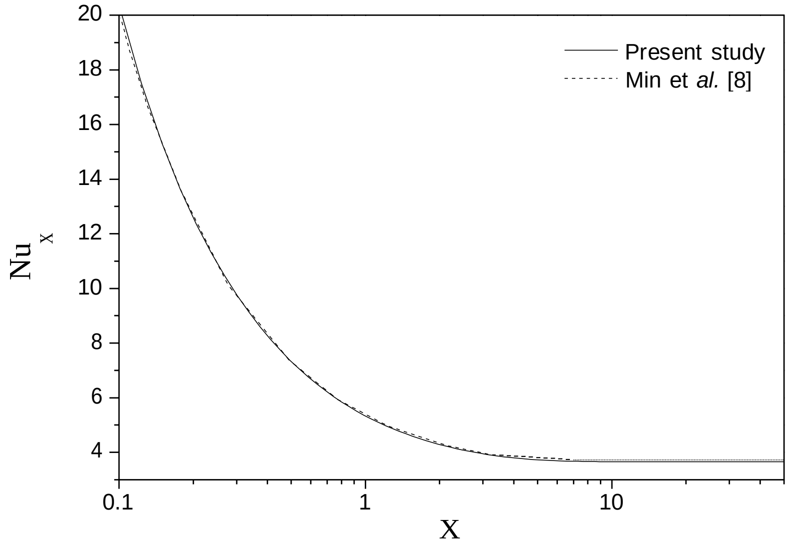

Fig. 1 Axial evolution of the local Nusselt number. Re = 50, Pr = 1, n = 1.

III. RESULTS AND DISCUSSION

The present study focuses on the analysis of the effect of neglecting viscous dissipation when the Carreau fluid is considered isoviscous and thermodependent.

Viscous dissipation is an energy source, represented by the Brinkman number (Br). Taking this function into account in the energy equation, leads to significant modifications on heat transfer behaviour, especially for viscous Newtonian and non Newtonian fluids.

A. Case of a Isoviscous Fluid

Fig. 2 represents the effect of the Brinkman number on the axial evolution of the Nusselt number, by considering both cases of wall heating (Br < 0) and wall cooling (Br > 0).

The figure shows a pronounced decrease of the Nusselt number from the inlet until reaching an asymptotic value which corresponds to the fully developed flow. For both heating and cooling, this value is single and is equal to 11.07, which is greater than the one obtained when viscous dissipation is neglected (Br = 0), i.e. 3.79.

Heat transfer is improved by the increase of the Brinkman number. Thus, neglecting viscous dissipation leads to undervalue heat transfer about 192% comparing to the case where viscous dissipation is neglected.

Note that in the case of wall heating (Br < 0), the curves present a discontinuity, with the existence of negative values of the Nusselt number due to the change in heat direction.

ISSN: 1737-933439

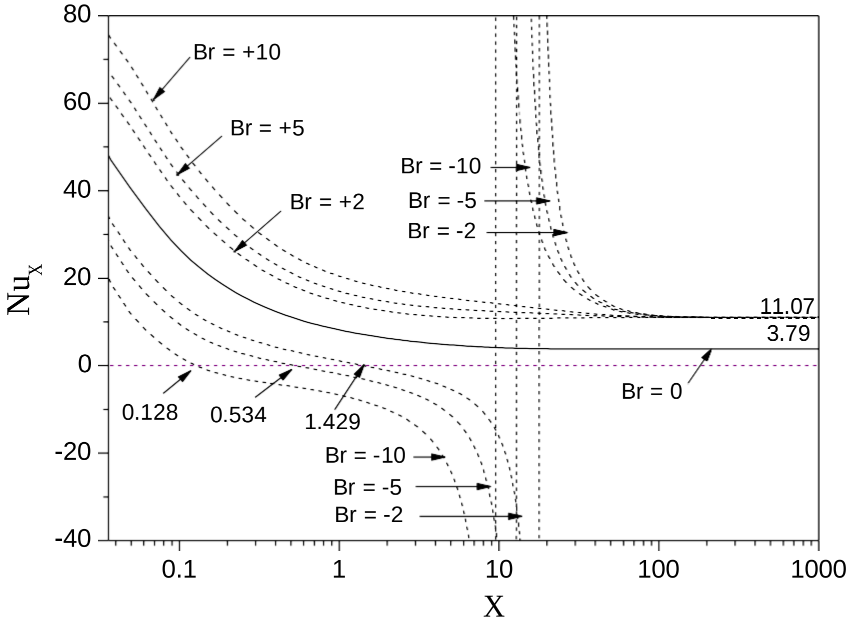

Fig. 2 Axial evolution of the local Nusselt number for various values of the Brinkman number. Re = 40, Pr = 10, n = 0.7, We = 20.

B. Case of a Thermodependent Fluid

The curves of Fig. 3 which represent the axial evolution of the Nusselt number when the fluid's apparent viscosity is thermodependent, show a decrease of the Nusselt number to reach different asymptotic values according to heating (Br < 0 ; a* > 0) or cooling (Br > 0 ; a* < 0) cases. Indeed, contrary to the case of a constant viscosity, an asymptotic value of the Nusselt number is obtained for each value of the Brinkman number as the fluid is temperature-dependent.

It is interesting to note also that in the developing region, the increase of the Brinkman number enhances heat transfer in the cooling case and worsens it in the heating case. However, in the fully developed region, heat transfer is improved when the Brinkman number decreases in absolute value, for both heating and cooling cases.

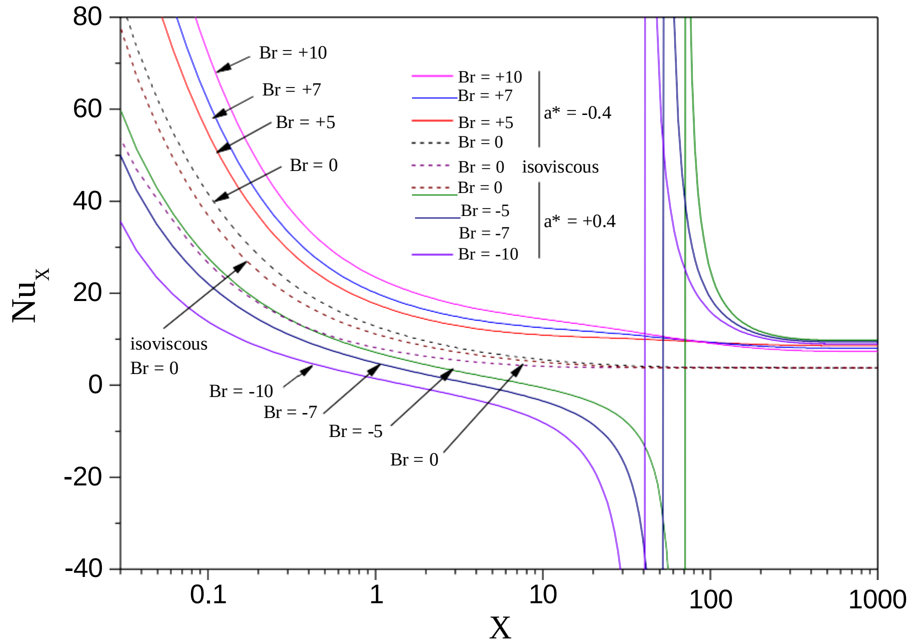

Fig. 3 Axial evolution of a temperature-dependent Carreau-Yasuda fluid's Nusselt number via the Brinkman number. n = 0.7, Re = 40, Pr = 10, We = 20.

IV. Conclusions

A numerical study based on the finite volume method was undertaken for a steady laminar forced convection flow of a Carreau fluid within a circular pipe maintained at a uniform wall temperature.

The study focused on the effect of viscous dissipation on heat transfer rate in the pipe, by considering an isoviscous fluid and a thermodependent one. The results show that heat transfer is strongly affected by viscous dissipation for both cases.

Thus, it is not rigorous to neglect viscous dissipation in calculation especially, when dealing with viscous fluids such as those obeying the rheological model of Carreau.

References

[1] K. Khellaf, G. Lauriat, "Numerical study of heat transfer in a non-Newtonian Carreau-fluid between rotating concentric vertical cylinders," *J. Non-Newtonian Fluid Mech.*, vol. 89, pp. 45-61, 2000.

[2] F.M. Abbasi, T. Hayat, A. Alsaedi, "Numerical analysis for MHD peristaltic transport of Carreau–Yasuda fluid in a curved channel with hall effects," *J. Magnetism and Magnetic Materials*, vol. 382, pp. 104-110, 2015.

[3] F. Rousset, S. Millet, V. Botton, H. Ben Hadid, "Temporal stability of Carreau fluid flow down an incline," *J. Fluids Eng.*, vol. 129, pp. 913-920, 2007.

[4] S. Lounis, R. Rebhi, N. Hadidi, G. Lorenzini, Y. Menni, H. Ameur, N.A. Che Sidik, "Thermo-Solutal Convection of Carreau-Yasuda Non-Newtonian Fluids in Inclined Square Cavities Under Dufour and Soret Impacts," *CFD Letters*, vol. 14 (3), pp. 96-118 (2022).

[5] M. Bilal, I. Ullah, M.M. Alam, S.I. Shah, S.M. Eldin, "Energy transfer in Carreau Yasuda liquid influenced by engine oil with Magnetic dipole using tri-hybrid nanoparticles," *Scientific Reports*, vol. 13, Article number 5432, 2023.

[6] R.B. Bird, R.C. Armstrong, O. Hassager, *Dynamics of Polymeric Liquids*, Vol. 1 Fluid Mechanics, 2nd edtion, Wiley and sons, New York, 1978.

[7] S.V. Patankar, *Numerical heat transfer and fluid flow,* Hemisphere, New York, 1980.

[8] T. Min, H.G. Choi, J.Y. Yoo, H. Choi, "Laminar convective heat transfer of a Bingham plastic in a circular pipe-II. Numerical approach-hydrodynamically developing flow and simultaneously developing flow," *Int. J. Heat Mass Trans*, vol. 40, pp. 3689-3701, 1997.

Nomenclature

Br Brinkman number, $=\eta_0 V_0^2 / k(T_0 - T_w)$
C_p specific heat at constant pressure, $J.kg^{-1}.K^{-1}$
D pipe diameter, m
k fluid thermal conductivity, $W.m^{-2}.K^{-1}$
L pipe length, m
n flow index
Nu Nusselt number, $= -\frac{1}{\theta_m}\frac{\partial\theta}{\partial R}\Big|_{R=0.5}$
Pr Prandtl number, $=\eta_{à} C_p V_0 / k\, D$
P^* dimensionless pressure, $= p^* / \rho V_0^2$
p^* pressure, Pa
r radial coordinate, m
R dimensionless radial coordinate, $= r / D$
Re Reynolds number, $=\rho V_0 D / \eta_0$
T temperature, K
T_m dimensional bulk temperature, K
T_0 inlet and reference temperature, K
T_w wall temperature, K
U dimensionless x-component velocity, $= V_x / V_0$
V dimensionless r-component velocity, $= V_r / V_0$
V_x x-component velocity, $m.s^{-1}$
V_r r-component velocity, $m.s^{-1}$
V_0 inlet velocity, $m.s^{-1}$
We Weissenberg number, $=\lambda D / V_0$
x axial coordinate, m
X dimensionless axial coordinate, $= x / D$

Greek symbols:
ρ density of the fluid, $kg.m^{-3}$
γ shear rate, s^{-1}
γ^* dimensionless shear rate, $=\gamma D / V_0$
η effective viscosity, $Pa.s^n$
η_{app} dimensionless effective viscosity, $=\eta / K_0$
η_0 viscosity at zero shear, Pa.s
λ the relaxation time, s
θ dimensionless temperature, $= (T - T_w) / (T_0 - T_w)$
θ_m dimensionless mean temperature, $= (T_m - T_w)/(T_0 - T_w)$

ISSN: 1737-933441

Numerical investigation of double diffusive mixed convection in vertical channel with a porous medium

Karima SELLAMI[#1], M'barek FEDDAOUI[2], Monssif NAJIM[2], Nabila LABSI[1], and Youb Khaled BENKAHLA[1]

[#1]*Laboratoire de phénomènes de transfert, RSNE, Faculté de Génie Mécanique et de Génie des Procédés, USTHB, Alger, Algérie*

[2]*Laboratoire Génie de l'Energie, Matériaux et Systèmes, ENSA Agadir, Maroc*

Email 1 - sellami_karima@yahoo.fr

Abstract:

The present paper concerns a new mathematical approach to analyse the influence of the effective parameters on the performance of direct evaporation from a porous layer. The ambient air flows over a porous material, fed with water. The evaporation of an amount of water into the air reduces its temperature and, at the same time, raises the air's humidity. A mathematical model that accounts for simultaneous heat and mass transfer characteristics in the ambient air and water flow in corporating non-Darcian model in the porous region within vertical parallel walls is presented. The solution of the mathematical model is based on the finite volume method and the velocity-pressure coupling is treated with the SIMPLE algorithm. The results showed that the porous evaporative cooler could meet the cooling requirements in arid climates. An average drop of 15 °C of air temperature below the ambient temperature can be reached at the considered conditions. Therefore, the ambient air is satisfactorily cooled. Furthermore, the better cooling performance can be achieved for a high porosity with a thick porous medium and lower air velocity at the entrance.

Key words: evaporative cooling, non-Darcian Model, porous ceramic, vertical walls, mixed convection.

Nomenclature

A	area, m^2
C	inertia parameter.
Cp	specific heat of the fluid at constant pressure, ($J.kg^{-1}.K^{-1}$)
d	porous layer thickness, (m)
D_h	hydraulic diameter, (m)
D	mass diffusivity, ($m^2.s^{-1}$)
g	gravitational acceleration, ($m.s^{-2}$)
H	channel width, (m)
h_{fg}	latent heat of vaporization, ($J.kg^{-1}$)
K	permeability of the porous layer, (m^2)
k	thermal conductivity, ($W.m^{-1}.K^{-1}$)
L	channel length, (m).
m_L	liquid mass flow rate, ($kg.m^{-1}.s^{-1}$)
$\dot{m}_I$	evaporative mass flux, ($kg.m^{-2}.s^{-1}$)
Mr	evaporation rate of mixture
P	pressure, (Pa)
Q_l	latent heat flux density ($W.m^{-2}$)
Q_s	sensible heat flux density ($W.m^{-2}$)
Q_t	total heat flux density ($W.m^{-2}$)
Re	Reynolds number
T	temperature, (K)
U_0	gas inlet velocity, ($m.^{-1}$)
V_x	longitudinal velocity, ($m.s^{-1}$)
V_y	transverse velocity, ($m.s^{-1}$)
W	mass vapour fraction,
x	longitudinal coordinate, (m)
y	transverse coordinate, (m)

Greek symbols

β	coefficient of thermal expansion, (K^{-1})
ρ	density, ($kg.m^{-3}$)
ϕ	relative humidity of the air-vapour mixture.
ε	porosity
μ	dynamic viscosity, ($kg.m^{-1}.s^{-1}$).
ξ	cooling efficiency.

ISSN: 1737-933442

Indices and exponents

0	inlet
a	air
e	effective
I	interface
L	liquid
m	mixture
out	channel outlet
S	solid
v	vapour
w	wall

Introduction :

- The Double-diffusive convection in porous media are attracting increasing interest for several decades, where the fluid flow is induced by the simultaneous presence of heat and mass transfer. A considerable amount of research has been reported on double-diffusive convection since of its many engineering and technology applications. To enhance the heat and mass transfer, researchers have developed a diversity of effective strengthening heat transfer technologies, such as changing the surface structure using the corrugated wall to increase the heat exchange surface; introducing nanoparticle to change fluid characteristics; and so on. Porous media, as an efficient tool, is also used commonly to enhance heat transfer in many engineering applications because of its high thermal conductivity.

Wan et al. (2018) developed a new method to determine the heat and mass transfer coefficients in the counter-flow dew point evaporative cooler under diverse climatic. The authors investigated the effects of the various conditions on the heat and mass transfer coefficients, including climatic, operating and geometric conditions. Their results showed the capability of the dew point evaporative cooler to achieve higher cooling effectiveness. In addition, the new method provide the accurate data to realize optimum design of the dew point evaporative cooler.

Recently, Sohani et al. (2018) presented a comparative analysis of various kinds of heat and mass exchangers to determine the best design of dew point evaporative coolers at diverse climatic conditions. It was found that the counter regenerative configuration was the ideal choice in very hot and dry areas, while in other investigated climates; the cross configuration was the better alternative.

Dai and Sumathy (2002) investigated a cross-flow direct evaporative cooler with wet honeycomb paper as the packing material. The system was expected to act as both humidifier and evaporative cooler that can create a comfortable indoor environment in arid regions. They presented a mathematical model, which was validated experimentally for theoretical prediction of the system performance. Later, a simplified mathematical model was developed by Fouda and Melikyan (2011) to describe the heat and mass transfer between air and water in a direct evaporative cooler. The relationship between the cooling efficiency and its influence factors for the direct evaporative cooler with porous, durable honeycomb papers as a pad material was considered. The effectiveness of evaporative cooling has been proved in different climatic situations, not only in hot and dry regions where it was initially applied (Dabaieh et al., 2015; Kharrufa and Adil, 2012) but also in hot and humid regions (Zhang et al., 2015, 2016).

In addition, several passive evaporative cooling systems such as intermittent evaporative roof cooling (Alturki and Zaki, 1991; Wang et al., 2008) and two-stage indirect/direct evaporative cooling (Al-Juwayhel et al., 2004; Jain, 2007) have been investigated in order to enhance the cooling effect in an evaporative cooling system and to reduce the dissipated energy caused by the inherent heat and mass transfer resistance need to be achieved in all these systems. Therefore, some physical quantities are necessary to be defined to estimate the cooling ability of the evaporative system and to measure the endothermic ability dissipation during the process. Very recently, Zhang et al. (2017)

ISSN: 1737-933443

presented a novel approach for modelling and analysing the influence of evaporation on roof thermal performance. A multivariate nonlinear model was developed for the prediction of the evaporation rate from a porous tile. Their study focused on a numerical method rather than heat and mass transfer model itself, and a complete discussion about mathematical models was avoided.

A theoretical analysis to free evaporating cooling in unsaturated porous packed bed in houses or buildings was presented by Liu et al. (1995). The simultaneous heat and mass transfer in the porous media unsaturated with liquid was numerically simulated. He et al. (2009, 2010) constructed a passive evaporative cooling wall out of moist void bricks, and Chen et al. (2015) for a pipe-shaped porous ceramics that were capable to absorb water and allowed wind penetration, which consequently reduced their surface temperature via water evaporation. Other authors used ceramic as porous materials. Indeed, Riffat and Zhu (2004) combined porous ceramic and heat pipe into an indirect evaporative cooler. Ibrahim et al. (2003) have built several prototypes of wet porous ceramic materials for building cooling. Achievement of this indirect evaporative cooling has been affected by passing air through a wet porous medium plate.

The main objective of this work is to investigate the heat and mass transfer during the evaporation of liquid film by mixed convection of humid air in a vertical channel with porous wet wall. The liquid and air streams are modeled as two coupled laminar boundary layers incorporating non-Darcian models of the inertia and boundary effects. The governing equations and the associated boundary conditions are discretized by means of the finite volume method implemented on a staggered mesh and the velocity pressure coupling is processed by the SIMPLE algorithm.

Problem Formulation.

Our model consists of a vertical channel formed by two plates of length L = 3 m, spaced by a distance H = 0.04 m (Fig. 1). The internal left wall is assumed adiabatic and covered with a porous material of thickness d, permeability K, and porosity ε. The plate is wetted by a falling water film with an inlet temperature $T_{0;L}$ and inlet mass flow rate $m_{0;L}$, used as a porous evaporative plate. The second plate is adiabatic and dry. A laminar ambient air flows along the channel with a uniform velocity U_0, temperature T_0, and relative humidity ϕ_0.

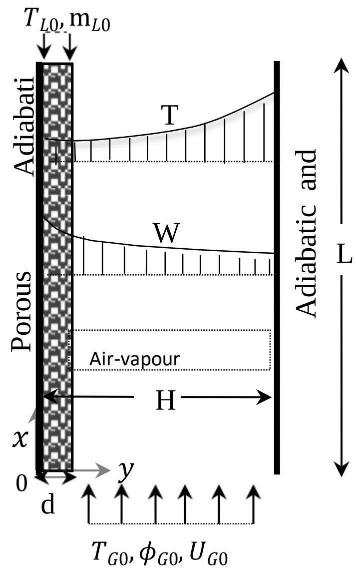

Figure 1: *Schematization of the physical problem and boundary conditions*

- Basic equations for the liquid film

ISSN: 1737-933444

$$0 = -\rho_L\, g + \frac{\partial}{\partial y}\left(\frac{\mu_L}{\varepsilon}\frac{\partial V_x}{\partial y}\right) - \frac{\mu_L}{K}V_x - \frac{\rho_L C}{\sqrt{K}}V_x^{2} \tag{1}$$

$$\frac{\partial}{\partial x}\left(\rho_L V_x C_{p,L} \mathrm{T}\right) = \frac{\partial}{\partial y}\left(k_e \frac{\partial \mathrm{T}}{\partial y}\right) \tag{2}$$

- **Basic equations for gas flow**

$$\frac{\partial(\rho_m V_x)}{\partial x} + \frac{\partial(\rho_m V_y)}{\partial y} = 0 \tag{3}$$

$$\frac{\partial(\rho_m V_x^2)}{\partial x} + \frac{\partial(\rho_m V_x V_y)}{\partial y} = -\frac{\partial p}{\partial x} + \rho_m\, g + \frac{\partial}{\partial x}\left(\mu_m \frac{\partial V_x}{\partial x}\right) + \frac{\partial}{\partial y}\left(\mu_m \frac{\partial V_x}{\partial y}\right) \tag{4}$$

$$\frac{\partial(\rho_m V_y V_x)}{\partial x} + \frac{\partial(\rho_m V_y^2)}{\partial y} = -\frac{\partial p}{\partial y} + \frac{\partial}{\partial x}\left(\mu_m \frac{\partial V_y}{\partial x}\right) + \frac{\partial}{\partial y}\left(\mu_m \frac{\partial V_y}{\partial y}\right) \tag{5}$$

$$\frac{\partial(\rho_m V_x C_p \mathrm{T})}{\partial x} + \frac{\partial(\rho_m V_y C_p \mathrm{T})}{\partial y} = \frac{\partial}{\partial x}\left(k_m \frac{\partial \mathrm{T}}{\partial x}\right) + \frac{\partial}{\partial y}\left(k_m \frac{\partial \mathrm{T}}{\partial y}\right) \tag{6}$$

$$\frac{\partial(\rho_m V_x W)}{\partial x} + \frac{\partial(\rho_m V_y W)}{\partial y} = \frac{\partial}{\partial x}\left(\rho_m D_m \frac{\partial W}{\partial x}\right) + \frac{\partial}{\partial y}\left(\rho_m D_m \frac{\partial W}{\partial y}\right) \tag{7}$$

Boundary conditions and used expressions

The boundary conditions associated with this problem, are given as follow:

At the inlet: $x = 0$

For the liquid $0 < y < d$: $\mathrm{T} = \mathrm{T}_{0,L}$ $m_L = m_{0,L}$ (8)

For the gas $d < y < H$: $V_{x,m} = U_{0,m}$ $V_{y,m} = 0$ $\mathrm{T} = \mathrm{T}_{0,m}$ $\phi = \phi_{0,m}$ (9)

At the walls:

$y = 0$: $V_{x,L} = 0$ $\left.\frac{\partial T}{\partial y}\right|_{y=0} = 0$ (10)

$y = H$: $V_{x,m} = V_{y,m} = 0$ $\left.\frac{\partial T}{\partial y}\right|_{y=H} = 0$, $\left.\frac{\partial W}{\partial y}\right|_{y=H} = 0$ (11)

At the outlet: $x = L$ and $d < y < H$

$$\frac{\partial V_x}{\partial x} = \frac{\partial V_y}{\partial x} = \frac{\partial T}{\partial x} = \frac{\partial W}{\partial x} = 0 \tag{12}$$

At the interface: $y = d$

The solution from the liquid side and gas side satisfies the following interfacial matching conditions:

- Continuities of velocity and temperature

$$\mathrm{V}_{x,\mathrm{I}} = \mathrm{V}_{x,I,m} = \mathrm{V}_{x,I,L} \qquad T_{\mathrm{I}} = T_{I,m} = T_{I,L} \tag{13}$$

ISSN: 1737-933445

- Continuity of shear stress

$$\tau_I = \left[\mu \frac{\partial V_x}{\partial y}\right]_{I,L} = \left[\mu \frac{\partial V_x}{\partial y}\right]_{I,m} \qquad (14)$$

- The transverse velocity component of the air-vapour mixture at the interface is calculated by :

$$V_e = -\frac{D_m}{1 - W_I} \frac{\partial W}{\partial y}\bigg|_I \qquad (15)$$

Résultats :

This study investigates the characteristics of heat and mass transfer process between two vertical parallel walls with a wetted porous wall used as an evaporative cooler, with particular emphasis on studying the factors affecting the thermal and mass performances. Evaporative cooling is a heat and mass transfer process that uses water evaporation for air-cooling, in which a large amount of heat is transferred from air to water, involving consequently, a decrease of ambient air temperature and a rises of its relative humidity.

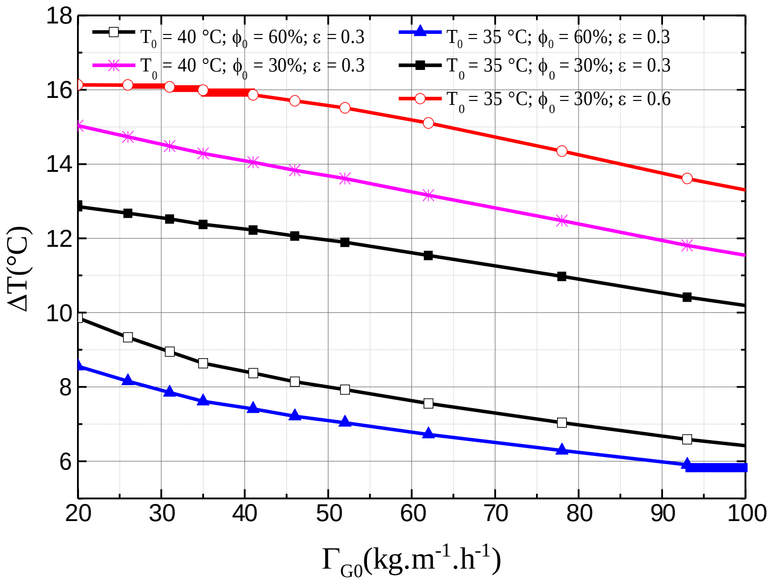

Figure 2 *: Variation of the temperature drop as a function of the inlet airflow for various considered parameters*

Figure 2 shows the variation of the temperature deference between the inlet and the outlet of the channel, as a function of the airflow at the inlet, and this, for different values of the temperature and humidity of the air at the entrance as well as the thickness of the porous layer.

This figure shows that the increase of the inlet air mass flow induces the decrease of the temperature deference. Indeed, at high airflow at the entrance, the required contact time between the air and the surface decreases. As a result, the gas temperature on the channel axis decreases due to evaporation. The most intense decrease is observed for low values of the airflow at the entrance. Indeed, for a flow of air mG0 < 70 kg.m-1.h-1, the difference in temperature decreases slightly. It is also noted

ISSN: 1737-933446

that for fixed moisture and porosity, the air-cooling is improved for high values of inlet air temperature and porosity. Regarding the effect of air humidity at the inlet, we note that its increase deteriorates the performance of cooling, since a small differences in temperature are noted.

The effect of the inlet air parameters as well as the characteristics of the porous layer on the evolution of the difference of the relative humidity of the ambient air between the inlet and the outlet of the evaporative cooler are represented in Figures 5 and 6.

The figures show that the difference in the humidity of the air decreases as a function of the air flow at the inlet. This decrease is more important as the air flow at the entrance is large. It should be noted in Figure 5 that the effect of the parameters considered, namely: temperature and porosity, is small on the relative humidity however, the relative humidity of the air is more important.

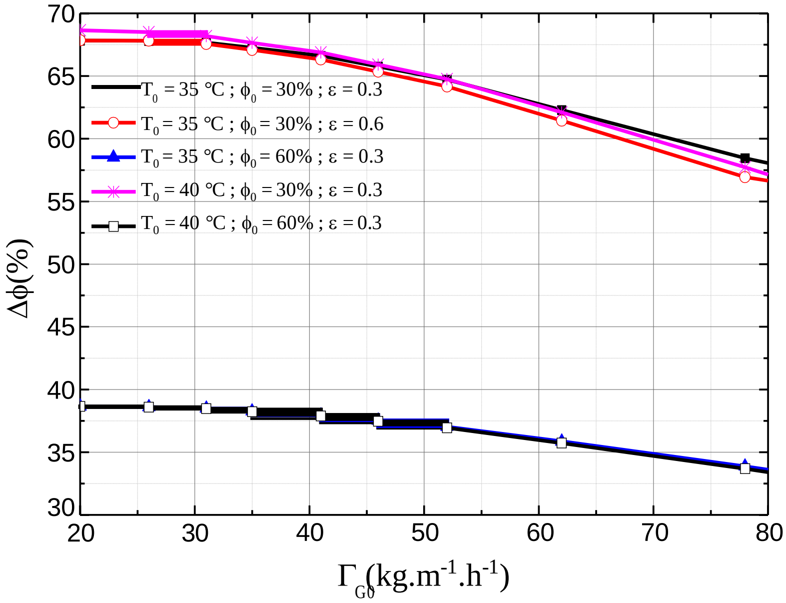

Figure 3 : Variation of the air relative humidity drop as a function of the airflow.

Conclusion:

- This paper presents a two dimensional numerical study to describe heat and mass transfer during the evaporative cooling process from porous media. This article has reported the investigation of the effect of the imposed inlet air mass flow, porous layer thickness and porosity on the evaporative cooling performance.

The results show a drop in the temperature of air proportional to the sensible heat and an increase in humidity proportional to the latent heat drop. The lower ambient relative humidity causes a high evaporation rate in the porous evaporative cooling plate. Moreover, the increase in the thickness of the porous layer causes the increase of the temperature difference between the porous media and the ambient air.

Reference:

1. Al-Juwayhel, F., El-Dessouky, H., Ettouney, H., Al-Qattan, M., 2004, Experimental evaluation of one, two, and three stage evaporative cooling systems. Heat Transfer Eng. 25(6), 72-86.

2. Alturki AM, Zaki GM. Energy saving through intermittent evaporative roof cooling. Energy Build. 17(1), 35–42.

3. Chen, W., Liu, S. and J. Lin, 2015, Analysis on the passive evaporative cooling wall constructed of porous ceramic pipes with water sucking ability, Energy Build. 86, 541–549.

4. Dabaieh, M., Wanas, O., Hegazy, M.A., Johansson, E., 2015, Reducing cooling demands in a hot dry climate: a simulation study for non-insulated passive cool roof thermal performance in residential buildings, Energy Build. 89, 142–152.

5. Dai, Y.J., Sumathy, K., 2002, Theoretical study on a cross-flow direct evaporative cooler using honeycomb paper as packing material, Applied Thermal Engineering. 22, 1417–1430.

6. Fouda, A., Melikyan, Z., 2011, A simplified model for analysis of heat and mass transfer in a direct evaporative cooler, Applied Thermal Engineering. 31, 932-936.

7. He, J. and Hoyano, A., 2009, A 3D CAD-based simulation tool for prediction and evaluation of the thermal improvement effect of passive cooling walls in the developed urban locations, Sol. Energy. 83 (7), 1064–1075.

8. He, J., and Hoyano, A., 2010, Experimental study of cooling effects of a passive evaporative cooling wall constructed of porous ceramics with high water soaking-up ability, Build. Environ. 45 (2), 461–472.

9. Ibrahim, E., Shao, L., Riffat, S.B., 2003, Performance of porous ceramic evaporators for building cooling application. Energy Build. 35(9), 941-9.

10. Kharrufa, S.N. and Adil, Y., 22012, Upgrading the building envelope to reduce cooling loads, Energy Build. 55, 389–396.

11. Liu, W., Peng, S. W., Mizukami, K., 1995, A general mathematical modelling for heat and mass transfer in unsaturated porous media: an application to free evaporative cooling, Heat and Mass Transfer. 31, 49-55.

12. Patankar S.V, 1980, Numerical heat transfer and fluid flow, Hemisphere.

13. Riffat, S.B. and Zhu, J., 2004, Mathematical model of indirect evaporative cooler using porous ceramic and heat pipe. Appl Therm Eng 24(4), 457-70.

14. Sohani A, Sayyaadi H, Mohammadhosseini N., 2018, Comparative study of the conventional types of heat and mass exchangers to achieve the best design of dew point evaporative coolers at diverse climatic conditions, Energy Conversion and Management 158, 327–345.

15. Wang, XC, Niu, JL, Van Paassen, AHC, 2008, Raising evaporative cooling potentials using combined cooled ceiling and MPCM slurry storage. Energy Build. 40, 1691–8.

16. Zhang, L., Feng, Y., Meng, Q., Zhang, Y., 2015, Experimental study on the building evaporative cooling by using the Climatic Wind Tunnel, Energy Build. 104, 360–368.

17. Zhang, L., Liu, X., Meng, Q., Zhang, Y., 2016, Experimental study on the impact of mass moisture content on the evaporative cooling effect of porous face brick, Energy Effic. 9 (2), 511–523.

18. Zhang, L., Zhang, R., Zhang, Y., Hong, T., Meng, Q., Feng, Y., 2017, The impact of evaporation from porous tile on roof thermal performance: A case study of Guangzhou's climatic conditions, Energy and Buildings. 136, 161–172.

ISSN: 1737-933448

Optimization of surface roughness by the tribofinishing process with the use of Box-Behnken experimental designs

D. SAIDI[1], M.A. DJEMA2, K. HAMOUDA[2],M. BOUAZIZ[1]

1. Ecole Nationale Polytechnique, Alger, Algérie
2. Université des Sciences et de la Technologie Houari Boumediene, Alger, Algérie
e-mail: djamel.saidi@g.enp.edu.dz

Abstract

This work presents an experimental research of the influence of the three important parameters (frequency, amplitude, abrasive size) on surface roughness during tribofinishing treatment.

The process of tribofinishing is investigated as a means to reach a state of quality for the surface treated, this work consists in treatment on cylindrical samples of AA 2017 aluminium alloys in order to improve the surface state, using Box-Behnken design which is a power full tool for experimental design is used to optimize the process parameters. Box-Behnken design method as well as analysis of variance (ANOVA) is used to analyze the influence of parameters of treatment on surface roughness Ra.

The optimum process parameters for minimum surface roughness in tribofinishig process have been obtained and validated with the experiments and found highly satisfactory results.

Keywords: Box–Behnken design, tribofinishing, roughness, frequency, amplitude, abrasive size

1. Introduction

The tribofinishing process is a mechanical-chemical process which aims to remove small particles of metal and its oxides by micro blows that the surface receives, which generates plastic deformation while causing surface hardening.

This method was inspired by nature where the constant flow of water transforms rough stones into perfectly polished pebbles.

Tribofinishing is a process to improve the surface state of mechanical parts that includes: elimination of rough edges, burrs, also to round off angles, to polish, with a technology that uses unguided cutting tools **(**abrasive particles)[1, 2]
The ability of mechanical parts to insure a particular function depends on some parameters, such as microstructure, superficial geometrical and mechanical characteristics
[3, 4].

To obtain such a surface state, many methods such grinding, superfinishing, lapping, etc… are used [5, 6].

Some of these processes are relatively expensive and cannot be adapted perfectly to complex geometries of the specimen used. Tribofinishing is a suitable process used to improve complex geometries characteristics. It acts by removing small metal particles and oxides from the treated surface [7, 8, 9].

Achievement of surface quality is obtained by continuous friction between the work pieces and the particles (generally porcelain balls) acting as abrasives [10].

ISSN: 1737-933449

This study focuses on the application of tribofinishing treatment (porcelain balls) on aluminium alloy (AlCu4MgSi) AA 2017, and parameters optimization of treatment regime.

The process parameters that were taken into consideration are: frequency, amplitude and abrasive size, using Box-Behnken design.

In 1960, Box and Behnken proposed designs that allow us to directly implement seconddegreemodels. All the factors have three levels: –1, 0, and 1.

These designs are easy to carry out and have the property of sequentiality.

The Box-Behnken design for three factors is constructed on a cube.

The experimental points are placed not at the corners of the cube, but in the middle of the edges. This arrangement means that all experimental points are placed equidistant from the center of the study domain. Center points are added to the study domain [11,12].

The Box-Behnken design for three factors is shown in Figure 1. The cube has 12 edges. Traditionally, three experimental points are placed at the center of the study. Box-Behnken designs for three factors therefore have 12 +3 = 15 trials [13, 14].

We have developed an empirical mathematical model to illustrate the relationship between these three parameters and the response roughness “Ra”.
In this study, the design and analysis have been carried using Design-Expert version 10.

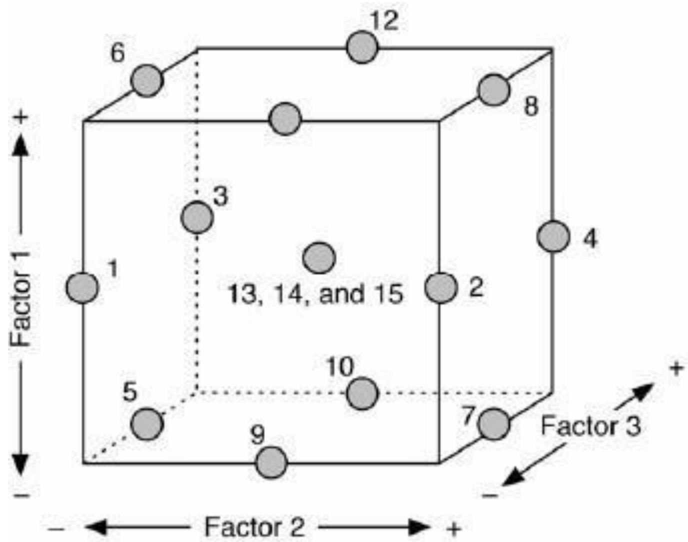

Figure 1 Illustration of the Box-Behnken design for three factors. There are twelve experimental points at the center of each edge, and three points at the center of the cube.

2. Surface roughness measurement

Surface roughness is one of the important parameters toassess the product quality or surface quality. This factor has asignificant effect on functionality as well as esthetic aspects ofthe product.

The most commonly used parameter to quantifythe surface roughness is arithmetic mean surface roughnessvalue (Ra). $Ra$is the arithmetic average of the absolute valuesof the roughness profile ordinates or the integral of the absolute value of the roughness profile height over the evaluationlength. Mathematically this can be described by the following relation [8].

$$Ra = \frac{1}{L}\int_0^L |z(x)|dx \qquad (1)$$

ISSN: 1737-933450

3. Experimental setup

The experimental tests were carried out on AA 2017 using a brand type (УВГ 4 x 10)linear vibrator (Figure 2). The total duration of tribofinishing treatment is 240 minutes, with a variation of parameters (frequency, Amplitude, Abrasive size).

The work pieces are put into the working chamber of the vibrator which is filled with porcelain balls and chemical additives. The vibrator receives a low frequency vibration and can move freely in the space three directions.

The working chamber is ring shape with a flat bottom which ensures a perfect immersion of the parts in the abrasive charges.

The treated parts are usually removed manually.

Machine Features

- Working chamber capacity: 10 dm^3
- Number of working chamber: 4
- Engine power (KW) 1
- Dimensions (mm) 1300 X 952 X 1370
- Type pumpПА-22
- Power (KW)0.12
- Flow rate (l/min) 22
- Particle nature: Porcelain balls
- Net weight of particles: 5 kg.
- Chemical Additive: Lauryl Ether Sulfate ($C_{12}H_{25}O_4S$) in one liter of water.
- Treatment time: 60min.

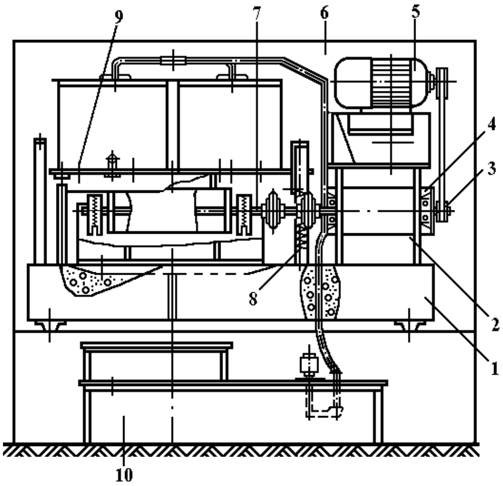

Figure 2 Schematic of the experimental linear vibrator.

1- Foundation
2- Intermediate shaft
3- System belt transmission
4- Maine shaft
5- Electric motor
6- Lubricating system
7- Elastic sleeve
8- Unbalance
9- Working chamber
10- Ferry reservoir.

Process parameters and experimental design

The summary of the parameters used for this study are in the table 1.

Table 1 Process parameters and their levels

Parameters	Variation Levels		
	Low (-1)	Medium (0)	High (+1)
Frequency (Hz)	15	33	50
Amplitude (mm)	1.5	3	5
Abrasive size (mm)	6	8	10

This study evokes a Box-Behnken design which requires 3-levels of each factor coded as -1, 0 and 1.

ISSN: 1737-933451

In order to observe parameter effects on surface state, testing scheme are shown in figure 3.

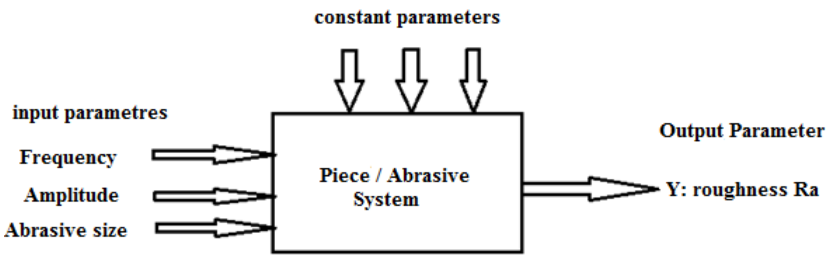

Figure 3Testing scheme

Experimentations

The design matrix, including the recorded experimental values for the roughness, is presented in table 2.

Table 2 Design matrix with their experimental values of roughness (Ra)

Test Number	Independent Variables			Response
	Frequency (Hz)	Amplitude (mm)	Abrasive size (mm)	Roughness Ra (µm)
1	15	1.5	8	1.610
2	50	1.5	8	1.488
3	15	5	8	1.600
4	50	5	8	1.358
5	15	3	6	1.592
6	15	3	10	1.606
7	50	3	6	1.412
8	50	3	10	1.454
9	33	1.5	6	1.570
10	33	5	6	1.516
11	33	1.5	10	1.582
12	33	5	10	1.538
13	33	3	8	1.556
14	33	3	8	1.556
15	33	3	8	1.556

The dimensions and the roughness measured samples are presented in figure 4.

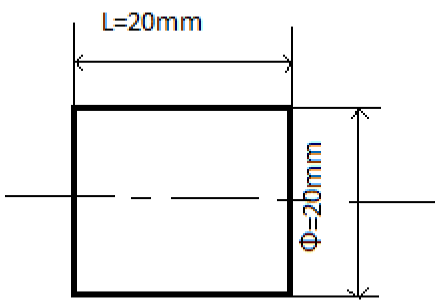

Figure 4 Roughness measured samples.

ISSN: 1737-933452

Chemical composition of the work piece was 86.15% Al and 5.51% Cu, as confirmed by SEM image (shown in figure 5).

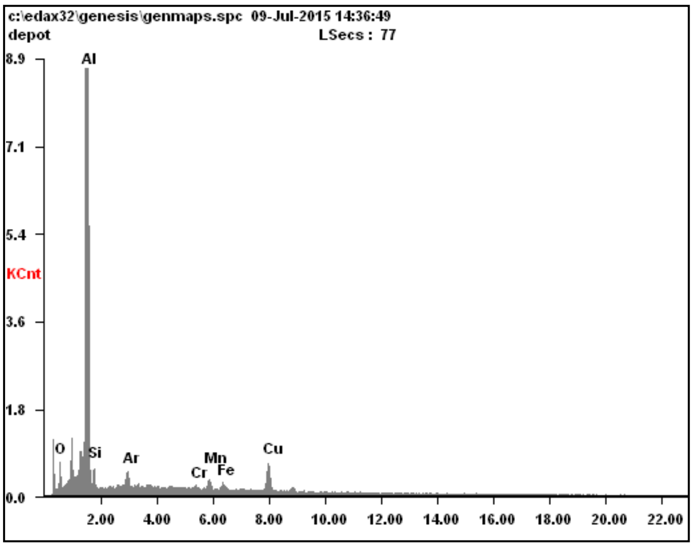

Figure 5 SEM image

4. Results and discussion

The general equation for the proposed second order regression model to predict the response Y can be written as:

$$Y = a_0 + a_1x_1 + a_2x_2 + a_3x_3 + a_{12}x_1x_2 + a_{13}x_1x_3 + a_{23}x_2x_3 + a_{11}x_1^2 + a_{22}x_2^2 + a_{33}x_3^2 + e \quad (2)$$

Where:

- Y: Response
- a: Coefficient
- x: variable
- e: Prediction error.

To formulate the effect of selected process parameters on surface roughness, the modeller software was given inputs of measured responses (Ra values) for all experimental runs. The surface roughness was modelled in terms of frequency, amplitude and abrasive size as follows:

- **Final Equation in Terms of Coded Factors:**

$$Ra = +1.56 - 0.088 * A - 0.030 * B + 0.010 * C - 0.030 * AB + 9.500E - 003 * AC + 2.500E - 003 * BC - 0.038 * A^2 - 4.500E - 003 * B^2 + 0.000 * C^2 \quad (3)$$

Statistical results

Using analysis of variance (ANOVA), the effects of frequency, amplitude, abrasive size and their second order interactions on surface roughness were calculated. (See table 3)

Table 3Analysis of variance (ANOVA) for Response Surface Quadratic model

Source	DF	SS	MS	F	P
Model	9	0.080	8.91E-003	208.86	<0.0001 significant
A Frequency	1	0.062	0.062	1458.63	<0.0001
B Amplitude	1	7.080E-003	7.080E-003	165.76	<0.0001
C Abrasive size	1	8.000E-004	8.000E-004	18.73	0.0034
AB	1	3.600E-003	3.600E-003	84.28	<0.0001
AC	1	3.610E-004	3.610E-004	8 .45	0.0228
BC	1	2.500E-005	2.500E-005	0.59	0.4693
A^2	1	5.921E-00	5.921E-003	138.62	<0.0001
B^2	1	8.526E-005	8.526E-005	2.00	0.2006
C^2	1	0.000	0.000	0.000	1.0000
Residual	7	2.990E-004	4.271E-005		
Lack of Fit	3	2.990E-004	9.967E-005		
Pure Error	4	0.000	0.000		
Cor Total	16	0.081			

R-Squared 0.9963, The "Pred R-Squared" of 0.9406 is in reasonable agreement with the "Adj R-Squared" of 0.9915; i.e. the difference is less than 0.2.
Values of "Prob> F" less than 0.0500 indicate model terms are significant.
In this case A, B, C, AB, AC, A^2 are significant model terms.

Graphical results

Figure 6 show the perturbation plot of surface roughness. This perturbation plot compares the effect of every factor at a particular point in the design space (Design Expert, 10)
The roughness decreases when increasing the frequency and amplitude and the abrasive size decreases.

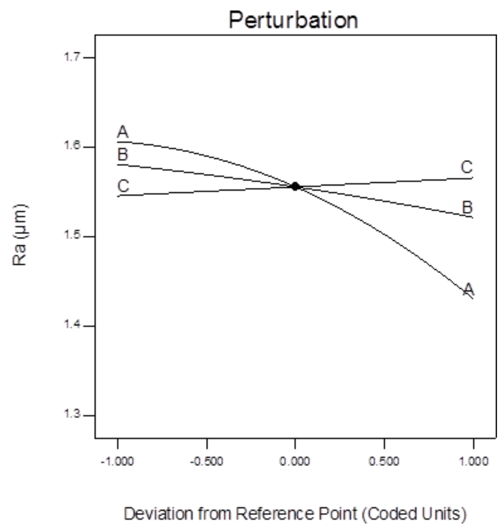

Figure 6 Perturbation plot for surface roughness.

ISSN: 1737-933454

Response Surface Plot

In order to gain a better understanding of the interactioneffects of variables on surface roughness, three-dimensional (3D)plots for the measured responses were formed based on themodel equation (4). Also the relationship between thevariables and responses can be further understood by theseplots. Since model has three variables, one variable is held constant at medium level; therefore, a total of 6 responsesurface plots were produced for responses.

The relationship between variables and their influence onthe response, the surface roughness, is shown in Figure 7which showsthe influence of frequency and amplitude onthe surface roughness.

It indicates that surface roughnessdecreases.

In others words, Figures 7, 8 and 9indicate that frequency, amplitude, and abrasive size have considerable influence on the surface roughness.

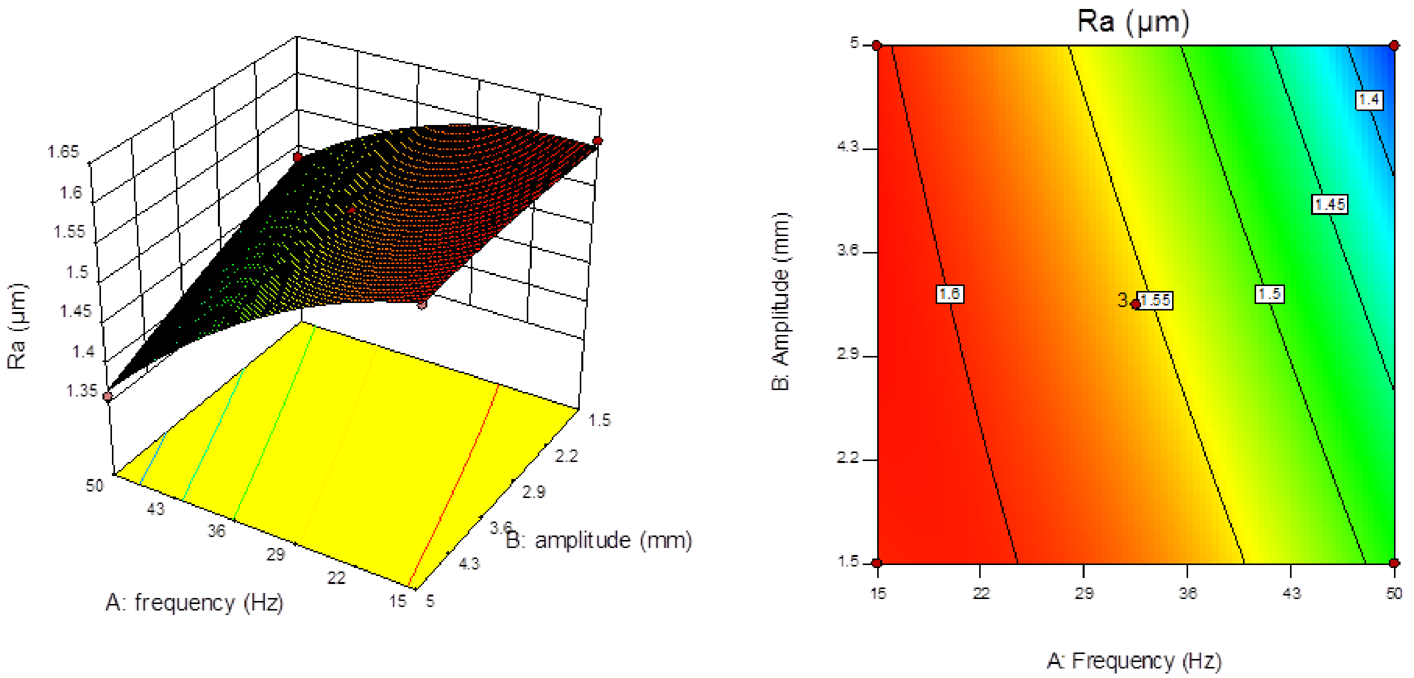

Figure 7Response surface plots showing effect oftwo variables (frequency, amplitude) on surface roughness

ISSN: 1737-933455

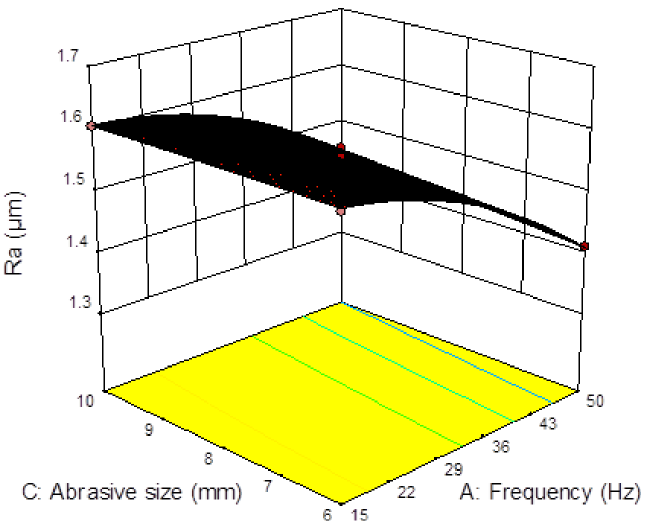

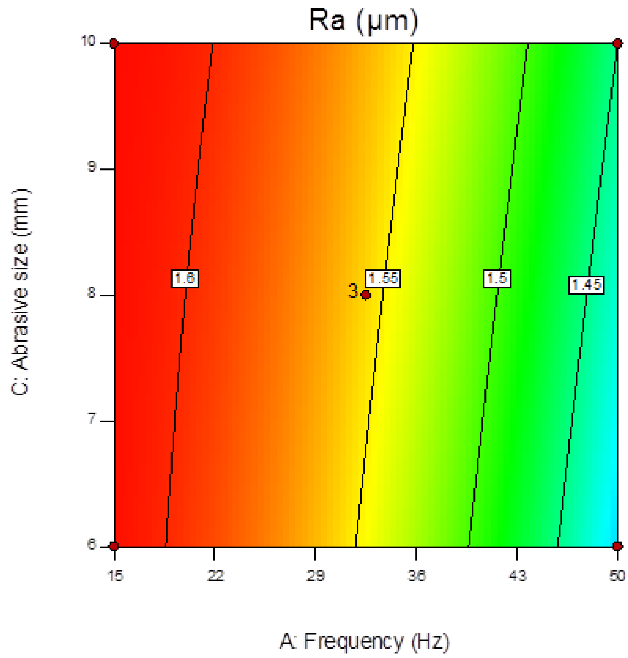

Figure 8Response surface plots showing effect of two variables (frequency, abrasive size) on surface roughness

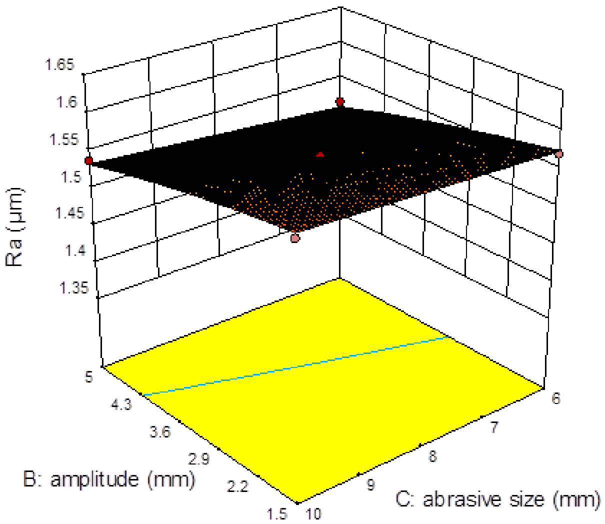

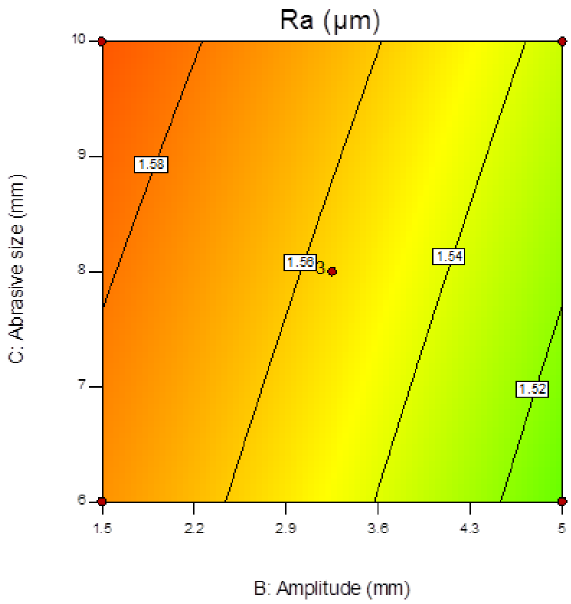

Figure 9Response surface plots showing effect of two variables (amplitude, abrasive size) on surface roughness

Figure 9a and figure 9b shows a comparison between predicted and actual values of the response and confirms that the results obtained are in a good agreement with the predicted values.

Additionally, the developed response surface model for Ra has been checked by using residual analysis.

The residual plots for Ra are shown in Figures. 10a-10b. In normal probability plot, the data are spread approximately in a straight line, which show a good correlation between experimental and predicted values for the response (Figure 10a).

Figure 10b is the plot of the residuals calculated against the order of experimentation. It is asserted that a tendency to have runs of positive and negative residuals indicate the existence of correlation. From the above analysis of residual plots for Ra, the model does not reveal inadequacy.

ISSN: 1737-933456

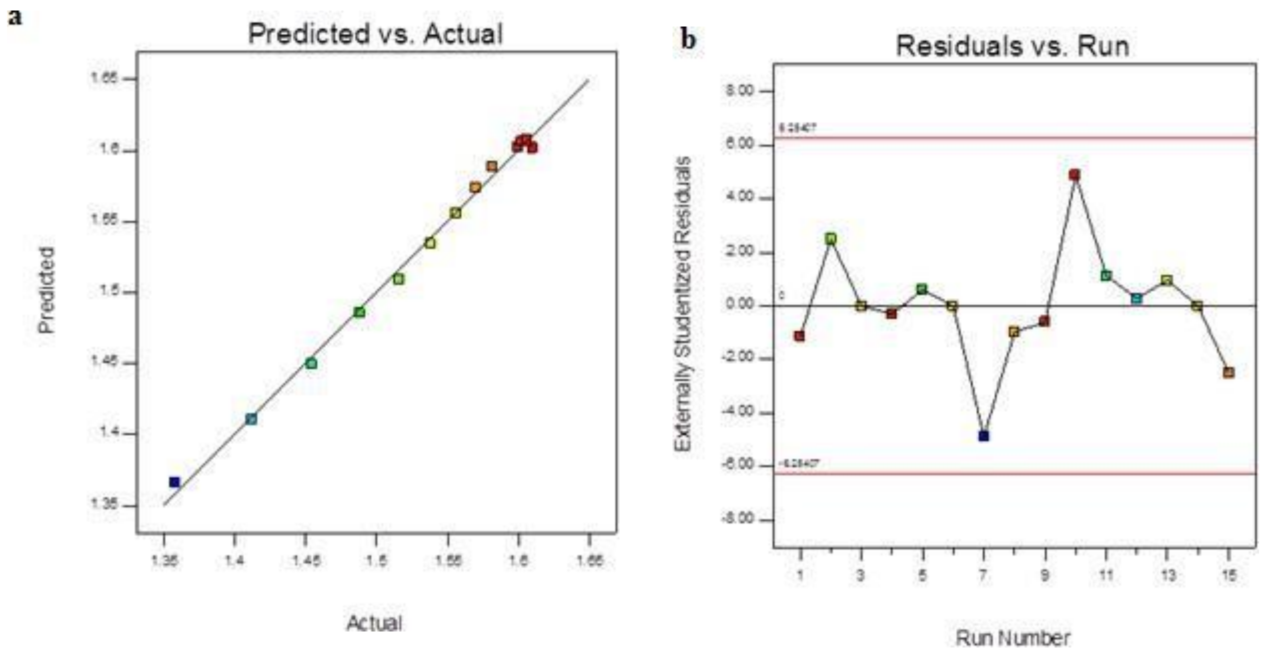

Figure 10 Relation between experimental and predicted values (a), Residual analysis (b)

Hardened layer

Figure 11 illustrates the hardened layer that appears on the SEM image, in light graycolor in the order of 100 microns with an X350 magnification, observed by a scanning electron microscope (SEM) JEOL JSM-type 6360

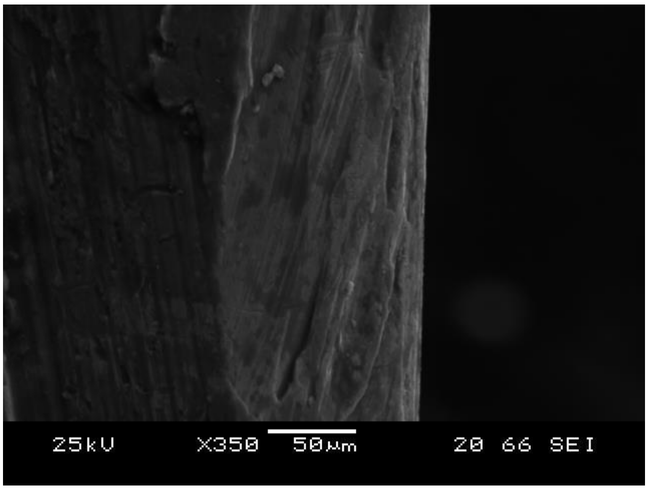

Figure 11 Hardened layer

Conclusions

In this study, optimization of parameters (frequency, amplitude, abrasive size)during tribofinishing process has been carried out.

ISSN: 1737-933457

The surface roughness response Ra has been modeled and analyzed through response surface methodology (RSM).
A Box-Behnken design was used to carry out the experimental study.

Analysis of variance (ANOVA) was used to analyze the effect of the parameters on the response.

In summary, the following conclusions can be drawn:

1. The frequency is found to be the most importantparameter effecting Ra, followed by amplitudewhile abrasive size has the least effect.

2. The predicted value of Ra matches the experimentalvalues reasonably well, with high value of coefficientof determination ($R2 = 0.9963$) for Ra.

3. The variation in percentage error for Ra is between 1 to5%, which shows that the model developed for Ra isaccurate, and can be used for predicting the surfaceroughness.

Acknowledgements

The authors gratefully acknowledge VIBROTECH laboratory for the cooperation and help. The authors are also thankful toVIBROTECH laboratory for providing the linear vibrator to achieve the experimental testing.

References

[1] M. A. Tamarkin, Theoretical principles of optimization processing of mechanical parts in free abrasive particles, as PhD thesis, 1995 Russia.
[2] Surface treatments and coatings for tribological purposes, CETIM, GAMI, 1994 ISBN 2-85400-333-0
[3] A. P. Babichev, P.D. Motrenko, Using the Vibration technology for improving the surface quality and the mechanical characteristics, 2006, ISBN 5-7890-0390-7
[4] A. P. Babichev, improving the fatigue strength of non-ferrous materials by tribofinishing process, 2010.
[5] A. P. Babichev, I. A. Babichev, Principles of vibration technology, 2008, ISBN 978-5-7890-0472-2
[6] Jacques Goupy, Lee Creighton, Introduction to design of experiments, SAS Publishing, 2007
[7] Jacques Goupy, Pratiquer les plans d'expériences, Dunod, 2005
[8] Alain Cornet, Jean-Paul Deville, Physics and surface engineering, 1998, ISBN 2-86883-352-7
[9] [2] F. Hashimoto, Modeling and Optimization of Vibratory Finishing Process, CIRP Ann. Manuf. Technol. 45 (1) (1996) 303–306.
[10] Mohammad Reza Baghbanan, Akihiro Yabuki, Roland S. Timsit, Jan K. Spelt, Tribologicalbehavior of aluminum alloys in a vibratory finishing process, Wear, 255 (2003), 1369-1379.
[11] VOLKER SCHULZE, Modern Mechanical Surface Treatment, Edition WILEY-VCH, 2006.
[12] DOUGLAS C. MONTGOMERY, Design and analysis of experiments, Publisher: JOHN WILEY & SONS, 5th Edition, 2001.
[13] LAROUX. K. GILLESPIE, Mass Finishing Handbook, Edition Industrial Press New York, 2007.
[14] LAROUX. K. GILLESPIE, Deburring and Edge Finishing, Handbook, Edition SME, 1999

Evaluating the Efficiency of Municipal Solid Waste Collection in Tunisian's Municipalities using Data Envelopment Analysis

Sabrine Ismail[#1], Habib Chabchoub[*2], Soulef Smaoui[#3]

[#] *Quantitative Methods, Faculty of Economics and Management, Sfax, Tunisia*

* *College of Business, Al Ain University, Abu Dhabi,UAE*

Email 1 - sabrineismail9@gmail.com
Email 2 - habib.chabchoub@aau.ac.ae

Email 3 - soulef.smaoui@gmail.com

Abstract

Municipal solid waste (MSW) collection plays a crucial role in achieving sustainability goals within municipalities.Systems for collecting waste that are efficient are crucial for protecting the environment, encouraging resource conservation, and enhancing public health.In this paper, we study the efficiency of 23 municipalities in Sfax City, Tunisia in order to evaluate their performance and identify the sources of inefficiencies.The Data Envelopment Analysis (DEA) method has been chosen to address our objective.

Keywords: Municipal Solid Waste Collection, Sustainability, Data Envelopment Analysis.

1 Introduction

Municipal Solid Waste Management, including Municipal Solid Waste Collection, has been garnering growing attention from scholars, economists, technical staff, and other stakeholders [15].Proper disposal of MSW is vital to safeguard environmental quality, human health, and natural resources. By adopting sustainable waste management strategies, communities can address the economic, environmental, and social impacts of waste while working towards achieving long-term sustainability goals [9].This study primarily aims to pinpoint best practices for MSW collection and establish performance targets by identifying areas of excessive resource consumption and areas that require improvement. To accomplish these objectives, DEA will be utilized as a suitable method.

The remainder of this paper is structured as follows:Section 2 is dedicated to the literature review, while Section 3 elaborates on the DEA methodology. In Section 4, the case study is

ISSN: 1737-933458

presented, and Section 5 focuses on the discussion of the results. Lastly, the conclusion is presented.

2 Literature review

The DEA methodology has been widely employed in numerous studies to address MSW-related issues. Among these studies, some notable examples includeSánchez (2006) [13] whoconducted an analysis of the waste collection schemes in 34 municipalities in Spain. For this study, he considered the total staff as an input and two outputs, namely tonnage collected and collection points.In 2011, De Jaeger *et al.* [6] examined the state of Municipal Solid Waste Management (MSWM) in 299 municipalities in Belgium. The inputs selected for the study were costs, and the five outputs analyzed were residual waste, packaging waste, paper and cardboard waste, glass, and other separately collected waste.The following year, Rogger and De Jaeger [11] implemented the shared input DEA approach in 293 municipalities of Belgium. For this analysis, waste costs were chosen as the input, and six outputs were considered: residual waste, other municipal waste, packaging waste, other EPR-waste, green waste, and bulky waste.In his study encompassing 103 municipalities in Italy, Lo Storto [8] utilized annual expenditures as inputs, while urban infrastructure development, urban ecosystem quality, nursery schools, municipality area extension, and resident population were considered as outputs.Struk *et al.* [16] employed a one-stage DEA approach to assess the efficiency of 400 municipalities in Czech Republic. For this evaluation, expenditures were taken as the input indicator, while population, number of dwellings, and serviced area served as the output indicators.In 2017, Sarra *et al.* [14] conducted an analysis of 289 municipalities in Italy, focusing on waste-related factors. For their study, they chose waste costs as the input, and two outputs were considered, one being desirable and the other undesirable.Yang *et al.* [17] utilized a three-stage DEA methodology to evaluate 34 cities in China. The selected inputs for the analysis were the number of Vehicles and Equipment Designated for Municipal Environmental Sanitation and Fixed Assets Investment in the Public Facilities of Municipal Environmental Sanitation. The output indicators considered were the Quantity of MSW Collected and Transported and the MSW Harmless Treatment Rate.

3 Data Envelopment Analysis method

An effective method utilized to assess the performance of Sfax's municipalities is DEA. It is proposed by Charnes et *al*. [5] in 1978. Employing a non-parametric approach, DEA

ISSN: 1737-933459

evaluates the efficiency and productivity of entities known as decision-making units (DMUs) [10].DEA finds application in a wide array of settings, encompassing financial institutions, hospitals, the US Air Force, airports, schools, rates departments, and courts, among others [1].The relative efficiency of homogenous decision-making units (DMUs) is evaluated using DEA. In this context, inputs are the resources that a DMU uses, and outputs are the products the DMU produces or measures in terms of performance [2]. The efficiency score when dealing with multiple inputs and outputs is determined by calculating the weighted sum of outputs divided by the weighted sum of inputs [4]. DEA employs two fundamental models, resulting in the identification of two distinct efficiency frontiers. The first one is known as the Charnes, Cooper, and Rhodes (CCR) model [5] and the second model is referred to Banker, Charnes, and Cooper (BCC) model under both Constant Returns to Scale (CRS) assumption and Variable Returns to Scale (VRS) assumption, respectively[3]. Model orientation can be whether input or output orientation. The selection depends on whether the goal is to minimize inputs or maximize outputs.DEA's strength lies in its ability to handle multiple inputs and outputs when evaluating the relative efficiencies of a group of homogeneous DMUs [12].

4 Case study

The DEA method is applied to assess the efficiency of MSW management in Sfax City.Sfax, situated in the Republic of Tunisia in North Africa, is the second-largest city in the country. Notably, it faces environmental challenges due to pollution levels. In 2019, the population of Sfax was approximately 1,007,592 inhabitants, leading to the production of 233,982 tons of municipal solid waste during that year, which is equivalent to 0.1795 kg per person per day. Sfax City is composed of a total of 23 municipalities presented in Figure1.

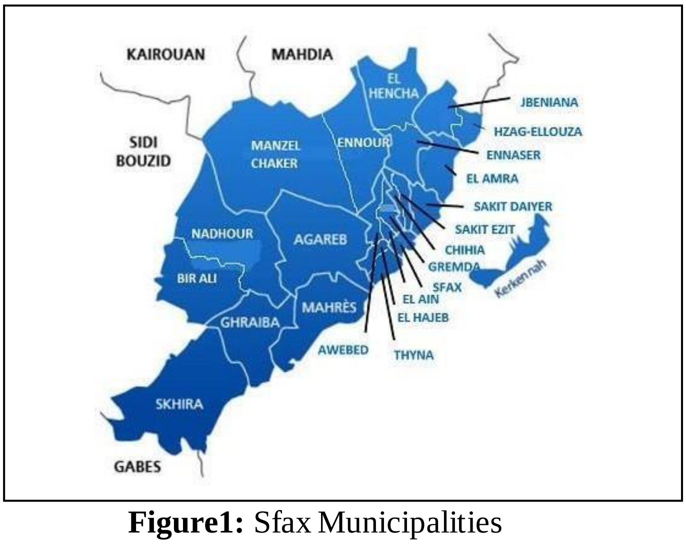

Figure1: Sfax Municipalities

Our objective is to assess the performance of Sfax municipalities, examine their efficiencies, and pinpoint the origins of inefficiencies in both inputs and outputs for each municipality. By identifying benchmark members of the efficient set, we can conduct a comprehensive evaluation and discern the specific sources of inefficiency in the process. So, the most appropriate tool to deal with our objective is DEA. First, inputs and outputs must be determined. The first input selected is the number of working hours in order to enhance work-life balance and prioritize employee well-being. By carefully selecting and managing this aspect, we aim to create an environment that fosters a harmonious integration of work and personal life, leading to increased job satisfaction and overall contentment among employees.As part of our strategy to achieve economic sustainability and cost reduction, the second input chosen pertains to the quantity of fuel. By optimizing fuel consumption, we aim to minimize expenses and improve the overall financial efficiency of the operations, ensuring a sustainable and economically viable approach. The output selected was the quantity of waste collected. By effectively managing waste disposal, we aim to curb pollution and mitigate the impact on the environment. This environmentally responsible approach aligns with our commitment to fostering a greener and cleaner future for our municipalities.This metric is widely employed as the primary means of assessing the effectiveness of waste-collecting operations [7]. Next, the model as well as the orientation must be fixed. We have opted for a Variable Returns to Scale (VRS) model with an input orientation since we have to minimize inputs for a fixed quantity of output.

5 Results and interpretations

As previously stated, a Variable Returns to Scale (VRS) model with an input orientation is chosen for the analysis.The efficiency of all municipalities is evaluated using the DEA method, utilizing the DEAP Software as the primary tool for conducting the analysis.The software gives efficiency details for each municipality, empowering local governments to make data-driven decisions and optimize resource allocation for better service delivery and citizen satisfaction.

The first example of a benchmark unit is shown in Figure 2. This benchmark unit serves as a valuable foundation for assessing and improving the overall efficiency of similar entities.

ISSN: 1737-933461

```
Results for firm:      2
Technical efficiency = 1.000
Scale efficiency     = 1.000  (crs)
 PROJECTION SUMMARY:
  variable            original        radial         slack      projected
                         value      movement      movement          value
 output     1         4481.700         0.000         0.000       4481.700
 input      1        52638.000         0.000         0.000      52638.000
 input      2         5354.000         0.000         0.000       5354.000
 LISTING OF PEERS:
  peer    lambda weight
    2       1.000
```

Figure2: Municipality 2 Efficiency Results

Figure 2 shows that municipality 2 isa benchmark; ithas a technical efficiency and a scale efficiency of 100%.The remarkable feat of achieving 100% in both these aspects makes it a shining example for other municipalities to aspire to.

A second result example is presented in Figure 3.

```
Results for firm:      4
Technical efficiency = 1.000
Scale efficiency     = 0.551  (irs)
 PROJECTION SUMMARY:
  variable            original        radial         slack      projected
                         value      movement      movement          value
 output     1         1229.800         0.000         0.000       1229.800
 input      1         9905.000         0.000         0.000       9905.000
 input      2         4563.000         0.000         0.000       4563.000
 LISTING OF PEERS:
  peer    lambda weight
    4       1.000
```

Figure3: Municipality 4 Efficiency Results

Municipality 4 currently exhibits a technical efficiency of 100%, indicating optimal performance and effective resource management and operational practices. However, there is room for improvement by adjusting its size, which has the potential to lead to significant input savings. If properly optimized, it could potentially reduce inputs by 44.9% (100% - 55.1%), further enhancing its overall efficiency.

A third example concerning municipality 5 is presented in Figure 4.

ISSN: 1737-933462

```
Results for firm:      5
Technical efficiency = 0.571
Scale efficiency     = 0.363  (irs)
 PROJECTION SUMMARY:
  variable           original       radial        slack     projected
                        value     movement     movement         value
 output      1        878.860        0.000      581.140      1460.000
 input       1      15848.000    -6792.000        0.000      9056.000
 input       2      21900.000    -9385.714    -6126.286      6388.000
 LISTING OF PEERS:
  peer   lambda weight
    7      1.000
```

Figure4: Municipality 5 Efficiency Results

According to Figure 3, municipality 5 demonstrates a technical efficiency of 0.571 and a scale efficiency of 0.363. This indicates that it has the potential to save 42.9% (100% - 57.1%) of inputs through management improvements and 63.7% (100% - 36.3%)by minimizing its size. To enhance its efficiency, municipality 5 can seek guidance from municipality 7, which serves as a benchmark for comparison. The reduced input quantities required by municipality 5, in contrast to the original values, are presented in the last column.As an example, the initial value of "input1" was 15,848, and for "input2," it was 21,900. However, after projecting, the values for "input1" and "input2" became 9,056 and 6,388, respectively.

6 Conclusion:

This study aimed to assess the efficiency of MSW collection in all 23 municipalities of Sfax City using the DEA method. The analysis enabled the identification of efficiency and inefficiency sources, offering valuable managerial insights. For inefficient municipalities, peers were identified, and revised input quantities were determined. As a part of future work, we plan to extend this evaluation to assess the efficiency of municipalities in other cities across Tunisia.

References:

[1] N. K Avkiran. “Productivity analysis in the service sector with data envelopment analysis”. In: *Available at SSRN 2627576* (2006).

[2] H. Bal, H H. Örkcü, and S. Çelebioğlu. “Improving the discrimination power and weights dispersion in the data envelopment analysis”. In: *Computers & operations research* 37.1 (2010), pp. 99–107.

[3] Banker, R. D., Charnes, A., and Cooper, W. W. “Some models for estimating technical and scale inefficiencies in data envelopment analysis”. *Management science30* (1984), 1078–1092.

ISSN: 1737-933463

[4] D. S. Chang et al. “A novel approach for evaluating the risk of health care failure modes”. In: *Journal of medical systems* 36 (2012), pp. 3967–3974.

[5] Charnes, A., Cooper, W. W., and Rhodes, E. Measuring the efficiency of decision-making units. *European journal of operational research* 2 (1978), 429–444.

[6] S. De Jaeger et al. “Wasteful waste-reducing policies? The impact of waste reduction policy instruments on collection and processing costs of municipal solid waste”. In: *Waste Management* 31.7 (2011), pp. 1429–1440.

[7] Garc´ıa-Sanchez, I. M. “The performance of spanish solid waste collection”. *Waste Management & Research* 26 (2008), 327–336.

[8] C. Lo Storto. “Evaluating technical efficiency of Italian major municipalities: a Data Envelopment Analysis model”. In: *Procedia-Social and Behavioral Sciences* 81 (2013), pp. 346–350.

[9] Menikpura, S. N. M., et al. “Evaluation of the effect of recycling on sustainability of municipal solid waste management in Thailand”. *Waste and Biomass Valorization* 4 (2013): 237-257.

[10] H. Najadat, Q. Althebyan, and Y. Al-Omary. “Higher Education Units Assessment Based on Data Envelopment Analysis and Clustering Techniques”. In: *2019 International Arab Conference on Information Technology (ACIT).* IEEE. 2019, pp. 171–17.

[11] . Rogge and S. De Jaeger. “Evaluating the efficiency of municipalities in collecting and processing municipal solid waste: A shared input DEA-model”. In: *Waste management* 32.10 (2012), pp. 1968–1978.

[12] P. Rouse. “Data envelopment analysis in the public sector”. In: *Socio-economic planning sciences* 48 (2014), 2e3.

[13] IM G. Sánchez. “Efficiency of solid waste collection in Spain”. In: WIT *Transactions on Ecology and the Environment* 92 (2006).

[14] A. Sarra, M. Mazzocchitti, and A. Rapposelli. “Evaluating joint environmental and cost performance in municipal waste management systems through data envelopment analysis: Scale effects and policy implications”. In: *Ecological Indicators* 73 (2017), pp. 756–771.

[15] P. Simões, P. Carvalho, and R. C. Marques. “Performance assessment of refuse collection services using robust efficiency measures”. In: *Resources, Conservation and Recycling* 67 (2012), pp. 56–66.

[16] M. Struk et al. “The application of two-stage data envelopment analysis on municipal solid waste management in the Czech Republic”. 2016.

[17] Q. Yang et al. “Evaluating the efficiency of municipal solid waste management in China”. In: *International journal of environmental research and public health* 15.11 (2018), p. 2448.

ISSN: 1737-933464

Effect of Surfactants on double diffusive natural convection of CNT water-based micropolar nanofluids

Awatef Abidi[a,b,c], , NessrinManaa[b], Patrice Estellé[d], Mohammed NaceurBorjini[b]

[a] *Physics Department, College of Sciences Abha , King Khalid University, Saudi Arabia.*
[b] *Research Laboratory of Metrology and Energy Systems, National Engineering School, Energy Engineering Department, Monastir University , Monastir City, Tunisia.*
[d]*Higher school of Scienecs and Technology of Hammam Sousse, Sousse University, Tunisia.*
[d]*Univ Rennes, LGCGM, F-35000, Rennes, France.*
Email1 : abidiawatef@yahoo.fr
Email 2 : manaa_nessrin@outlook.com
Email3 : patrice.estelle@univ-rennes1.fr
Email 4 : borjinimn@yahoo.com

Abstract :**The present study deals withthe influence of surfactants which are one of the most important factors affecting the process of energy transport during the preparation ofnanofluids. In fact, these additives modify the transport properties of nanofluids such as viscosity and thermal conductivity. This highlights the modeling and study of the impact of surfactant on heat and mass transfer rates in a cubic cavity containing a micropolar nanofluid. The objective of this work is therefore to perform an analysis of the three-dimensional natural convection with double diffusion in the multi-walled CNT/water micropolar nanofluid stabilized with two types of surfactants "lignin" and "sodium polycarboxylate". We have discussed the effects of surfactants used to stabilize the micropolar nanofluid, the microrotation parameter, the nanoparticle volume fraction, the buoyancy ratio, and the Rayleigh number on heat and mass transfer rates and flow behavior.**

I. INTRODUCTION

Utilizing nanofluid is one of the new methods for conservation energy during natural convection. These fluids are manufactured by the dispersion of nanoparticles in conventional heat transfer fluids.It exists many types of nanoparticles used in nanofluids that differ in nature, such as metallic (Al, Cu, Ag...), oxide (Al_2O_3, TiO_2, CuO…) and carbon-based materials.

Putra et al. [1] investigated experimentally the natural convection of nanofluid in a horizontal cylinder filled with two types of nanoparticles CuO and Al_2O_3. They obtained a decrease in heat transfer rate with the enhancement in nanoparticles' concentrations. Khanafer et al. [2] carried out a numerical investigation on natural convection with Cu nanofluid and noticed heat transfer increase with an increase in nanoparticles' volume fraction. Enhancement in heat transfer was shown to be more efficient with nanofluid than with pure fluid. Abu Nada et al. [3] carried out numerical investigations considering different nanofluids based on Al_2O_3, TiO_2, Cu and Ag, in horizontal annuli. They reported the dependence of heat transfer performance following the type of nanofluid used.

Among all nanoparticles available for producing nanofluids, carbon nanotubes (CNT) are more recommending than other traditional nanoparticles because of their relatively low density and very high thermal conductivity.Wen and Ding [4] studied the effective thermal conductivity of aqueous suspensions of MWCNTs.They used the sodium polycarboxylate as surfactant to stabilize the nanofluids. They obtained an enhancement of thermal conductivity when the nanoparticles volume concentrationincreases, and the dependence was nonlinear even at very low concentrations. They founded

ISSN: 1737-933465

that an enhancement in temperature increases the effective thermal conductivity of nanofluid. A study of the effect of lignin as surfactant on viscosity and thermal conductivity of CNT/water-based nanofluids was investigated by Estellé et al. [5]. They compared the effect of lignin on the viscosity and thermal conductivity of CNT/water nanofluid with the effect of sodium polycarboxylate. They noticed that the thermal conductivity of nanofluid increase with the nanoparticles volume concentration. Estellé et al. [6] investigated theoreticallythe natural convection in a square cavity partially heated filled with CNT water-based nanofluids. They analyzed the effect of the average temperature and the nanoparticles volume fraction, driving temperature between hot and cold walls and role of surfactant. They founded that the Nusselt number of nanofluids is decreased with the increase of the volume fraction of nanofluid, which is related to non-Newtonian behavior of nanofluids.

The theory of Enrigen [7] can be used to elucidate fluid particles' micro-motions which cannot be explained by the classical models. In fact, physically, fluid particles may expand, contract, rotate about their own axis or may even change their shape due to the shear stress applied on them. So, the micropolar fluid theory can be valuable to explore fluid behavior of polymer fluids, solidification of liquid crystals, cooling of a metallic plate in a bath, exotic lubricants, colloidal systems, and biological fluids, for which the theory of Navier–Stokes is inadequate to describe the impacts of the microstructures on fluid motion.

The rotating micro-constituents 'effects in nanofluids should be judiciously exploited to understand the behavior of fluid flow effectively. Abidi et al. [8] carried out the 3D numerical simulation of both heat and mass transfer rates and fluid flow in a cubic cavity filled with an Al_2O_3/water micropolar fluid. The simulations are conducted under a uniform magnetic field. The results reveal that heat and mass transfer rates and three-dimensional characters of the flow are weaker when the micropolar nanofluid model was used compared to the pure nanofluid model. Manaa et al. [9] investigated the thermo-solutal natural convection of a micropolar nanofluid filled 3D enclosure with different types of nanoparticles (Al_2O_3, TiO_2, Cu and Ag) considering the effect of relevant parameters on heat and mass transfer characteristics. They obtained that both heat and mass transfer rates and the three-dimensional character of the flow for the micropolar nanofluid model are smaller compared with that of a pure nanofluid model. Their results show that the rates of heat and mass transfer decrease with an enhancement in micropolar parameter as well as nanoparticlesvolume fractions.The main aim of thisworkis to perform a computation analysis on the three-dimensional double-diffusive natural convection in multi-walled CNT/water micropolar nanofluid stabilized with two types of surfactants lignin and sodium polycarboxylate. In this work, experimental thermophysical properties determined in previous works were used. The effect of the type of used surfactant to stabilize the micropolar nanofluid, micropolar parameter, nanoparticles' volume fraction, buoyancy ratio, and the Rayleigh number on heat and mass transfer rates and flow behavior are meticulously elucidated.

II. MATHEMATICAL MODELING

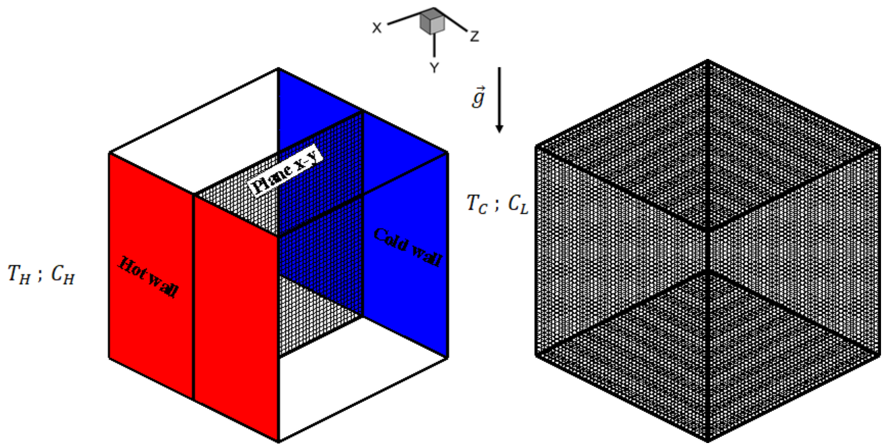

(a) **(b)**

Fig.1 (a) Schematic of the considered problem, **(b)** Mesh surfaces

A simple schematic view of the thermo-solutal natural convection problem under study is described inFig. 1. The cube is filled with multi-walled CNT water-based micropolar nanofluid stabilized with two types of surfactants lignin and sodium polycarboxylate respectively. The two vertical walls parallel to the plane (y-z) are subject to constant temperatures ($T_H>T_C$) and constant concentrations ($C_H>C_L$). The other walls are supposed to be impermeable and adiabatic. The dynamic and thermal slips between nanoparticles and the base fluid are negligible. During the process of the natural convection, all the properties of the base fluid and nanoparticles are unchangeable except the density in the buoyancy term in momentum equation, its variations being modeled using Boussinesq approximation. The effects of Soret and Dufour are assumed to be negligible.

The vorticity–vector potential formulation is used in the present study to eliminate the pressure term and makes easier the numerical treatment. The vorticity and vector potential are respectively defined by the following two relations: $\vec{U} = \nabla \times \vec{\psi}$and $\vec{\omega} = \nabla \times \vec{U}$.

The system of governing equationsof the phenomenonis:

$$\nabla^2 \vec{\psi} = -\vec{\omega} \tag{7}$$

$$\frac{\partial \vec{\omega}}{\partial t} + (\vec{U}.\nabla)\vec{\omega} - (\vec{\omega}.\nabla)\vec{U} = Pr\left(\frac{\mu_{nf}}{\mu_f} + K\right)\left(\frac{\rho_f}{\rho_{nf}}\right)\nabla^2\vec{\omega} - PrK\left(\frac{\rho_f}{\rho_{nf}}\right)\nabla^2\vec{H}$$
$$+RaPr\left(\frac{(\rho\beta_T)_{nf}}{(\rho\beta_T)_f}\right)\left(\frac{\rho_f}{\rho_{nf}}\right)\left(\left[\frac{\partial T}{\partial z}, 0, -\frac{\partial T}{\partial x}\right] - N\left[\frac{\partial C}{\partial z}, 0, -\frac{\partial C}{\partial x}\right]\right) \tag{8}$$

$$\left(\frac{\partial \vec{H}}{\partial t} + (\vec{U}.\nabla)\vec{H}\right) = Pr\left(\frac{\mu_{nf}}{\mu_f} + \frac{K}{2}\right)\left(\frac{\rho_f}{\rho_{nf}}\right)\nabla^2\vec{H} + PrK\left(\frac{\rho_f}{\rho_{nf}}\right)(\vec{\omega} - 2\vec{H}) \tag{9}$$

$$\frac{\partial T}{\partial t} + (\vec{U}.\nabla)T = \left(\frac{(\rho C_P)_f}{(\rho C_P)_{nf}}\right)\left(\frac{k_{nf}}{k_f}\right)\nabla^2 T \tag{10}$$

$$\frac{\partial C}{\partial t} + (\vec{U}.\nabla)C = \frac{1}{Le}\left(\frac{(\rho C_P)_{nf}}{(\rho C_P)_f}\right)\left(\frac{k_f}{k_{nf}}\right)\nabla^2 C \tag{11}$$

The local Nusselt and Sherwood numbers on the isothermal walls are defined by:

$$Nu = \left.\frac{k_{nf}\frac{\partial T^F}{\partial x^F}}{k_f\frac{T^F_H - T^F_C}{L}}\right)_{x^F=0,1} = -\left.\frac{k_{nf}}{k_f}\frac{\partial T}{\partial x}\right)_{x=0,1} \tag{12}$$

$$Sh = \left.\frac{D\frac{\partial C^F}{\partial x^F}}{D\frac{C^F_H - C^F_L}{L}}\right)_{x^F=0,1} = \left.\frac{\partial C}{\partial x}\right)_{x=0,1} \tag{13}$$

The average Nusselt and Sherwoood numbers, on the isothermal walls of the enclosure are defined as follows:

$$\overline{Nu} = \int_0^1\int_0^1 Nu\,\partial y\,\partial z \tag{14}$$

$$\overline{Sh} = \int_0^1\int_0^1 Sh\,\partial y\,\partial z \tag{15}$$

For each time step, the following convergence criterionissatisfied:

$$\sum_{1,2,3} \frac{\max|\psi^n - \psi^{n+1}|}{\max|\psi^n|} + \max|T^n - T^{n+1}| + \max|C^n - C^{n+1}| \leq 10^{-5} \tag{16}$$

III. RESULTS AND DISCUSSION:

For comparison purpose with nanofluids, water which is the base fluid of nanofluids was takenas a reference. The thermo-physical properties of water used for the simulations are reported in [1].
In this study, it is considered carbon nanotubes with density of 1800 kg m^{-3} and purity of 90% and 9.2 nm and 1.5 µm in average diameter and length, respectively, dispersed in a mixture of water and surfactant. To improve the dispersion and stability of multi-walled CNT within water and to reduce clogging and the sedimentation with time, it was used two types of surfactants lignin and sodium polycarboxylate. The preparation of nanofluid was reported in [5, 6, 11]. The volume fraction of carbon nanotubes under consideration ranges from 0.0055 to 0.557%. Density, thermal conductivity, viscosity at 20°C were experimentally determined in [5, 6, 11] from well-designed procedures while heat capacity was theoretically determined neglecting heat capacity of surfactants. All these results are shown in Fig. 2and used in the present numerical simulations.

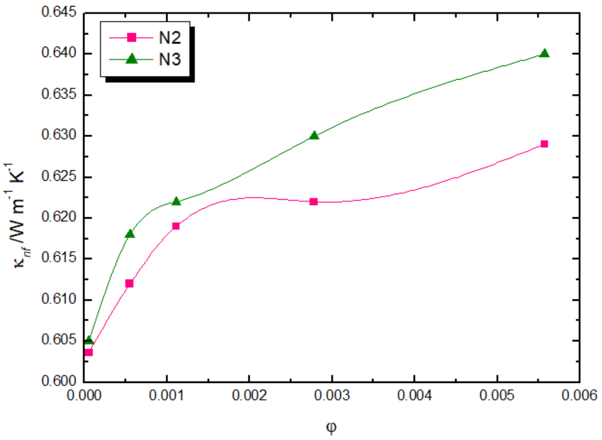

(a)

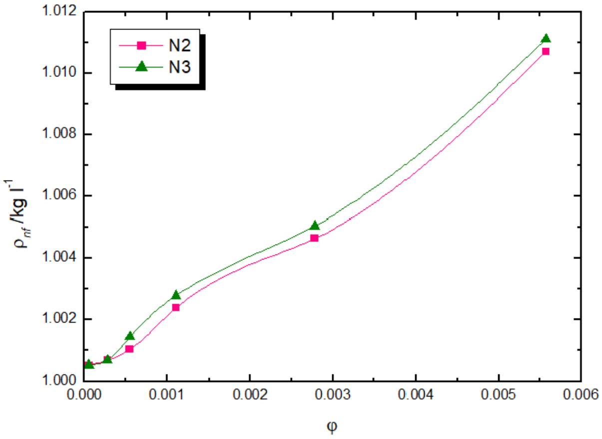

(b)

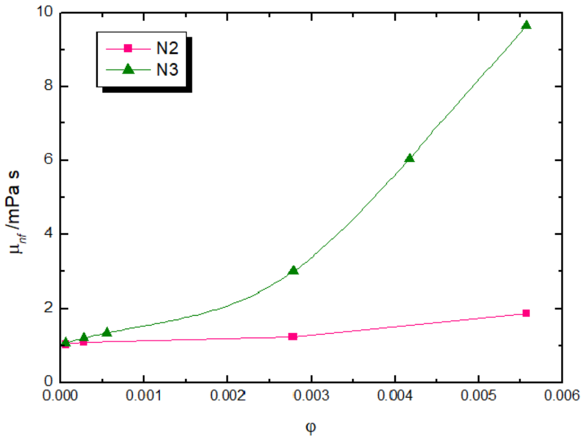

(c)

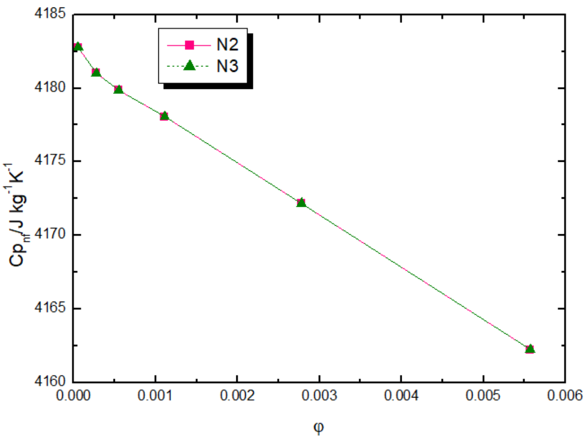

(d)

ISSN: 1737-933468

Fig. 2 Thermophysical properties of CNT nanofluids at 20°C with two types of surfactants: **(a)** thermal conductivity, **(b)** density, **(c)** dynamic viscosity and **(d)** heat capacity

Figure 3shows the variations of maximum transverse velocity with the nanoparticle's volume fraction for micropolar/non-micropolar nanofluid stabilized with Lignin (N2) and sodium polycarboxylate (N3). Thus, the effects of nanoparticles' volume fraction on the three-dimensional flow are explored. This figure shows, irrespective of the model used,that the maximum transverse velocity is improved by increasing φ to the critical value then the velocity tends to decrease. Also, it is clearly noted that N2 have higher transverse velocity compared to N3. For example, for φ=0.0055% it exists a 27.63 % difference between the two cases. In addition, it isinteresting to note that the non-micropolar nanofluid (*K=0*) has the highest maximum transverse velocity compared to the micropolar nanofluids (*K*≠0) for all the considered values of nanoparticles volume fraction.

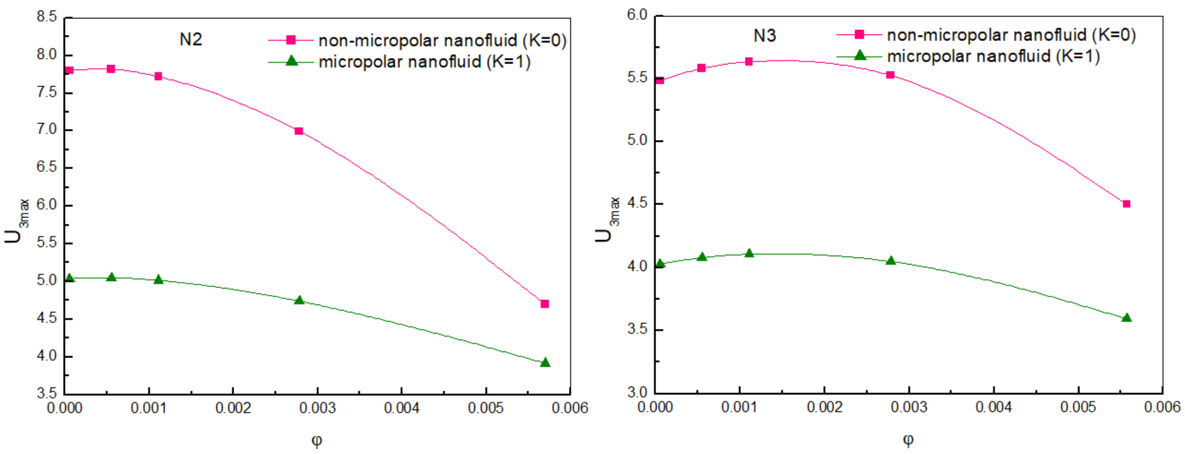

Fig. 3: Variation of maximum of transversal velocity U_{3max} according to the nanoparticles volume fraction for N2 and N3 micropolar/non-micropolar nanofluid for $Ra=10^5$ and $N=-0.2$.

Figure 4 shows the variations of average Nusselt number $\overline{Nu}$ and Sherwood number $\overline{Sh}$ with nanoparticles' volume fraction for micropolar/non-micropolar nanofluid stabilized with Lignin (N2) and sodium polycarboxylate (N3). Irrespective to the considered type of nanofluids, $\overline{Nu}$ and $\overline{Sh}$ are lower when the micropolar nanofluid model is under consideration, and are increased when the non-micropolar fluid model is under consideration irrespective of the values of nanoparticles volume fraction. It is noticed that for the two types of surfactants used, the average Nusselt and Sherwood numbers increase in the area where the value of the volume fraction of nanoparticles is less than its critical value. This is because the thermal performance of water solution is improved by the addition of nanoparticles. Afterwards, the heat and mass transfer rates decrease in the area where the value of the nanoparticles volume fraction is greater than its critical value due to the predominant influence of viscosity over thermal properties. It can be seen also from Fig.3, for the case where the surfactant lignin is used, the average Nusselt and Sherwood numbers are greater than in the case of the surfactant sodium polycarboxylate is employed.

ISSN: 1737-933469

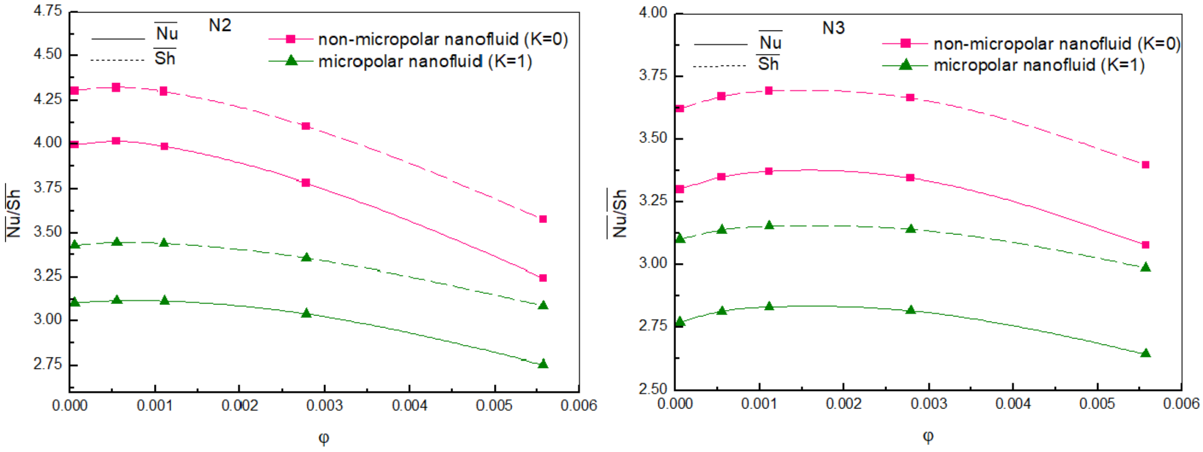

Fig. 4: Variation of $\overline{Nu}$ and $\overline{Sh}$ on the hot wall with nanoparticles volume fraction for both micropolar and non-micropolar N2/N3 nanofluid models for $Ra=10^5$ and $N=-0.2$.

IV. CONCLUSION:

It is observed that the heat and mass transfer rates are lower for a micropolar nanofluid model when compared to the pure nanofluid model. In fact, the enhancement of micropolar parameter results a decrease of average Nusselt and Sherwood numbers. The use of lignin as a surfactant ameliorates heat and mass transfer rate and nanofluid flow better than the use of sodium polycarboxylate as a surfactant. The nanoparticles volume fraction can be used as a control element for heat rate and fluid flow. Thus, for a nanoparticles volume concentration less than the critical value, the flow intensity is ameliorated and is deteriorated when it exceeds this value.

REFERENCES :

[1] Putra N, Roetzel W, Das SK. Natural convection of nano-fluids.Heat Mass Transf. 2002; 39:775-784.

[2] Khanafer K, Vafai K, Lightstone M. Buoyancy-driven heat transfer enhancement in a two-dimensional enclosure utilizing nanofluids. Int J Heat Mass Trans. 2003; 46: 3639–3653.

[3] Abu-Nada E, Masoud Z, Hijazi A. Natural convection heat transfer enhancement in horizontal concentric annuli using nanofluids. IntComm Heat Mass Transf. 2008; 35: 657–665.

[4] Wen D, Ding Y. Effective thermal conductivity of aqueous suspensions of carbon nanotubes (carbon nanotube nanofluids). J Thermal Heat Transf. 2004; 18: 481-485.

[5] Estellé P, Halelfadl S, Maré T. Lignin as dispersant for water-based carbon nanotubes nanofluids:Impact on viscosity and thermal conductivity. Int Com Heat Mass Transf. 2014; 57: 8-12.

[6] Estellé P, Mahian O, Maré T, Öztop HF. Natural convection of CNT water-based nanofluids in a differentially heated square cavity. J Thermal Anal Calorim. 2017; 28: 1765–1770.

[7] Eringen AC. Theory of micropolar fluids, J MathMech. 1966; 16: 1–18.

[8] Abidi A, Raizah Z, Madiouli J. Magnetic Field Effect on the Double Diffusive Natural Convection in Three-Dimensional Cavity Filled with Micropolar Nanofluid. App Sci. 2018; 8: 2342–2367.

Manaa N, Abidi A, Saleel CA, Al Makwash SM, Borjini MN. On Simulation of Double-Diffusive Natural Convection in a Micropolar Nanofluid Filled Cubic Cavity. Heat Transf Eng. 2020;https://doi.org/10.1080/01457632.2020.1756074.

[9] Therme-Excel: Physical characteristics of water at the atmospheric pressure. Last update: 2003.http://www.thermexcel.com/english/tables/eau_atm.htm.

[10] Estellé P, Halelfadl S, Maré T. Thermal conductivity of CNT water based nanofluids: Experimental trends and models overview. J Thermal Eng. 2015; 1: 381-390

Conférence Internationale sur les Sciences Appliquées et l'Innovation (CISAI-2023)
Proceedings of Engineering & Technology-PET-Vol 77

Vortex characteristics of two rotating immiscible fluids

Kenza Brahma*[1], Rachid Saci[2], Kacem Mansouri[3]

*[1]*Mechanical Engineering Department, Energy and Mechanical Engineering Laboratory, Boumerdes University Frantz fanon City, Boumerdes, Algeria*

[2]*Physics Department, Boumerdes University*

[3]*Mechanical Engineering Department, Boumerdes University*

*k.brahma@univ-boumerdes.dz
r.saci@univ-boumerdes.dz
manskac@yahoo.fr

Abstract

Hydrodynamic and behavior of laminar confined axisymmetric flows driven by the rotating top disk in cylindrical cavity have been studied numerically. The vertical cavity, is filled with two superposed immiscible incompressible fluids. The top more viscous liquid drives the lower heavier fluid via the interface shear. The study, identified and highlighted a flow topology of types of axisymmetric recirculation regions; depending upon the effects of the disk rotation rate. This work confirms partly previous experimental observations and provides additional quantitative findings; particularly in the vicinity of the interface. The findings are in good accord with the experiments and show that vortex size increases with increasing rotation rate. The basic flow is made up of two clockwise circulation cells, separated by a thin layer of anticlockwise circulation (TCL). The gap thickness of TCL decreases with increasing rotation rate however, the interface high increases as rotation rate increases

Introduction:

The vortex breakdown phenomenon may be observed in several industrial applications involving rotating fluid flows (bioreactors, hydro-cyclones, chemical reactors etc) as well as in the natural environment (atmospheric vortices, hurricanes, tornadoes etc). The physical mechanisms of this structure are still not fully highlighted; which motivated numerous attempts to develop strategies to control the conditions of its onset and development [1], [2], [3]. Unlike the case of a single fluid configuration, relatively few studies were devoted to the conditions of occurrence and development of the vortex breakdown within two a layer of two immiscible rotating fluids [4], [5]. In this context, the present work explores numerically means of controlling the vortex pattern which develops in a vertical cylinder under differential rotation of its boundaries.

Physical problem:

A schematic description of confined axisymmetric flow considered in the present work is reported in Fig. 1. The physical problem consists of a cylindrical cavity filled with “glycerin-water mixture”of density $\rho_g = 1208\ kg/m^3$ and kinematic viscosity$u_g = 42.82 \times 10^{-6} m^2/s$ till h_g. The sunflower oil is of density$\rho_o = 920\ kg/m^3$ and viscosity $u_o = 54.86 \times 10^{-6} m^2$/s The

ISSN: 1737-933471

surface tension at theinterface is σ = 0.0315 N/m [5].The radius of the cylindrical cavity is 0.045m while the height is 0.1125m.The aspect ratio of the cylinder is fixed at Ah=H/R=2.5.

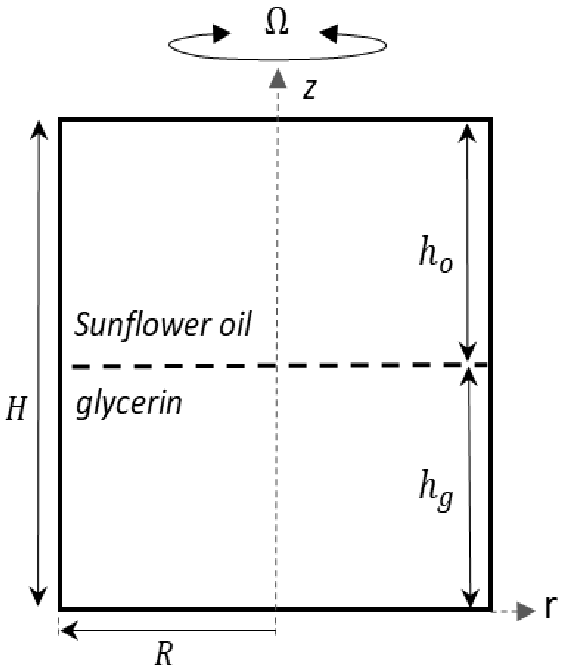

Fig. 1Schematic of the model flows under consideration

The flow is driven by the top part with constant angular velocity **Ω**. Thenon-dimensional numbers which govern the problem is Reynolds number $Re = \Omega R^2/\nu_o$Here, subscripts "o" and "g" denote oil and glycerin respectively.

Results:

The induced flow topology is mainly presented in terms of streamlines and circulation zones for Reynolds number Re = 900 (Fig.2 (a)). In order to confirm the numerical method, our results were partly validated by comparing the mean axial velocity distribution against experimental measurement (Fig.2 (b)).

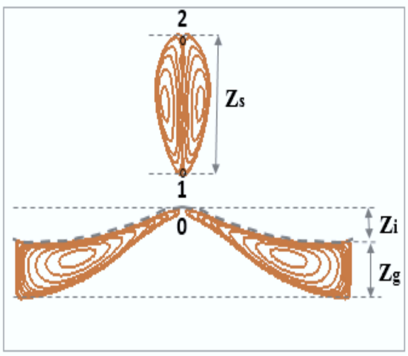

(a)

ISSN: 1737-933472

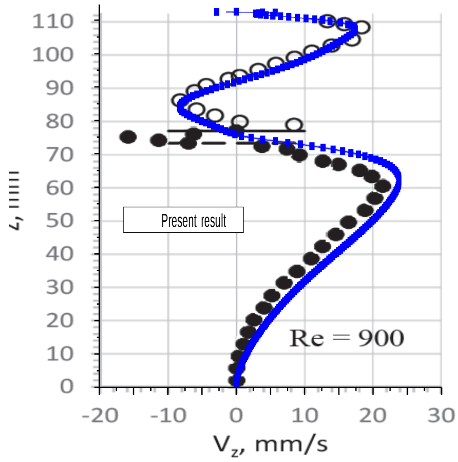

(b)

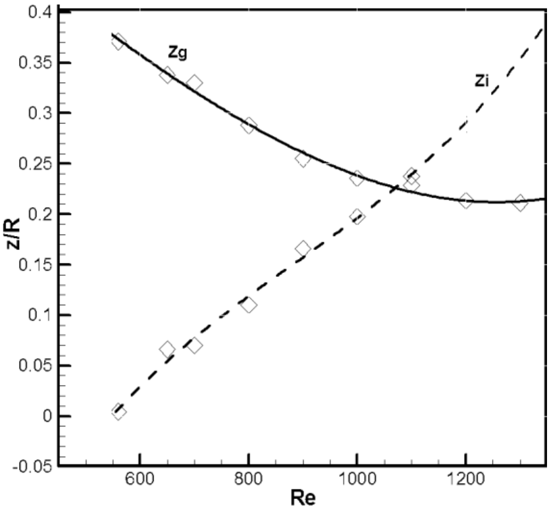

(c)

Fig. 2(a) schematic of selected vortex and associated thin circulation layer characteristics, (b) comparison of the mean axial velocity with experiments (black and withe circles), (c) dependence of interface height and gap width on the rotation rate

The top more viscous liquid drives the lower heavier fluid viathe interface shear.The basic flow is made up of two clockwise circulationcells, separated by a thin layer of anticlockwise circulation (TCL) and Vortex Breakdown Bubble (VBB) occurs in the oil flow, as Re increases.

The vortex types and characteristics, are identified and analyzed. The gap thickness of TCLdecreases with increasing rotation rate however, the interface high increases as rotation rate increases (Fig.2 (b)).

The effect of Reynolds number on VVB size is also well illustrated in Fig.3which is in good accord of experimental finding of [5]

ISSN: 1737-933473

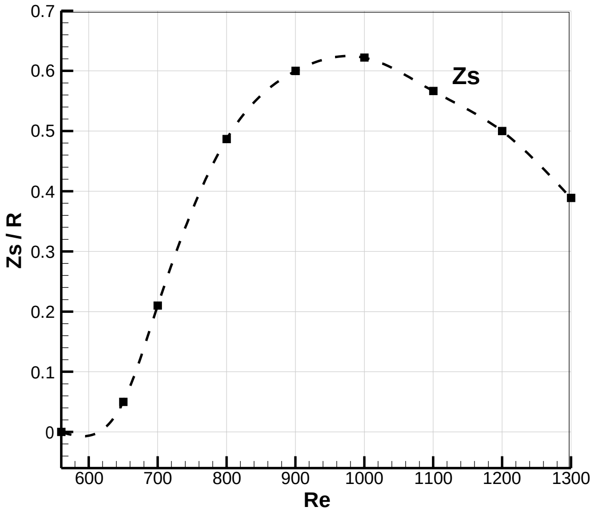

Fig. 3 Dependence of VBB size on Reynolds number

Conclusion:

The swirling axisymmetric laminar flow of two fluids has been numerically investigated.the TCL has been detectedby numerical simulations, because it has not been experimentally observed.This work compliments and confirm previous prediction of[5].

The study of vortex flows characteristics is relevant for both industrial and natural applications, in particular, this type of flow can provide efficient mixing in aerial vortex bioreactors for tissue growth in chemical applications.

References:

[1] Escudier, M. (1988). Vortex breakdown: observations and explanations. Progress in Aerospace Sciences, 25(2), 189-229.

[2] Fujimura, K., Yoshizawa, H., Iwatsu, R., Koyama, H. S., & Hyun, J. M. (2001). Velocity measurements of vortex breakdown in an enclosed cylinder. J. Fluids Eng., 123(3), 604-611.

[3] Fekhar, M., Rachid, S. A. C. I., & Gatignol, R. (2021). Swirling Flows Characteristics in a Cylinder Under Effect of Buoyancy. Mechanics, 27(3), 201-208.

[4] Naumov, I. V., Sharifullin, B. R., Tsoy, M. A., & Shtern, V. N. (2020). Dual vortex breakdown in a two-fluid confined flow. Physics of Fluids, 32(6), 061706.

[5] Naumov, I. V., Glavny, V. G., Sharifullin, B. R., & Shtern, V. N. (2019). Formation of a thin circulation layer in a two-fluid rotating flow. Physical Review Fluids, 4(5), 054702.

ISSN: 1737-933474

Recent Trends in Signal Processing

Tamrabet Chaima[#1], Hadjadj Aoul Elias[*2], Dekhmouche Med Tahar[#3]

[#]*Department of Electromechanical, Badji Moukhtar- Annaba, Algeria*

Email 1 – chaima.tamrabet@univ-annaba.org
Email 2 - Hadjadj.elias@yahoo.fr
Email 3 - dekhmouchemed@gmail.com

Abstract:

Using signal processing techniques for fault diagnosis of rotating machines become increasingly important. Advanced digital technology started to accelerate the theoretical signal processing techniques over academia. Despite this interest, no one to the best of our knowledge studied so deeply the possibility of making all of these innovations feasible on real or not. The aim of our work is the theory understanding and verification of basic signal processing techniques for practical problems such as bearings faults with the help of MATLAB. FFT, EMD, and HT are done in order to extract features from signals for fault detection and identification with the help of MATLAB code. These tests reveal that strong evidence of FFT is found on filtering signals based on the frequency information. EMD also reflected as a self-adaptive and an automatic filter. Finally, Hilbert transform extract time-frequency domain features from the IMFs.

Keywords— signal processing, bearing diagnosis, fast fourier transform, empirical mode decomposition, Hilbert transform

Introduction:

In recent years, signal processing has many applications in the field of machine condition monitoring and diagnosis of typical rotating machine. Being one of the most fragile elements of rotating machinery, rolling bearings are a must-have.

In the literature, there are a surprising number of examples showing the application of signal processing for bearing fault detection. In particular, combining decomposition-based methods with traditional or artificial intelligence-based methods. Singh et al. have been proved that by adding white noise to EMD, the mode mixing problem can be removed and got a signal with effectively reduced noise [1]. Sher et al. conducted a satisfying hybrid signal processing approach for fault diagnosis of bearing using discrete wavelet transform (DWT), empirical mode decomposition (EMD), and One-way ANOVA and Kruskal Wallis in MATLAB for feature extraction and selection. DWT is used to split the raw vibration signal into certain frequency sub-bands, and EMD is used to decompose the selected frequency band into a number of intrinsic mode functions (IMFs) and a residue. Finally compared to SVM and ANN. The results were quite satisfying [2]. Another research that proved an effective approach for bearing monitoring, based on (EMD) and the Hilbert transform (HT). The proposed approach using EMD to extract the temporal components of oscillating vibration signals called intrinsic mode functions (IMFs). Combined

ISSN: 1737-933475

with the HT, the EMD allows an estimate of the instantaneous frequency of each IMF. The Hilbert marginal spectrum density is then extracted as a health indicator in order to detect and diagnose the degradation of bearings. This approach was validated on two test benches with variable speeds and loads [3]. Weng et al. have been combining time-varying filtered empirical modal decomposition and the singular value decomposition (TVF-EMD-SVD) with deep belief neural network show that the fault identification of rolling bearing reaches more than 95 % [4]. C. Zhou et al. have been proposed a parameter-adaptive time-varying filtering empirical mode decomposition (TVF-EMD) feature extraction method based on the improved grasshopper optimization algorithm (IGOA), In order to separate the sub-signals and extract the feature frequency in the signal accurately. At last, the result was Compared with ensemble empirical mode decomposition (EEMD), variational mode decomposition (VMD), TVF-EMD-GOA have been achieved high performance [5]. Faysal et al. have been applied empirical mode decomposition (EMD) to the raw vibration signal. Intrinsic mode function (IMF) containing the characteristics of vibration data was analysed to obtain 90 statistical features. principal components analysis (PCA) and binary particle swarm optimiser (BPSO) were applied individually for feature reduction. The reduced feature subsets were 12 and 35 for PCA and BPSO, respectively. -NN was applied to the entire feature set and individually on the selected feature subset of PCA and BPSO. The reduced feature subset with PCA performed the finest in all the measurements taken [6].

After reviewing the literature, it can be concluded that there is always some error associated with the results when working with a single domain analysis. So, in this work, a hybrid of Empirical Mode Decomposition (EMD), Hilbert Transform (HT) and condition indicators (kurtosis, mean…) are used to collect and analyze features imbedded in the data provided by the case Western Reserve University Bearing Data Center Website (CWRU).

Signal processing techniques using MATLAB:

Methods and Results:

Signal processing techniques are widely used to improve the effectiveness of fault detection and identification approaches. Signal processing techniques extract the hidden properties of the signal using various analyses, such as time-domain analysis, frequency-domain analysis, and time–frequency analysis.[7, p. 5]

I. Data acquisition:

The case Western Reserve University Bearing Data Center Website:

https://engineering.case.edu/bearingdatacenter

II. Feature extraction:

- ✓ **Time-domain:**

ISSN: 1737-933476

a. Kurtosis:

Figure 1. representes signal processing in the time domain, no useful information about the state of the bearing.In order to quantify the infromation contained in the signal. The use of certain statistical indicator (RMS, mean, variance, kurtosis,…etc) could provide a precise information about the state.As mentioned in [3]. For bearing that operates in normal state, the value of kurtosis is close to 3 and increases dramatically as soon as pulses occur due to defect.

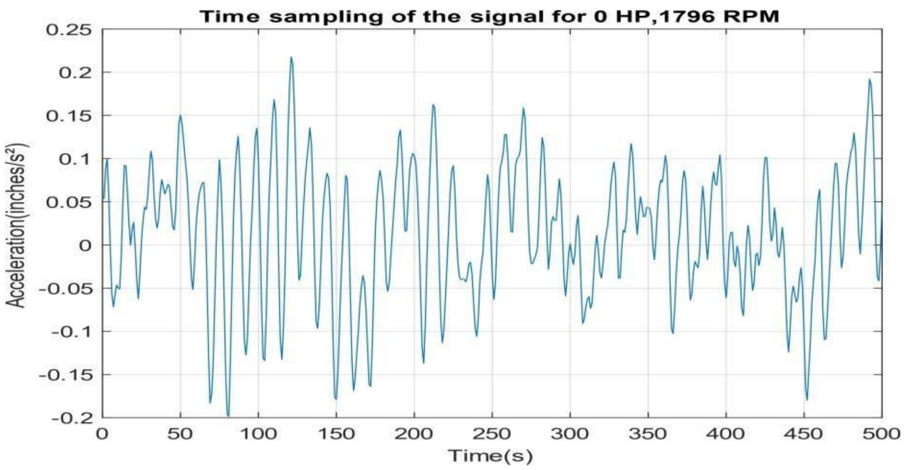

Figure1. Time sampling of healthy rolling bearing for 0 HP, 1796 RPM

By using MATLAB we get the following results:

- **a)** The Kurtosis value for healthy state (0HP, 1796 RPM) is: **2.7642**
- **b)** The Kurtosis value for abnormal state (inner race, fault depth 0.007, 0HP, 1796 RPM) is: **6.0272**
- **c)** The Kurtosis value for abnormal state (inner race, fault depth 0.021, 0HP, 1796 RPM) is: **4.1681**

The result indicates the existance of fault by using the statistical quantity kurtosis.

b. Other condition indicators:

The following statistical indicators (min, max, mean, median, peak to peak, RMS) obtained by Signal Analyzer application on MATLAB, provide a precise information about the state. The value increases dramatically for each indicator due to the existence of defect.

Name	Line	ROI - Min	ROI - Max	Min - Value	Min - Time	Max - Value	Max - Time	Mean	Median	Peak to P...	RMS
X097_DE...		0	243937	-2.8664e-01	28964	3.1125e-01	49841	1.2558e-02	1.2517e-02	5.9789e-01	7.3764e-02

ISSN: 1737-933477

Name	Line	ROI - Min	ROI - Max	Min - Value	Min - Time	Max - Value	Max - Time	Mean	Median	Peak to P...	RMS
X213_DE...		0	244338	-3.0276e+00	147895	3.0750e+00	147848	1.1167e-02	9.3877e-03	6.1026e+00	5.8507e-01

✓ **Frequency-domain: Fast Fourier Transform:**

Table 1. Defect frequencies**:** (multiple of running speed **in Hz**). [8]

Inner Ring	**Outer Ring**	**Cage Train**	**Rolling Element**
5.4152	3.5848	0.39828	4.7135

For: F_r 0HP (1796 RPM) → $=\frac{1796}{60}=$**29.93 Hz**

BPFI=5.4152*F_r= 5.4152*29.93≈ **162.0769 Hz.**

2BPFI=324.15 Hz.

3BPFI=486.23 Hz.

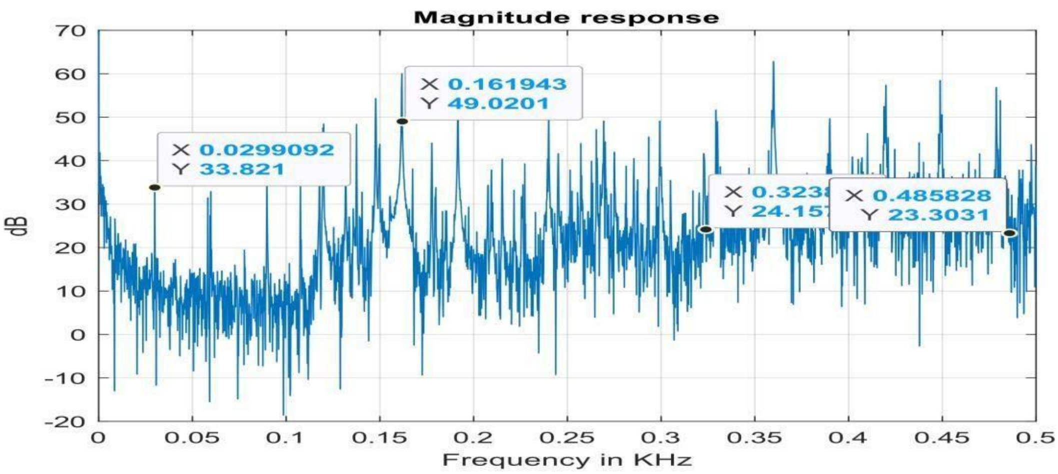

Figure2. Frequency sampling of healthy rolling bearing for 0 HP, 1796 RPM.

ISSN: 1737-933478

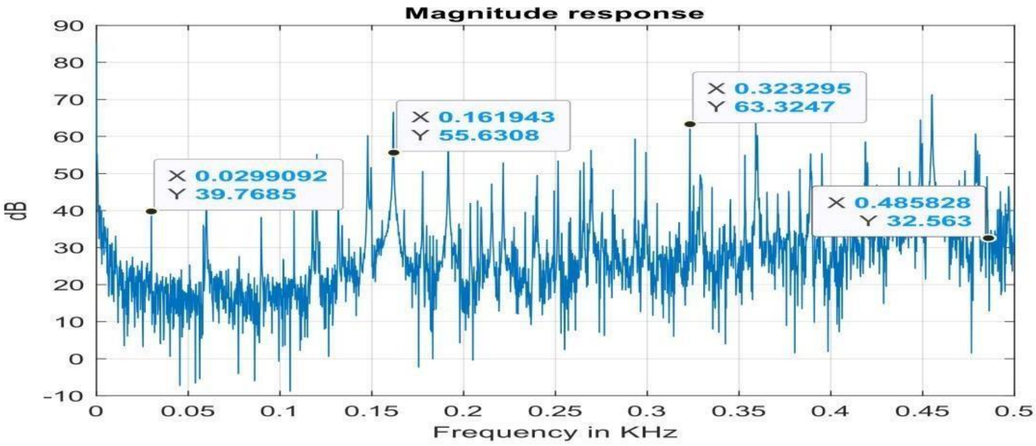

Figure3. Frequency sampling of faulty inner race for 0.007 in depth, 0 HP, 1796 RPM.

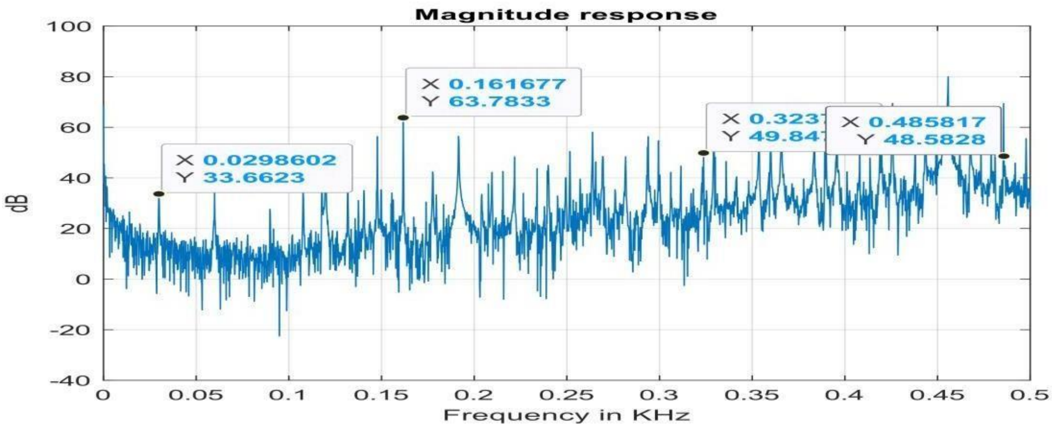

Figure 4. Frequency sampling of faulty inner race for 0.021 in depth, 0 HP, 1796 RPM.

We can notice from figures (figure 2-4), that the acceleration exceeded at the fault frequency characteristic for bearing with 0.021 in depth more than the bearing with 0.007. So, the existence of the fault effects the magnitude at the peak of inner fault frequency and its harmonics, 2BPFI, 3BPFI, …etc. In addition, there was no visible periodicity between the acceleration peaks giving an indication of its fault frequency. Which implies further analysis.

✓Emperical Mode Decomposition for feature extraction:

As we mentioned before, our approach was based on filtering the vibration signals around the characteristic frequencies. Knowing that the signal of the bearing contains sinusoidal waves with different amplitude and frequency values. For such nonstationary signals, EMD approach is used by dividing the signal into intrinsic mode functions (IMF), that helps in finding crucial machine failure data for processing purposes. Sifting is the process of breaking down a signal into an IMF function. According to frequency, the EMD approach ranks the IMF from highest to lowest.

In order to determine the intrinsic mode functions (IMFs), we performed an empirical mode decomposition to the healthy and defective bearing signals using MATLAB. The table generated in the command window indicates the number of sifting iterations, the relative tolerance, and the sift stop criterion for each generated IMF.

Command Window

```
>> EMDMACHINELEARNING
```

Current IMF	#Sift Iter	Relative Tol	Stop Criterion Hit
1	2	0.025071	SiftMaxRelativeTolerance
2	2	0.11424	SiftMaxRelativeTolerance
3	2	0.075746	SiftMaxRelativeTolerance
4	2	0.033861	SiftMaxRelativeTolerance
5	2	0.019684	SiftMaxRelativeTolerance
6	2	0.0291	SiftMaxRelativeTolerance
7	2	0.030946	SiftMaxRelativeTolerance
8	2	0.07239	SiftMaxRelativeTolerance
9	2	0.1047	SiftMaxRelativeTolerance
10	2	0.037319	SiftMaxRelativeTolerance

```
Decomposition stopped because maximum number of intrinsic mode functions was extracted.
fx >>
```

Table 2. The number of sift iterations, the relative tolerance, and the sift stop criterion for each generated IMF for the healthy bearing (0HP,1796 RPM).

Command Window

```
>> EMDMACHINELEARNING
```

Current IMF	#Sift Iter	Relative Tol	Stop Criterion Hit
1	1	0.056914	SiftMaxRelativeTolerance
2	2	0.081968	SiftMaxRelativeTolerance
3	1	0.14509	SiftMaxRelativeTolerance
4	2	0.028836	SiftMaxRelativeTolerance
5	2	0.08935	SiftMaxRelativeTolerance
6	2	0.033731	SiftMaxRelativeTolerance
7	2	0.0114	SiftMaxRelativeTolerance
8	2	0.19623	SiftMaxRelativeTolerance
9	2	0.032256	SiftMaxRelativeTolerance
10	2	0.014136	SiftMaxRelativeTolerance

```
Decomposition stopped because maximum number of intrinsic mode functions was extracted.
fx >>
```

Table 3. The number of sift iterations, the relative tolerance, and the sift stop criterion for each generated IMF of inner race faulty bearing with 0.021 in depth (0HP,17976 RPM).

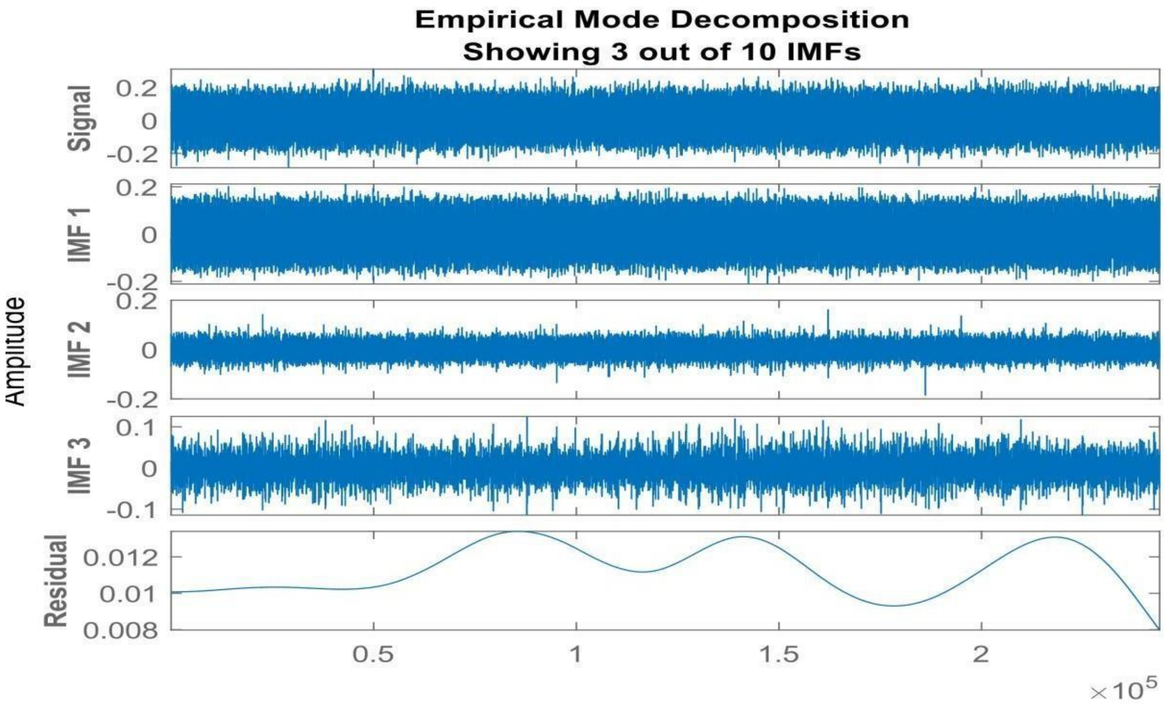

Figure 5. EMD of the healthy bearing 0HP, 1796RPM.

ISSN: 1737-933480

As the figure indicates, the visualization of the IMFs of the healthy or for the defective bearing. The first empirical mode reveals the high-frequency impacts. This high-frequency mode increases in energy as the inner race fault progresses. The third mode shows the resonance in the vibration signal. The residue generated has not been used for further analysis due to the fact that it does not contain any rich information for a fault diagnosis. The resultant IMFs contain meaningful data, and it can be used for a variety of purposes.

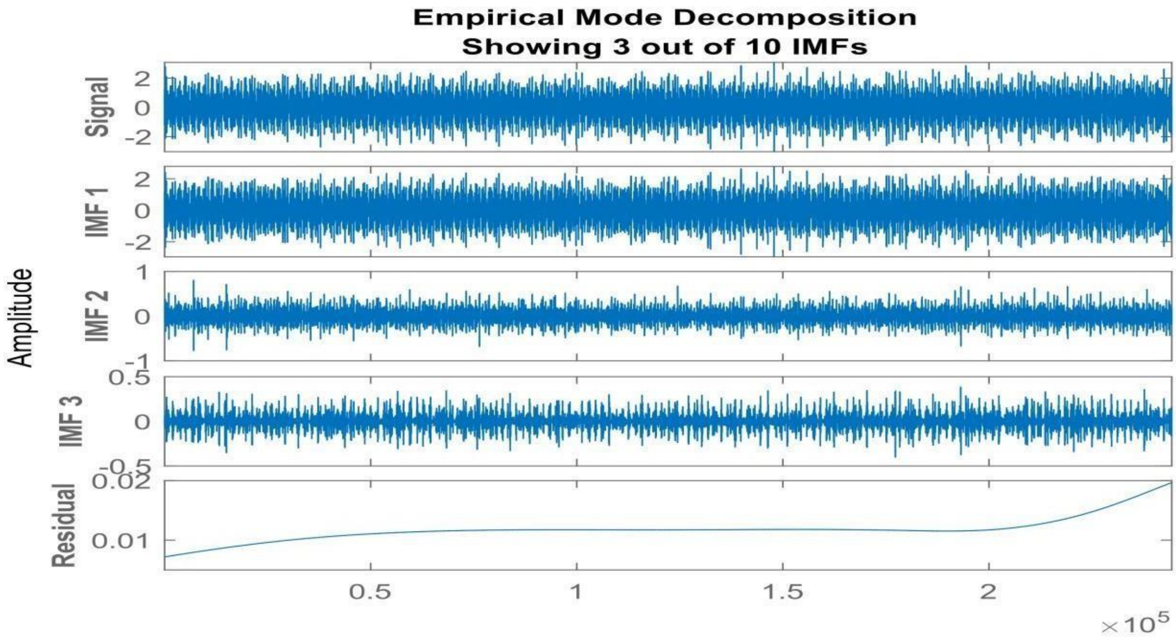

Figure 6. EMD of faulty inner race for 0.021in depth, 0HP, 1796RPM.

According to previous studies, EMD has a sudden change by a huge noise in the time-scaled decomposed signal called mixing mode. So, each IMF has a large number of frequency components (figure 5, figure 6).

To eliminate these phenomena, we perform Hilbert spectrum that could help for reaching the ultimate goal of data analysis for extracting the true signals.

✓Time-frequency domain: Hilbert Huang Transform

To create the Hilbert spectrum plot, we need the intrinsic mode functions (IMFs) of the signal obtained by the empirical decomposition method of the previous analysis.

ISSN: 1737-933481

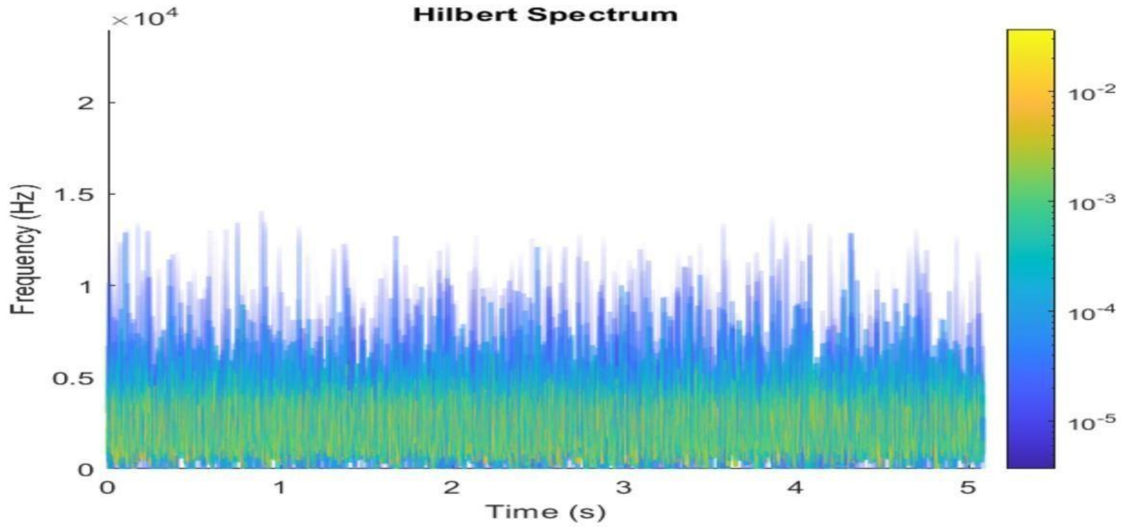

Figure 7. Hilbert spectrum of the healthy bearing (0HP, 1796RPM).

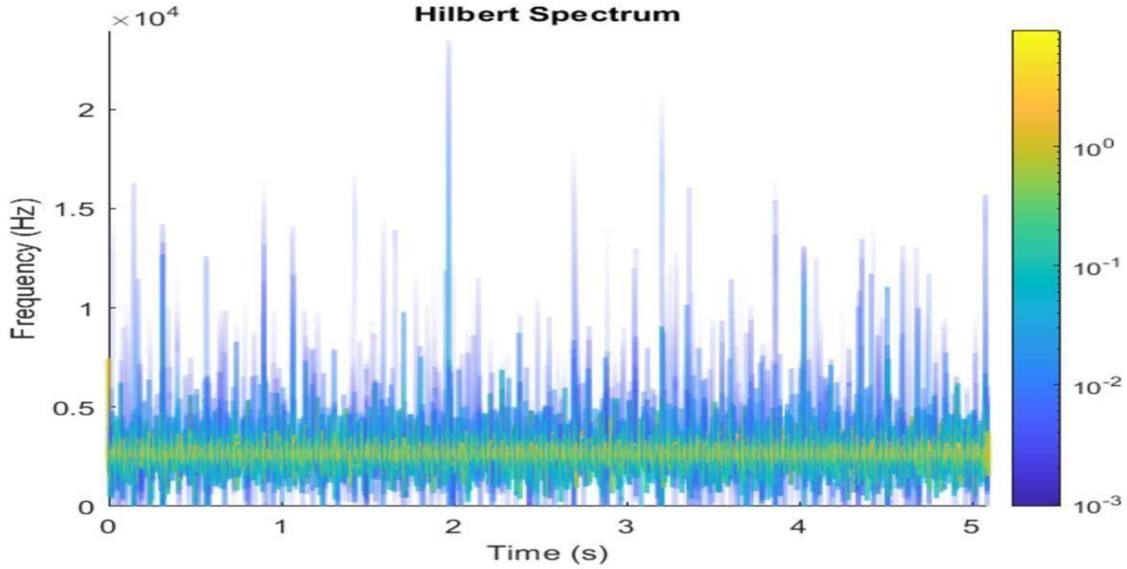

Figure 8. Hilbert spectrum of the inner race bearing fault (0HP, 1796RPM).

In Figure. 8, The frequency versus time plot is a sparse plot with a vertical color bar representing the instantaneous energy at each point in the IMF. The plot represents the instantaneous frequency spectrum of each component decomposed from the original mixed signal.

The Hilbert spectrum of IMFs 1, 3 (figure 7, figure 8) allow us to identify the frequency corresponding to the inner race fault. However, IMFs 2, 4,5,6,7,8,9,10 do not show significant anomalies (the amplitude of the defect is embedded in the noise).

The HT of the IMF 3, indicates high peaks around a harmonic of the frequency characteristic of inner race bearing fault. With an increase of the energy, which confirm that the signal is contain inner race bearing fault. We can conclude that, EMD and HT allows detecting and quantifying the fault for a given speed and load.

Conclusion:

Our research underlined the effectiveness of signal processing methods implemented in MATLAB for understanding real-time machine status. We start by extracting time-domain features from machine data using kurtosis. Then, extracting frequency-domain features using FFT, since the filter is designed based on the frequency information. EMD reflected as a self-adaptive and an automatic filter, by decomposing the signals into IMFs. These IMFs were classified locally from the highest frequencies to the lowest frequencies. Finally, extracting time-frequency domain features from the IMFs using Hilbert transform. The findings of this study indicate how powerful is signal processing-based techniques on detecting, locating, and quantifying the severity of degradation for a given speed and load. Our work clearly has some limitations related to the elimination of background noise that affects the quality of diagnosis. Like The need to choose the appropriate IMF, which will be used for further incorporation with other methods for extraction purposes or classification purposes using Artificial Intelligence. Time-frequency domains methods generally suffer from a need for strong expertise both for their application and for their interpretation. Despite this we believe our work could be a starting point for beginners on this field. We are currently in the process of investigating on how we implement more indicators in a machine learning for an automatic analysis.

ISSN: 1737-933483

References:

[1] A. Singh, K. R. Satyajit, and P. Ray, “A Computational Intelligence-Based Novel Bearing Defect Detection Method,” in *Recent Advances in Power Electronics and Drives*, S. Kumar, B. Singh, and A. K. Singh, Eds., in Lecture Notes in Electrical Engineering. Singapore: Springer Nature, 2022, pp. 645–659. doi: 10.1007/978-981-16-9239-0_49.

[2] M. A. Sher, X. Yu, and Q. Hu, “A Novel Fault Diagnosis of Bearing Approach using a Hybrid of Empirical Mode Decomposition and Discrete Wavelet Transform,” in *2021 IEEE Asia-Pacific Conference on Image Processing, Electronics and Computers (IPEC)*, Apr. 2021, pp. 865–870. doi: 10.1109/IPEC51340.2021.9421273.

[3] A. Soualhi, B. El Yousfi, H. Razik, and T. Wang, “A Novel Feature Extraction Method for the Condition Monitoring of Bearings,” *Energies*, vol. 14, no. 8, p. 2322, Apr. 2021, doi: 10.3390/en14082322.

[4] J. Weng, H. Sun, and B. Li, “Fault Identification of Rolling Bearing Based on Improved EMD-Kurtosis Criterion and DBN,” in *2022 4th International Conference on Artificial Intelligence and Advanced Manufacturing (AIAM)*, Oct. 2022, pp. 879–883. doi: 10.1109/AIAM57466.2022.00177.

[5] C. Zhou, Z. Xiong, H. Bai, L. Xing, Y. Jia, and X. Yuan, “Parameter-Adaptive TVF-EMD Feature Extraction Method Based on Improved GOA,” *Sensors*, vol. 22, no. 19, Art. no. 19, Jan. 2022, doi: 10.3390/s22197195.

[6] A. Faysal, N. W. Keng, and M. H. Lim, “Performance Evaluation of BPSO & PCA as Feature Reduction Techniques for Bearing Fault Diagnosis,” in *Recent Trends in Mechatronics Towards Industry 4.0*, A. F. Ab. Nasir, A. N. Ibrahim, I. Ishak, N. Mat Yahya, M. A. Zakaria, and A. P. P. Abdul Majeed, Eds., in Lecture Notes in Electrical Engineering. Singapore: Springer, 2022, pp. 605–615. doi: 10.1007/978-981-33-4597-3_55.

[7] R. Varghese P, M. S. P. Subathra, S. T. George, N. M. Kumar, E. S. Suviseshamuthu, and S. Deb, “Application of signal processing techniques and intelligent classifiers for high-impedance fault detection in ensuring the reliable operation of power distribution systems,” *Front. Energy Res.*, vol. 11, 2023, Accessed: May 14, 2023. [Online]. Available: https://www.frontiersin.org/articles/10.3389/fenrg.2023.1114230

[8] “https://csegroups.case.edu/ bearing datacenter/pages/download-,” *Bing*. https://www.bing.com/search?q=https%3A%2F%2Fcsegroups.case.edu%2F+bearing+datacenter%2Fpages%2Fdownload-&form=ANSPH1&refig=90d99c40b95f4e17b16669ec110ba786&pc=U531 (accessed Jul. 09, 2023).

ISSN: 1737-933484

Investigation of power flow calculation methods and analysis of computing efficiency

Fateh Ouali[#1], Narimen A. Lahaçani[*2],

[#]*Laboratoire de Maitrise des Energies Renouvelables, Faculté de Technologie, Université de Bejaia, 06000 Bejaia, Algeria*

[1]fateh.ouali@univ-bejaia.dz

[*] *Laboratoire de Maitrise des Energies Renouvelables, Faculté de Technologie, Université de Bejaia, 06000 Bejaia, Algeria*

[2]narimen.lahacani@univ-bejaia.dz

Abstract— **In this article, a comparison is made in the first place between the stability of the methods of calculating the power flow in terms of accuracy as well as the calculation time to show the characteristics of convergence or divergence of the three numerical methods most used in scientific research; therefore, they can be used in the case of the unavailability or temporary interruption of power measuring devices in some substations. Second, the analysis of the complexity of the execution time makes it possible to determine and compare the efficiency of algorithms to solve the same problem, as well as to study the impact of electric load modeling on power flow calculation algorithms, i.e., the evaluated power calculation methods such as the direct approach (DA), the front-back method (BFS), and the Newton-Raphson method (NR). Suitable methods are evaluated on a test and real IEEE HTA distribution network of 33, 69, and 155 buses. Satisfactory results are obtained by comparing the degree of uncertainty of the methods, the calculation time, and the number of iterations performed in the calculated power flow with other advantages.**

Keywords— **Power flow analysis; Newton Raphson; Backward/Forward Sweep, Approach direct, Execution time**

I. INTRODUCTION

The importance of power flow in the analysis and operation of the electrical system lies in its ability to determine steady-state voltage profiles and to provide information on the general operation of the system [1], [2]. It helps to assess the suitability of the nominal characteristics of the equipment, determine possible violations of voltage and current, and optimize the operation of the power system [3], [4]. In addition, the analysis of the power flow is considered fundamental data for the protective elements of the electrical system. It allows the coordination and proper functioning of relays and protective devices to ensure the safety and reliability of the electrical network. As a result, it ensures the safe and efficient operation of radial distribution systems and keeps them in good working order.

This type of analysis confronts the determination of the characteristics and performance of each method, which are evaluated on three radial distribution networks of different sizes, allowing weak areas for improvement to be identified. The analysis of power flow in RDN is based on solving a set of nonlinear algebraic equations with numerical methods such as the direct approach (DA)[5], Newton-Raphson (NR), and backward forward sweep (BFS) [6], [7]. Power flow equations are directly solved using matrix manipulation in DA, while an iterative technique based on power mismatches is employed by the NR method [8]–[10]. Power flow equations are solved iteratively from the load end to the source end in the BFS. The results of this analysis can be used to optimize the grid and manage distribution, including reconfiguration, fault detection, distributed generation placement (DG) and placement of flexible AC transmission Systems (FACTS) [11], [12]. The study of energy flow data has multiple objectives, such as optimizing energy production, identifying technical problems in electrical systems, planning preventive maintenance, monitoring the quality of the electrical wave, reducing costs associated with energy production and transmission, and improving the safety and reliability of electricity distribution. In addition, network design is a sizable combinatorial optimization problem with a difficult-to-find optimal solution [13], [14]. This makes computational time, rapid convergence of these methods, and load modeling important in load flow analysis, as they affect the accuracy, efficiency, and reliability of results [15], [16]. Despite extensive research on computation optimization, convergence analysis, and load modeling for power flow methods, there are still gaps that need attention. Further exploration is needed to develop advanced parallel processing techniques and machine learning to improve power flow calculations in large-scale systems [5], [17].

ISSN: 1737-85

Studying convergence challenges in complex scenarios, such as renewable energy integration and voltage stability issues, is essential to ensuring accurate load flow solutions. Improving the accuracy of load modeling by taking dynamic and stochastic load behaviors into account and integrating uncertainty analysis to manage prediction errors and measurement uncertainties will further improve the reliability and accuracy of power calculation results.

II. METHODOLOGY

Power flow analysis is typically performed in an experimental configuration involving a simulated radial network, such as IEEE systems or the real 155-bus Bejaia radial network. In this configuration, the mathematical expression of the power flow problem can be formulated as a system of nonlinear equations that model the relationships between voltages, currents, and active and reactive powers in an electrical system [18]. The amplitude of the voltages at the buses of the network and the currents in the branches are generally the variables to be determined.

The equations describing the system can be derived from Kirchhoff's equations for loads and power equilibria, as well as Ohm's and Faraday's laws governing the relations between currents and voltages. Solving the problem can be done using the power flow methods listed in Section I. The convergence is measured by monitoring certain criteria, such as the maximum mismatch of tension between successive iterations for a tolerance defined at one Pico, which are considered estimation performance measures of these methods. In addition, the number of iterations required and the execution time, the accuracy of the power flow analysis is evaluated by comparing the calculated maximum error values of voltage amplitudes, phase shifts. Performance measures, such as mean square error (RMS) and maximum deviation from predicted values, are used to quantify the accuracy of these algorithms.

A range of charge modeling approaches are examined in this work by integrating mathematical models that represent the distinct characteristics and behaviors of different types of electric charges. In order to evaluate the influence of these load modeling techniques on the analysis and optimization of power systems, load models are integrated with load flow analysis algorithms to assess the impact on the functionality and stability of these algorithms.

A. Selected Methods

In this section, we describe the methods that will be used as references in our study: These methods of calculating power flow were chosen for their reliability and accuracy, as well as for their relevance and importance in the field of electrical engineering and for their ability to achieve computational objectives.

1. Direct approach

The power flow calculation method called the direct approach is used to solve PF equations directly to determine voltages and currents. The solution is achieved through an iterative approach, using input data such as active and reactive power consumption at each network node and line data.

S_i The expression for the complex load at the node level is provided:

$$S_i = P_i + jQ_i \tag{1}$$

At iteration k of the solution, the corresponding equivalent current injection is calculated.

$$I_i^k =)I_i^{\$} + I_i^{i*} = +\left(\frac{S_i}{V_i^k}\right)^* \tag{2}$$

The bus voltage V and the equivalent current injection I of the bus at iteration k are represented, where the real and imaginary parts of the current injection equivalent to the k-th iteration are indicated as I^r and I^i, respectively.

The relationship between the branch current and the nodal currents of the bus is expressed by the following equation.

$$[B] = [BIBC][I] \tag{3}$$

The variable vectors [B], $[I]$ and matrix variables [BIBC] are concerned, where represents the branch current, represents the bus current, and refers to a matrix known as the branch current node injection matrix defined in [17]. The constant matrix is an upper triangular matrix composed of only 0 and +1 values. It applies to different power system analysis techniques, including load rate analysis, failure analysis, and stability analysis. This technique is used to examine the performance of power systems under various operating conditions.

ISSN: 1737-86

2. Backward/Forward Sweep

The Backward/Forward Sweep (BFS) method is an iterative method that involves performing a backward swipe and a forward swipe through the power grid. It is an iterative approach that can solve equations at different nodes in the network. The principle of this method is during the backward scanning, the knot currents are calculated using the voltages of the nodes and the injected apparent power using the equations 2 and 3.

The first step in initialization is to select one of the nodes as the voltage reference node. Then, the system voltage of each node is initialized to 1 pu. The tolerance value for the voltage loop is set at 10^{-12}.

The calculation is performed using the backward/forward scan method. During the backward phase, the node currents are determined from the nodes furthest from the reference node using the Kirchhoff current equations for each node. These node currents are then summed to determine the branch currents associated with each row in the system. During the forward phase, the knot voltages are determined from the reference node using the Kirchhoff voltage equations for each node. These knot voltages are used to determine the voltages at the ends of the branches.

$$S_i^* = V_i^* \sum_{k=1}^{n} Y_{ik} V_k \tag{4}$$

where * denotes the complex conjugate.

3. Newton–Raphson Methods

The Newton-Raphson (NR) method is a commonly used method for calculating power flow. The objective of this method is to iteratively solve nonlinear equations in order to determine the voltages at each node of the network. Active and reactive power equations for each branch of the network are used, as are input data such as loads, generators, and line configuration. The NR method relies on deriving equations to find a solution that gradually approaches reality with each iteration, until a convergent solution is reached. Details of the NR method are provided in references [7], [19].

The formulation of the power flow problem by the Newton-Raphson method makes it possible to use the expressions of active and reactive power in the following ways:

$$S_i = P_i + jQ_i = V_i \sum_{k=1}^{n} Y_{ik}^* V_k^* \tag{5}$$

$$S_i = \sum_{k=1}^{n} (V_i V_k Y_{ik}) \angle(\delta_i - \delta_k - \theta_{ik}) \tag{6}$$

$$P_i = V_i V_k Y_{ik} \cos\theta_{ii} + \sum_{\substack{k=1 \\ k \neq i}}^{n} (V_i V_k Y_{ik}) \cos(\delta_i - \delta_k - \theta_{ik}) \tag{7}$$

$$Q_i = V_i V_k Y_{ik} \cos\theta_{ii} + \sum_{\substack{k=1 \\ k \neq i}}^{n} (V_i V_k Y_{ik}) \sin(\delta_i - \delta_k - \theta_{ik}) \tag{8}$$

In each iteration, a Jacobian matrix is constructed and then solved. This matrix equation offers a linearized correlation between alterations in voltage angle (δ) and voltage magnitude (V), represented as follows:

$$\begin{bmatrix} \Delta P \\ \Delta Q \end{bmatrix} = J \begin{bmatrix} \Delta\delta \\ \Delta|V| \end{bmatrix} \tag{9}$$

Elements of the Jacobian matrix are the partial derivatives which are given as:

$$J = \begin{bmatrix} \frac{\partial P}{\partial \delta} & \frac{\partial P}{\partial |V_i|} \\ \frac{\partial Q}{\partial \delta} & \frac{\partial Q}{\partial |V_i|} \end{bmatrix} \tag{10}$$

The system of equations is solved to determine the next iteration of the voltage amplitude and angles, as shown in the following equations:

$$\delta_i^{(k+1)} = \delta_i^{(k)} + \Delta\delta_i^{(k)} \tag{11}$$

$$|V_i^{(k+1)}| = |V_i^{(k)}| + \Delta |V_i^{(k)}| \tag{12}$$

The calculations are repeated as many times as necessary until the specified tolerance is reached.

Where; ΔP and ΔQ are the difference between the planned and calculated values. k and (k+1) indicate the previous and next iterations, respectively.

$\delta_i^{(k+1)}$ and $\Delta\delta_i^{(k)}$ are the calculated angle and the variation of the calculated angle, respectively;

$|V_i^{(k+1)}|$ and $|V_i^{(k)}|$ are the voltage magnitude at iteration k at node i.

The total real and reactive power losses for each method are calculated as follows:

$$\begin{cases} P_{total_{loss}} = \sum_{i}^{nb} \frac{Pl_i^2 + Ql_i^2}{|V_i|^2} R_i \\ Q_{total_{loss}} = \sum_{i}^{nb} \frac{Pl_i^2 + Ql_i^2}{|V_i|^2} X_i \end{cases} \tag{13}$$

R_i and X_i are the resistance and reactance of the line i-th.

B. Modeling the voltage dependency of system loads

Load modeling describes how electrical power is used by consumers in an electrical system. This anticipates the demand for electrical energy through an analysis as a function of weather conditions and consumption habits at different times of the day or year, which is important for producers and suppliers of electrical energy to plan and size their production and distribution capacity.

The dependence on load constraints is modeled by a mathematical function for more accurate analysis and planning and to see its influence on power flow calculation algorithms. These loads are modeled using the variable load model, where the power absorbed by the load varies according to the amplitude of the voltage [20], [21]. A composite model of loads is considered.

The modeling of voltage-dependent loads Pl_i and Ql_i is adapted from [10]. The active and reactive power loads of node 'i' are given as follows:

$$\begin{cases} Pl_i = P_{n_i} \left[a_0 + a_1 V_i + a_2 V_i^2 \right] \\ Ql_i = Q_{n_i} \left[b_0 + b_1 V_i + b_2 V_i^2 \right] \end{cases} \tag{14}$$

Where P_n and Q_n are the nominal active and reactive loads, respectively. The other load coefficients (a_0, a_1, a_2) and (b_0, b_1, b_2) must satisfy the following equations:

$$\begin{cases} a_0 + a_1 + a_2 = 1 \\ b_0 + b_1 + b_2 = 1 \end{cases} \tag{15}$$

Exponential load modeling is essential to understanding the behavior of electrical systems. It refers to a load profile that shows rapid growth or decrease in energy consumption over time. The modeling equations for exponential load use parameters k1 and k2, which determine the magnitude of the change in energy consumption relative to a reference voltage V_{ref} using "(16)". Typical values of k1 range from 0.6 to 1.8, while values of k2 range from 1.6 to 6. These models help simulate and analyze the effects of exponential charging on electrical systems [20], [22].

$$\begin{cases} Pl_{,i} = P_{n_i}\left(\frac{V_i}{V_{re9}}\right)^{k1} \\ Ql_{,i} = Q_{n_i}\left(\frac{V_i}{V_{re9}}\right)^{k_2} \end{cases} \quad (16)$$

The heating and charging systems of electric vehicles (EVs) often have exponential electrical load profiles due to the nature of their active energy requirements. In this case, we will review the minimum k1 and the maximum k2.

III. RIGOROUS VALIDATION OF POWER FLOW ANALYSIS

The proposed methods were validated by a series of rigorous simulations and comparisons. These attempts were aimed at evaluating the performance, accuracy, and reliability of algorithms in various scenarios. The validation process involved the use of reference datasets and numerical simulation studies performed on the MATLAB_R2023a software version using a 3.3 GHz Intel Core i7 processor with 16 GB of RAM. And these three systems, namely IEEE 33-bus, 69-bus, and 155-bus of the Bejaia region, as shown in the appendix, are considered cases of small and medium-scale networks. Each of these systems is used as a relatively small- and medium-scale network case for the purposes of this comparative study. The effectiveness of each proposed method is verified using the complete data from these systems, which start from a specific initial point of 1 pu.

To ensure consistency, fairness, and that all methods are implemented and executed under similar conditions in this comparison. The size and nature of the radial network, as well as the hardware and software used, have been selected to provide a fair basis for evaluating the performance of these methods.

A. Statistical analysis of results

By comparing these proposed methods based on iterative processes on several critical factors in order to eliminate bias and provide a fair comparison, a consistent set of input data, system parameters, and computing resources is used for all three methods. This comparison provided valuable information on the efficiency of the calculation. The evaluation of the execution time of these algorithms is performed using tools provided by MATLAB, such as tic toc and timeit, both of which are used as parameters to assess the calculation time of these algorithms. MAE (Average Absolute Error) is employed by the first function, and RMSE (Root Mean Square Error) is employed by the second function, respectively.

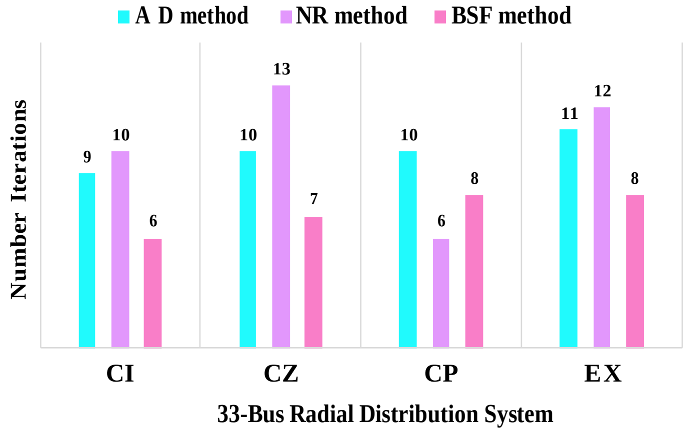

Fig. 1 Comparison of the performance in terms of the number of iterations of load flow methods

ISSN: 1737-89

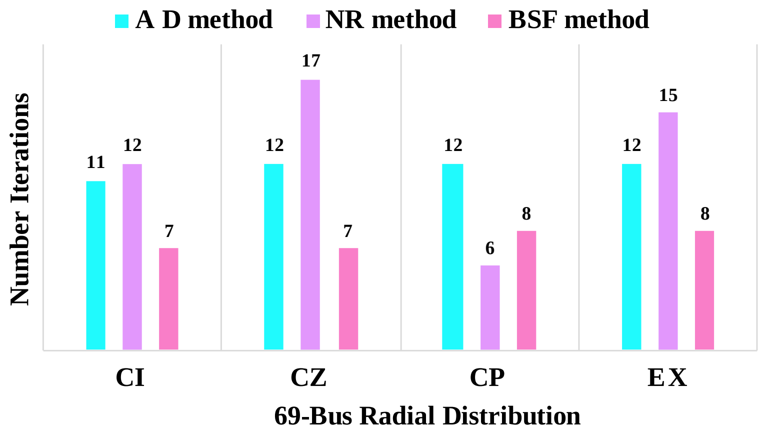

Fig. 2 Comparison of the performance in terms of the number of iterations of load flow methods

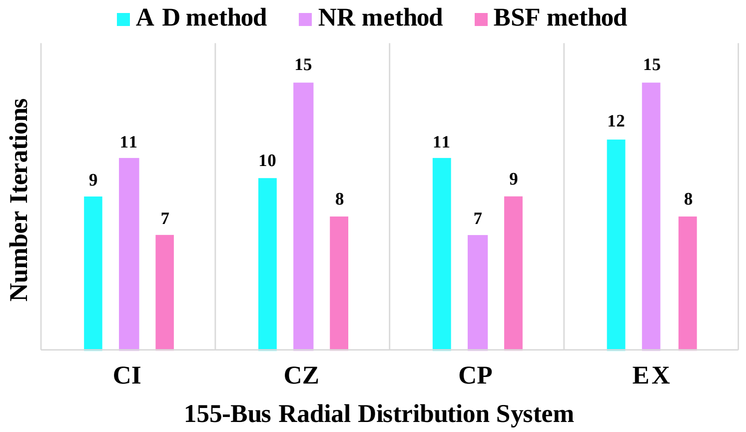

Fig. 3 Comparison of the performance in terms of the number of iterations of load flow methods

Figures 1, 2, and 3 illustrate the comparison of the number of iterations of the different methods of calculating the power flow. The direct approach (DA) and the BFS (Backward/Forward Sweep) method differ in their stability in terms of number of iterations, regardless of network size and load types. On the other hand, the Newton-Raphson (NR) method shows a significant variation in the number of iterations according to the types of loads. This suggests that the NR method may be more sensitive to variations in electrical loads and require more frequent iteration adjustments to achieve convergence.

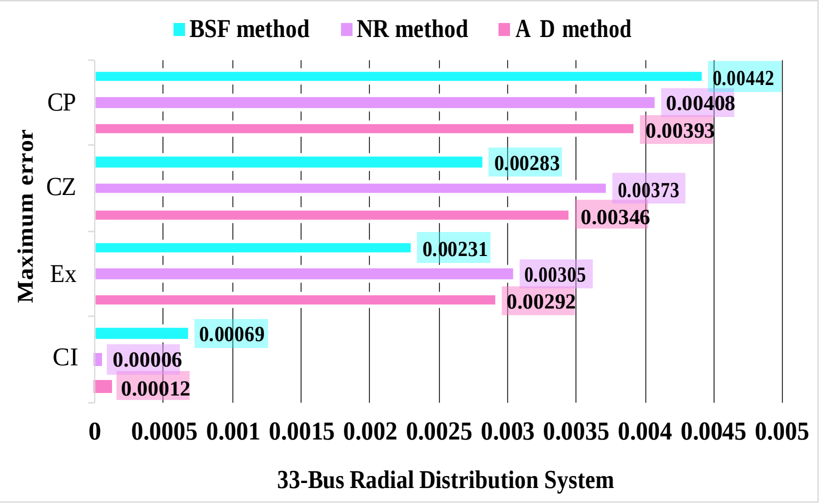

Fig. 4 Maximum error between two successive iterations

ISSN: 1737-90

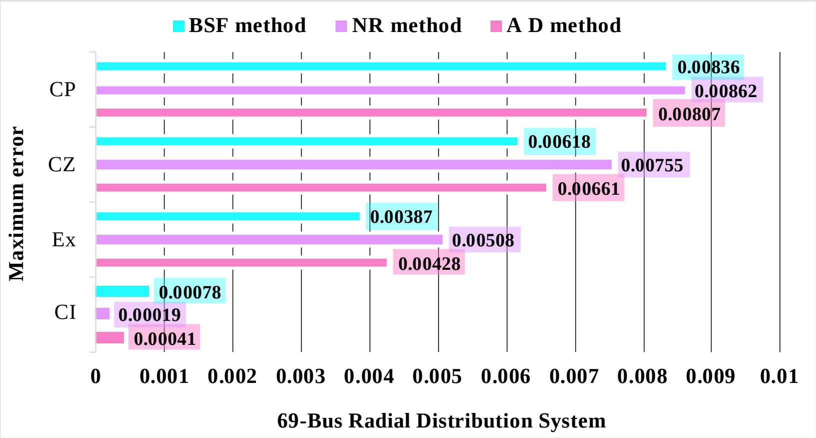

Fig. 5 Maximum error between two successive iterations

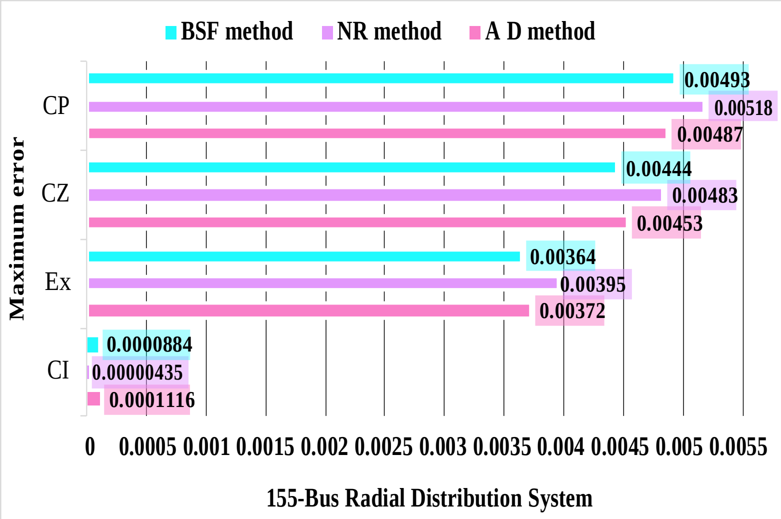

Fig. 6 Maximum error between two successive iterations

Figures 4, 5, and 6 show the stability of the maximum error between two successive iterations for each method. These figures show the results for the three radial networks, as a function of load type. We see a similar pattern across all figures. The DA and BFS approaches continue to show maximum error stability between successive iterations, regardless of network size or load type. These methods maintain weak and almost stable errors, demonstrating their ability to converge effectively in radial networks.

The figures 7, 8, and 9 highlights the differences in run time between the three approaches for the different radial network systems and the four load modeling scenarios. The DA and BFS approaches show quasi-stable run times, while the NR approach shows increased run time with larger networks and different load modeling. These findings allow us to assess the computer efficiency of each approach and suggest that the DA and BFS approaches are the most appropriate for the radial network, regardless of the type of load selected.

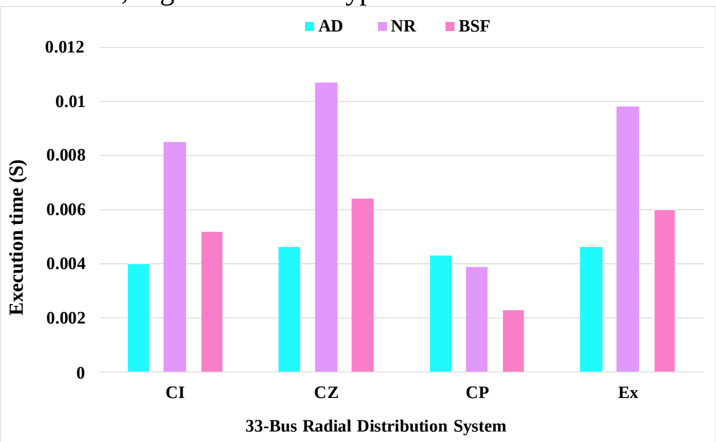

Fig. 7 Comparison of the performance in terms of the execution time

ISSN: 1737-91

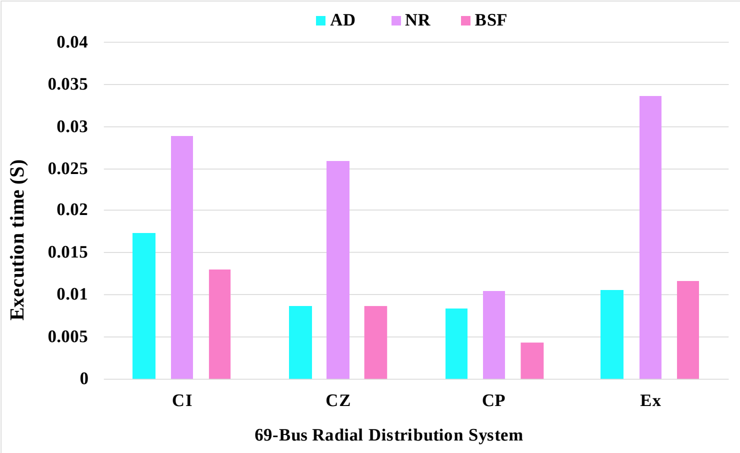

Fig. 8 Comparison of the performance in terms of the execution time

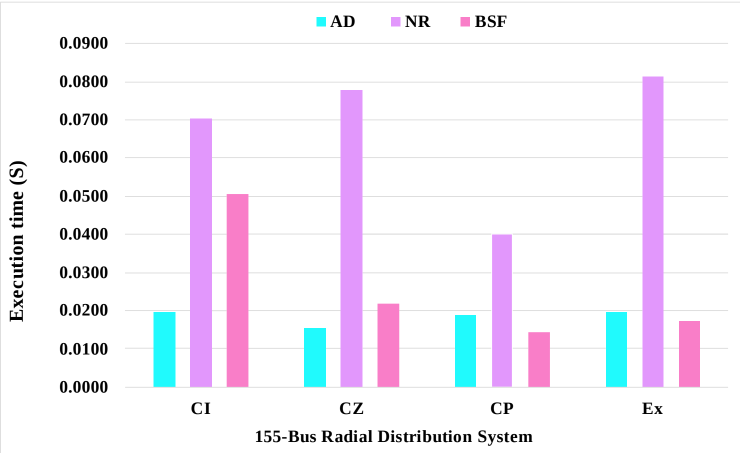

Fig. 9 Comparison of the performance in terms of the execution time

B. Comparative analysis

This section presents the results of our analysis on the computational efficiency, execution time taken by each algorithm, number of iterations, power losses, convergence characteristics, and performance of these power flow calculation methods, which sheds light on their ability to analyze and know the state of the power system.

Throughout the validation process, extensive analyses were conducted to ensure that the proposed methods met the required criteria. Statistical analyses, error assessments, and sensitivity studies were conducted to thoroughly assess the efficiency of these methods. The results provide valuable information on the strengths and limitations of each method, helping to select the most appropriate load flow method for specific applications. The test results demonstrate the flexibility and accuracy of the proposed algorithms for the intended applications.

Overall, the validation process provided comprehensive evidence of the ability of the proposed methods to provide reliable and accurate results in the analysis of power systems. It demonstrated their strengths, highlighted their limitations, and identified areas for improvement. The results of the validation provided coherence in the practical implementation of these methods and supported their integration into power system analysis and operational workflows.

C. Discussion

Based on the analysis performed, significant differences were observed in the results of the comparative tests, including run time, number of iterations, and total power losses. The behavior of these algorithms and their iterative approach to the solution have been observed; in this instance, the reference relates to the voltage rather than the power because using the Newton-Raphson method caused the algorithm to become unstable and diverge. These differences are crucial for ensuring the protection of the power system and effective long-range planning, where accuracy holds importance.

ISSN: 1737-92

IV. Conclusions

In conclusion, these methods demonstrated their ability to maintain consistently low and stable errors, showcasing reliable and robust convergence across various radial network sizes. However, further analysis is recommended to ascertain the simulation's reliability and validate the baseline assumptions.

Furthermore, the algorithms' behavior, especially their iterative approach to the solution, was closely monitored during the study. Notably, using the Newton-Raphson method with power as the reference parameter led to instability and divergence.

Additionally, it is crucial to consider the influence of Electronic Control Unit (ECU) technology and the relative robustness of the algorithms in the analysis. These factors can significantly impact the execution time and the concordance required to achieve convergence and find solutions to the systems under study. Careful consideration of these aspects can enhance the accuracy and efficiency of power flow calculations in practical applications.

Acknowledgment

We would like to thank the DGRSDT of Algeria for providing necessary subventions to our laboratory.

References

[1] A. Kumar, B. K. Jha, D. K. Dheer, D. Singh, and R. K. Misra, ‘Nested backward/forward sweep algorithm for power flow analysis of droop regulated islanded microgrids’, *IET Gener. Transm. Distrib.*, vol. 13, no. 14, pp. 3086–3095, Jul. 2019, doi: 10.1049/iet-gtd.2019.0388.

[2] M. Gao, J. Yu, Z. Yang, and J. Zhao, ‘A Physics-Guided Graph Convolution Neural Network for Optimal Power Flow’, *IEEE Trans. Power Syst.*, vol. PP, pp. 1–11, 2023, doi: 10.1109/TPWRS.2023.3238377.

[3] A. Pandey, M. Jereminov, M. R. Wagner, D. M. Bromberg, G. Hug, and L. Pileggi, ‘Robust Power Flow and Three-Phase Power Flow Analyses’, *IEEE Trans. Power Syst.*, vol. 34, no. 1, pp. 616–626, Jan. 2019, doi: 10.1109/TPWRS.2018.2863042.

[4] S. Venkatasivanagaraju and M. V. Rao, ‘Loss Minimization and Optimal Power flow for long term and short-term Real-Time Forecasting System using Cuckoo Search Algorithm’, in *2022 Second International Conference on Artificial Intelligence and Smart Energy (ICAIS)*, Feb. 2022, pp. 805–810, doi: 10.1109/ICAIS53314.2022.9742990.

[5] U. H. Ramadhani, M. Shepero, J. Munkhammar, J. Widén, and N. Etherden, ‘Review of probabilistic load flow approaches for power distribution systems with photovoltaic generation and electric vehicle charging’, *Int. J. Electr. Power Energy Syst.*, vol. 120, no. December 2019, p. 106003, Sep. 2020, doi: 10.1016/j.ijepes.2020.106003.

[6] M. Balasubbareddy, D. Dwivedi, G. V. K. Murthy, and K. S. Kumar, ‘Optimal power flow solution with current injection model of generalized interline power flow controller using ameliorated ant lion optimization’, *Int. J. Electr. Comput. Eng.*, vol. 13, no. 1, p. 1060, Feb. 2023, doi: 10.11591/ijece.v13i1.pp1060-1077.

[7] J. Dancker and M. Wolter, ‘Improved quasi-steady-state power flow calculation for district heating systems: A coupled Newton-Raphson approach’, *Appl. Energy*, vol. 295, p. 116930, Aug. 2021, doi: 10.1016/j.apenergy.2021.116930.

[8] Y. Venkatesan, K. Srilakshmi, and A. Palanivelu, ‘Modified soccer game optimization and its application on power flow and distribution generation placement problems of distribution systems’, *Evol. Intell.*, vol. 16, no. 2, pp. 539–552, Apr. 2023, doi: 10.1007/s12065-021-00677-9.

[9] Z. Shao, Q. Zhai, Y. Mao, and X. Guan, ‘A method for evaluating and improving linear power flow models in system with large fluctuations’, *Int. J. Electr. Power Energy Syst.*, vol. 145, no. August 2022, p. 108635, Feb. 2023, doi: 10.1016/j.ijepes.2022.108635.

[10] S. Bhalla, S. Kumar, and S. K. Aggarwal, ‘Comparative Analysis of Newton’s Higher Order Methods for Load Flow Problem’, in *2019 Amity International Conference on Artificial Intelligence (AICAI)*, Feb. 2019, no. 1, pp. 334–339, doi: 10.1109/AICAI.2019.8701346.

[11] P. P. Biswas, P. Arora, R. Mallipeddi, P. N. Suganthan, and B. K. Panigrahi, ‘Optimal placement and sizing of FACTS devices for optimal power flow in a wind power integrated electrical network’, *Neural Comput. Appl.*, vol. 33, no. 12, pp. 6753–6774, Jun. 2021, doi: 10.1007/s00521-020-05453-x.

[12] J. Zhang, J. Cai, S. Wang, and P. Li, ‘Many-objective optimal power flow problems based on distributed power flow calculations for hierarchical partition-managed power systems’, *Int. J. Electr. Power Energy Syst.*, vol. 148, no. January, p. 108945, Jun. 2023, doi: 10.1016/j.ijepes.2023.108945.

[13] M. Zheng, R. Zhou, S. Liu, F. Liu, and X. Guo, ‘Route Design Model of Multiple Feeder Bus Service Based on Existing Bus Lines’, *J. Adv. Transp.*, vol. 2020, pp. 1–12, Dec. 2020, doi: 10.1155/2020/8853872.

[14] Z. Wu, D. Fan, and F. Zou, ‘Traction Load Modeling and Parameter Identification Based on Improved Sparrow Search Algorithm’, *Energies*, vol. 15, no. 14, p. 5034, Jul. 2022, doi: 10.3390/en15145034.

[15] M. S. Shahriar, ‘Load-flow dependent twofold technique of tolerance selection for robust estimation of power system states’, *Adv. Eng. Softw.*, vol. 176, no. August 2022, p. 103376, Feb. 2023, doi: 10.1016/j.advengsoft.2022.103376.

[16] F. D. Freitas and L. Neves de Oliveira, ‘Conditioning step on the initial estimate when solving ill-conditioned power flow problems’, *Int. J. Electr. Power Energy Syst.*, vol. 146, no. October 2022, p. 108772, Mar. 2023, doi: 10.1016/j.ijepes.2022.108772.

ISSN: 1737-93

[17] H. Bennani, A. Chebak, and A. El Ouafi, 'A generic power flow formulation for flexible modeling and fast solving for large-scale unbalanced networks', *Int. J. Electr. Power Energy Syst.*, vol. 148, no. January, p. 108956, Jun. 2023, doi: 10.1016/j.ijepes.2023.108956.

[18] L. H. T. Bandória, M. C. Almeida, and T. R. Fernandes, 'A phasor rotation-based approach to represent PV buses on the current injection power flow', *Electr. Power Syst. Res.*, vol. 216, no. October 2022, p. 108999, Mar. 2023, doi: 10.1016/j.epsr.2022.108999.

[19] R. G. Wasley, B. S. Tech, M. Sc, D. Ph, M. A. Shlash, and M. Sc, 'Newton-Raphson algorithm for 3-phase load flow', vol. 121, no. 7, 1974.

[20] J. Yang *et al.*, 'Identification and Stabilization of Constant Power Loads in AC Microgrids', *IEEE Trans. Ind. Electron.*, vol. PP, pp. 1–10, 2023, doi: 10.1109/TIE.2023.3257386.

[21] S. Nikkhah, A. Rabiee, A. Soroudi, A. Allahham, P. C. Taylor, and D. Giaouris, 'Distributed flexibility to maintain security margin through decentralised TSO–DSO coordination', *Int. J. Electr. Power Energy Syst.*, vol. 146, no. June 2022, p. 108735, Mar. 2023, doi: 10.1016/j.ijepes.2022.108735.

[22] J. S. Bhadoriya, A. R. Gupta, and B. Khan, 'Analysis of Pre- and during COVID-19 Mixed Load Models on Unbalanced Radial Distribution System Using a New Metaphor-Less Rao Optimization', *Int. Trans. Electr. Energy Syst.*, vol. 2023, pp. 1–21, Mar. 2023, doi: 10.1155/2023/6777135.

APPENDIX

Bejaia Radial Distribution Network 155 buses.

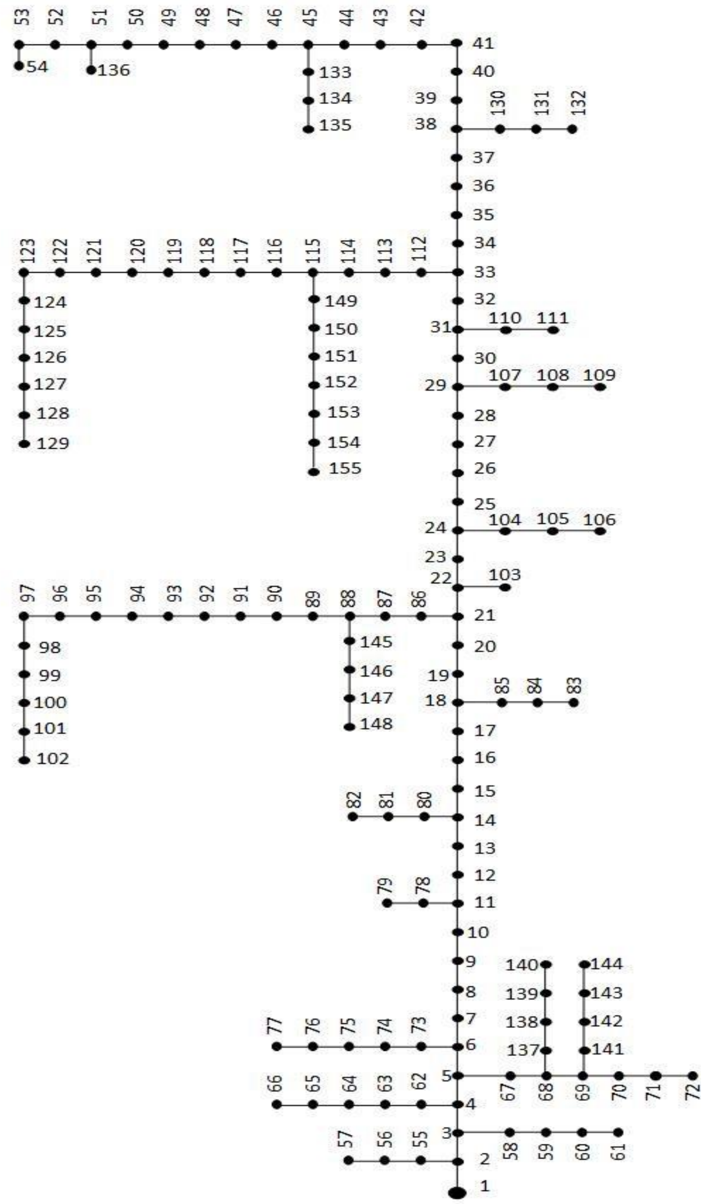

ISSN: 1737-95